



Université
de Toulouse

THÈSE

En vue de l'obtention du

DOCTORAT DE L'UNIVERSITÉ DE TOULOUSE

Délivré par :

Institut National Polytechnique de Toulouse (INP Toulouse)

Discipline ou spécialité :

Dynamique des fluides

Présentée et soutenue par :

M. BLAISE DELMOTTE

le lundi 21 septembre 2015

Titre :

MODELING AND SIMULATION OF INDIVIDUAL AND COLLECTIVE
SWIMMING MECHANISMS IN ACTIVE SUSPENSIONS

Ecole doctorale :

Mécanique, Energétique, Génie civil, Procédés (MEGeP)

Unité de recherche :

Institut de Mécanique des Fluides de Toulouse (I.M.F.T.)

Directeur(s) de Thèse :

M. ERIC CLIMENT

M. PIERRE DEGOND

Rapporteurs :

M. IGNACIO PAGONABARRAGA, UNIVERSITE DE BARCELONE

M. RAYMOND GOLDSTEIN, UNIVERSITE DE CAMBRIDGE

Membre(s) du jury :

M. BERTRAND MAURY, UNIVERSITE PARIS 11, Président

M. ERIC CLIMENT, INP TOULOUSE, Membre

M. ERIC KEAVENY, IMPERIAL COLLEGE OF SCIENCE LONDRES, Membre

M. FRANCK PLOURABOUE, INP TOULOUSE, Membre

Mme AREZOO ARDEKANI, PURDUE UNIVERSITY EU, Membre

M. PIERRE DEGOND, IMPERIAL COLLEGE OF SCIENCE LONDRES, Membre

À Lolotte et Odette.

Acknowledgments

Merci. Thanks. Gracias.

Les travaux exposés dans le présent manuscrit ont été effectués à l’Institut de Mécanique des Fluides de Toulouse (IMFT), au sein du groupe Particules Sprays et Combustion, et ont été financés par une bourse MESR-Midi-Pyrénées. Trois séjours de un mois chacun ont été menés à l’Imperial College (Londres).

Un grand merci à mes directeurs et encadrants de thèse: Eric Climent, Franck Plouraboué, Eric Keaveny et Pierre Degond. Ils ont toujours été, sans exception, disponibles et à l’écoute tout en me laissant une grande marge de manoeuvre. Eric (C), bien que je garde un souvenir amer et douloureux de ma défaite (11 – 12) contre toi au tournoi de pétanque 2012/2013, je te remercie d’avoir fait en sorte que nos interactions soient toujours agréables (sauf à la pétanque) et constructives. Merci pour avoir toujours soutenu mes initiatives, avoir su me guider quand il le fallait et pour savoir garder ce calme olympien en toute circonstances, qui a le bel effet d’être parfois communicatif. Un très grand merci à Franck, tu es l’origine de cette aventure. Sans ton projet INSA sur les traceurs passifs dans un vaisseau, il y a maintenant 5 ans, tout ça n’aurait pas eu lieu. Merci pour ta gentillesse, ta grande disponibilité et tes encouragements. Ta rigueur mathématique et ton optimisme m’ont été d’une précieuse aide. A huge thank to Eric (K), that I consider as one of my Ph.D supervisors. I really had a great time working with you and my stays at IC were great. You taught me a lot and an important part of the theoretical knowledge I acquired during my Ph.D comes from you. Thank you for these interesting projects that we carried out together. Our collaboration was very stimulating and I am glad to have done this work with you. Thank you for all the good times we spent in London but also in Toulouse! Merci à Pierre également pour ses conseils et sa disponibilité. Tu as toujours accepté mes sollicitations et tu as ajouté un point de vue intéressant sur mes travaux. J’ai beaucoup apprécié d’intégrer avec toi sur les modèles continus à Londres, c’était une expérience passionnante.

I would like to thank Raymond Goldstein for accepting to review this manuscript. También quiero agradecer Ignacio Pagonabarraga por aceptar leer esta tesis. Je remercie également Bertrand Maury d’avoir accepté d’être le président de ce jury. I would also like to thank Arezoo Ardekani for accepting to be part of this committee. I am honored to have such a prestigious committee for my Ph.D defense, I am grateful to all the committee members.

Je remercie l'IMFT pour l'accueil et les moyens mis à disposition, et en particulier le groupe PSC pour sa convivialité. Tout au long de ces trois ans, l'ambiance était excellente! Une dédicace à quelques personnes dont Jeannot (oh que oui!), Mimile (et ses AK47), Guillaume La Poutre, Manu (la flamenca-bolosse), Crep' mon compagnon de route, Baldus le fou, Numéro 1 toujours relax, Pradip (le paparazzi), Maxou (qui aime les marcel). Un salut aussi à Daniel, Anna (belle vie à Paris), Lolo (porté sur la chose), Sebastien, Guillaume, Quentin, Ibrahima (Bravo pour le stage!), Solène (vive le bureau 315!), Nico, Duc, François, Aurelien, Salvo (au fond on s'aime bien quand même!), Vielou (si tu m'entends), Mostafa (a pleasure working with you) et beaucoup d'autres. Ce fut aussi un plaisir des fréquenter les autres équipes dont Simon (pour nos cafés philosophiques), Nico le dauphin (ou Causette), Jean-Lou (alias "où est Charlie?"), Audrey (faudra que tu viennes te baigner dans l'Agly!) et Mathieu (vive la funk!). Un grand merci à l'équipe fondatrice de Doct'Eau pour les bons moments: Élise, Thomas, Édouard, Maxime, Damien et Mauricio.

I also would like to thank my office mates at IC. Alex (check my rythms!), Cesco (un plaisir!), Bogdan, Toby and Alastair. I spent great times with you guys. We will have to schedule our next box race!

I must mention Navish Wadhwa. We had great time working together but also hanging out in the streets of San Francisco or on a huge boat heading to Finland. I hope we will have other opportunities to collaborate!

I thank Aleksandar Donev for insightful discussions on fluctuating hydrodynamics. I am glad to have him as a future post-doc supervisor.

Un très grand merci à Pascal Fede pour sa précieuse aide. Sans toi, le code FCM ne serait pas aussi efficace et les fibres s'ennuieraient dans les écoulements de Stokes, je te dois beaucoup (oui je sais je te dois déjà des bières)! Merci beaucoup à Annaïg Pedrono. Patiente, sympathique et compétente, tu m'as beaucoup aidé!

J'en profite également pour mentionner que nombre de simulations ont été effectuées au centre de calcul régional CALMIP ainsi qu'à l'IDRIS. Merci pour leur support. Je remercie aussi les institutions qui ont financé la collaboration avec l'Imperial College: l'INPT, le COST Action MP1305 "Flowing Matter" et l'École des Docteurs de Toulouse.

Des personnes extérieures m'ont aussi soutenu lors de cette aventure. Notamment je tiens à remercier mes amis! Je rends particulièrement hommage à ma famille à laquelle je suis très attaché. Je salut aussi ma famille de La Réunion (Nou la fé!). Enfin, la présence de Marine à mes côtés a été un soutien incomparable. Merci pour ta gentillesse, ta compréhension et pour ton sourire.

Abstract

We have all witnessed the flocking of starlings in the sky and the schools of fish that form in the ocean. This kind of organization of living creatures is not limited to those that we see, but also occurs for those that we don't: swimming microorganisms. Suspensions of micro-swimmers exhibit a rich dynamics. Their behaviors can play an important role in the survival of the group, its development, the balance between species, their trophic strategies and even animal fertility. They can form coherent structures due to collective motion, mix the surrounding fluid or modify its rheological properties. Such diversity results from the complex interplay between swimming strategies, physiological processes, chemical reactions and hydrodynamic interactions. Fluid Mechanics is therefore essential to understand and master the mechanisms involved in these phenomena. While experimental studies bring out new findings and, sometimes, provide physical explanations, modeling remains essential. Yet, including an accurate description of the micro-swimmers in a suspension containing thousands (nay millions) individuals, requires considering a wide range of coupled scales (from one micron $10^{-6}m$ to several millimeters $10^{-3}m$). What happens on large scales depends on sophisticated mechanisms occurring two or three orders of magnitude below. Therefore, the multiscale modeling of such phenomena is still a major challenge for the state-of-the-art numerical methods.

This thesis aims at providing a contribution in that direction.

In a first part, we will show that reproducing swimming mechanisms at the scale of the micro-swimmer can be achieved with various models spanning different levels of complexity. We will then present our developments to incorporate these models in an efficient framework for large scale simulations. We will show how to simultaneously account for the Brownian motion of the smallest particles ($10^{-6}m$). Our code reproduces known results from the literature with the same accuracy, but at lower cost and at larger scales, thus bridging a gap between particle-based models, experiments and continuum formulations from kinetic theory. Using the capabilities afforded by our method, we eventually address two open problems in the experimental literature: the origins of orientational correlations between interacting self-propelled micro-droplets and the mechanisms at play in the nonlinear enhancement of Brownian particle diffusion in active suspensions.

Keywords: *Micro-organisms, Active Suspensions, Numerical Modeling, Low Reynolds number flows, Brownian motion.*

Résumé

Nous avons tou(te)s été témoins des nuages d'étourneaux dans le ciel ou de la formation de bancs de poissons dans l'océan. Ce type d'organisation chez les êtres vivant se produit aussi à des échelles parfois invisibles pour l'œil humain: celles des micro-organismes. Les suspensions de micro-nageurs présentent une dynamique riche. Elles peuvent former des structures cohérentes résultant d'un mouvement collectif, mélanger le fluides environnant et/ou modifier ses propriétés rhéologiques. Leurs comportements peuvent jouer un rôle important dans la survie, l'équilibre des espèces, leur stratégie trophique et même dans la fertilité animale. La diversité des phénomènes observés résulte de l'interaction complexe entre mécanismes de nage, processus physiologiques, processus chimiques et interactions hydrodynamiques. Comprendre et maîtriser les mécanismes impliqués fait nécessairement appel la Mécanique des Fluides. Les études expérimentales permettent de mettre en exergue certains phénomènes et parfois de les expliquer. Cependant la modélisation s'avère indispensable. Or, inclure une description fine des mécanismes de nages dans une suspension contenant des milliers (voire des millions) d'individus, implique de considérer une vaste gamme d'échelles couplées (typiquement du micron $10^{-6}m$ au millimètre $10^{-3}m$). Décrire une physique multi-échelles pour ce type problème reste un défi majeur pour la modélisation numérique actuelle.

Ainsi, dans le cadre de cette thèse nous nous proposons d'apporter une contribution dans cette direction. Nous montrerons dans une première partie qu'il est possible de reproduire les mécanismes de nage de façon satisfaisante à l'échelle du microorganisme avec des modèles de différentes complexités. Nous présenterons ensuite nos développements pour étendre ces modèles à l'échelle de la suspension. Nous montrerons comment inclure simultanément les effets Browniens qui agissent sur les plus petite particules ($10^{-6}m$). Enfin, nous exploiterons l'outil mis en place pour simuler des suspensions actives. Sa capacité à reproduire certains résultats de la littérature à précision égale, à moindre coût et à plus grande échelle, permet de combler le fossé entre modèles individuels, travaux expérimentaux et modèles continus issus de la théorie cinétique. Forts de cet outil, nous tenterons de répondre à deux questions ouvertes dans la littérature expérimentale : l'origine des corrélations d'orientation dans les suspensions de micro-gouttes auto-propulsées et les mécanismes en jeu dans la diffusion des particules Browniennes dans les suspensions actives.

Mots clés: *Microorganismes, Suspensions Actives, Modélisation numérique, Écoulements à bas nombre de Reynolds, Fluctuations Browniennes*

Contents

Introduction and theoretical background.	1
I Swimming Mechanisms at Small Scales	9
1 Introduction: understanding locomotion at microscales and its consequences	11
1.1 Short overview of swimming mechanisms	11
1.2 Why swimming mechanisms are interesting to study?	14
1.3 How to model these mechanisms ?	16
2 A general formulation of bead models applied to flexible fibers and active filaments at low Reynolds number.	19
2.1 Introduction	20
2.2 The bead model	22
2.3 Validations	37
2.4 Conclusions	54
2.5 Addendum: correspondence between \mathcal{M} and \mathcal{M}^*	54
3 Biologically-relevant mesoscopic models.	57
3.1 Squirmers using the force-coupling method	58
3.2 A time-dependent squirmer model based on experimental data	64
4 Conclusions: towards large multiscale simulations of active suspensions.	73
II From Small to Large Scales: A Modeling Challenge	77
5 Introduction: models for the multiscale physics of active suspensions.	79
5.1 How to model active suspension ?	79
5.2 Brownian motion in particulate suspensions.	81
6 Modeling active suspensions with the force-coupling method.	83
6.1 Solving hydrodynamic interactions with the force-coupling method	84
6.2 Numerical tools for High Performance Computing	86
6.3 Validations	90

7	Time integration for particle Brownian motion determined through fluctuating hydrodynamics	95
7.1	Introduction	96
7.2	Equations of motion	98
7.3	Fluctuating FCM	99
7.4	Time integration	103
7.5	Numerical studies	108
7.6	Conclusions	123
8	Conclusions: combining fluctuating FCM with active FCM.	125
III	The Physics of Active Suspensions	127
9	Introduction: the rich dynamics of active suspensions.	129
9.1	Where do we find active suspensions ?	129
9.2	Why do we study active suspensions ?	130
9.3	The role of numerical and theoretical models	134
10	Orientalional correlations in active suspensions: a parametric study at large scales.	137
10.1	Simulation Results on Polar Ordering in Suspensions of Squirmer	138
10.2	Extensions to ellipsoidal swimmers and time-dependent swimming gaits . .	151
10.3	Conclusions	157
11	Enhanced diffusion in dilute and concentrated active suspensions.	159
11.1	Introduction: theory for enhanced transport in dilute suspensions	160
11.2	Enhanced tracer diffusion in dilute suspensions of micro-swimmers	163
11.3	Nonlinear evolution of diffusion at higher volume fractions: a preliminary study for an open problem	174
11.4	Conclusions	178
12	Conclusions: a closer step towards experiments and continuum models.	179
12.1	Conclusions and future directions	179
12.2	A continuum model for squirmer suspensions ?	180
	Conclusions and Future Directions.	183
	References	188
	Appendices	211
A	Self-induced effects for spheroidal swimmers	213

A.1	Self-induced velocity \mathbf{W} due to the degenerate quadrupole \mathbf{H}	213
A.2	Self-induced rate of strain \mathbf{K} due to the squirmer dipole \mathbf{G}	215
A.3	Test case 1: torque against strain	216
A.4	Test case 2: ROS and velocity of a tilted passive/active spheroid in a shear flow	217
B	Handling collisions with kinematic constraints	219
B.1	Formulation and algorithm	219
B.2	Numerical tests	222
B.3	Conclusions	226
C	Stress-free boundary conditions with fluctuating hydrodynamics	227
D	Error expansion for the Drifter-Corrector	231
E	Coupling active FCM with fluctuating FCM	235
E.1	Langevin equation for the rotational motion of uniaxial objects	235
E.2	Langevin equation for the rotational motion of spherical swimmers	236
E.3	Integration scheme for swimmer orientation	237
E.4	Conclusions	240
F	Unit quaternions vs. orientation vectors: a note on angular integration	241
F.1	Description and formalism	241
F.2	Application to rotation	242
F.3	Tracking orientation: a comparative study	243
F.4	How to chose ?	250
G	Continuum models for squirmers: preliminary investigations with the monokinetic and the Von-Mises-Fischer closures.	251
G.1	Basic equations	252
G.2	System entropy	253
G.3	Monokinetic closure	254
G.4	Von-Mises-Fisher (VMF) closure	261
G.5	Conclusions	274

List of Tables

3.1	Magnitudes of the Fourier modes used to describe $B_2(t)$ in $\text{rad} \cdot \text{s}^{-1}$	65
3.2	Phases of the Fourier modes used to describe $B_2(t)$ in rad	65
6.1	Parameters for the contact forces on Figure 6.7b	91
7.1	Parameter values for the icosahedron collapse simulations.	118
7.2	Simulation parameters for the colloidal gelation simulations	120
7.3	State of the suspension at $t/t_{D_a} = 300$ for different values of ϕ_v . The numbers in parentheses correspond to the number of particles in the domain N_p . The label ‘‘P’’ indicates that the particles aggregated to form a percolated network, while ‘‘NP’’ indicates that they have not. The snapshots show the suspensions at the final time and N_c is the number of clusters in the images (accounting for periodicity).	121
A.1	Comparison of numerical results (num) with Eq. (A.15), (th), for the rotation rate ω_y of a passive/active spheroid aligned with $\hat{\mathbf{x}}$ and subject to a torque given by Eq. (A.14) in a shear flow $\mathbf{u}^\infty = \dot{\gamma}z\hat{\mathbf{x}}$, with $\dot{\gamma} = 1$	217
A.2	ROS and velocity of a tilted passive/active spheroid in a shear flow $\mathbf{u}^\infty = \dot{\gamma}z\hat{\mathbf{x}}$ with $\dot{\gamma} = 5$. β is the squirming parameter, $\theta = \cos^{-1}(\mathbf{p} \cdot \hat{\mathbf{x}})$ and $U = 1$	218
B.1	Simulation parameters.	222

List of Figures

1	Pathway of the thesis: we first focus on the details of swimming mechanisms, then change scale with mesoscopic models that we incorporate in large scale simulations to address the physics of active suspensions at the lab scale.	2
1.1	(a) Ciliary beating pattern decomposed into a power stroke and a recovery stroke. (b) <i>Chlamydomonas reinhardtii</i> uses ciliary beating to perform breaststroke swimming with its anterior appendages. Figure extracted from Leptos et al. (2013).	12
1.2	Examples of micro-swimmers using ciliary propulsion on their surface.	13
1.3	Propagation of bending waves along the flagellum of human sperm in a highly viscous liquid. Figure extracted from Smith et al. (2009)	13
1.4	Examples of artificial micro-swimmers.	15
2.1	The spring model uses a linear spring with stiffness k_s to keep constant the inter-particle distance.	24
2.2	joint model: if there is no gap between adjacent beads, particles overlap when beding occurs. c_1 is the contact point between bead 1 and 2.	24
2.3	joint model: the contact point c_1 is separated by a gap ε_g from the bead surfaces to prevent overlapping in case of bending.	25
2.4	gears model: the velocity at the contact point c_1 must be the same for each bead (Eq. (2.18)).	29
2.5	Beam discretization and bending torques computation of beads 1, 3 and 5. Remaining torques are accordingly obtained: $\tau_b^2 = \mathbf{m}(s_3)$ and $\tau_b^4 = -\mathbf{m}(s_3)$. 31	31
2.6	Dependence of the constraints $\bar{\varepsilon}_M/\dot{\gamma}L$ on the time step $\dot{\gamma}\Delta t$, + : gears model, \square : joint model. Inset: $\bar{\varepsilon}_M/\dot{\gamma}L$ with the gears model for a fixed time step given by Eq. (2.37) for different values of $\dot{\gamma}$	36
2.7	Tumbling period T depending on fiber aspect ratio r_p . \ominus : theoretical law Eq. (2.49) with r_e given by Eq. (2.51), \boxminus : theoretical law Eq. (2.49) with r_e given by Eq. (2.50), \triangle : gears model, ∇ : joint model.	38
2.8	Orbit of a flexible filament in a shear flow with BR = 0.04. Temporal evolution is shown in the plane of shear flow. (a) Symmetric ‘‘S-shape’’ of a straight filament, $\kappa^{eq} = 0$. (b) Buckling of a permanently deformed rod with an intrinsic curvature $\kappa^{eq} = 1/(100L)$	40

2.9 (a) Minimal radius of curvature depending on fiber length for several bending ratios. \boxminus : BR = 0.01, \ominus : BR = 0.03, ∇ : BR = 0.04, \triangleleft : BR = 0.07. (b) Minimal radius of curvature along BR. \circ : current simulations with aspect ratio $r_p = 35$ and intrinsic curvature $\kappa^{eq} = 0$; \bullet : current simulations with aspect ratio $r_p = 35$ and intrinsic curvature $\kappa^{eq} = 1/(10L)$; simulation results from Schmid et al. (2000) with $\kappa^{eq} = 1/(10L)$: (\diamond : $r_p = 50$, \triangle : $r_p = 100$, ∇ : $r_p = 150$, \square : $r_p = 280$); $+$: experimental measurements from Salinas and Pittman (1981), $r_p = 283$ 41

2.10 Shape of settling fiber for $B = 10000$ in the frame moving with the center of mass (x_c, z_c) . (a) Metastable “W” shape, $t = 12L/V_s$. (b) Steady “horseshoe” shape at $t = 53L/V_s$. V_s is the terminal settling velocity once steady state is reached. 43

2.11 (a) Scaled vertical deflection A/L depending on the elasto-gravitational number B . \bullet : gears model, \diamond : joint model, \boxminus : FCM results from Keaveny (2008), \triangleleft : Stokeslets results from Cosentino Lagomarsino et al. (2005), ∇ : Slender body theory results from Li et al. (2013). (b) Normal friction coefficient *vs.* B . \bullet : gears model, \diamond : joint model, \boxminus : FCM results from Keaveny (2008), \triangleleft : Stokeslets results from Cosentino Lagomarsino et al. (2005). 44

2.12 Comparison with experiments and numerical results from Yu et al. (2006). gears model results are superimposed on the original Fig. 3 of Yu et al. (2006). Snapshots are shown for four equally spaced intervals during the cycle for one tail with $\alpha_0 = 0.435\text{rad}$. \bullet : experiment, --- : linear theory, ---- : non-linear theory, — : gears model, a) $\zeta = 0.5 \text{ rad}\cdot\text{s}^{-1}$, Sp= 1.73. b) $\zeta = 1.31 \text{ rad}\cdot\text{s}^{-1}$, Sp= 2.2. c) $\zeta = 5.24 \text{ rad}\cdot\text{s}^{-1}$, Sp= 3.11. 48

2.13 Comparison with experiments from Coq et al. (2008). (Insets) Evolution of the filament shape with Sp⁴. Snapshots are shown for twenty equally spaced intervals during one period at steady state. Gray level fades as time progresses. Left inset: δ_0/L is the distance of the tethered bead to the rotation axis, d/L is the distance of the free end to the rotation axis. (Main figure) Distance of the rod free end to the rotation axis normalized by the filament length d/L . \diamond : experiment, \bullet : gears model with no anchoring distance $\delta_0/L = 0$, \blacksquare : gears model with $\delta_0/L = 0.1 \rightarrow 0.02$ as in Coq et al. (2009). 49

2.14 (a) Simulated wave motion of a swimming model *C. Elegans*. The nematode swims leftward and gray level fades as time progresses. Motion is shown in a frame moving with the micro-swimmer center of mass. (b) Inset: two *C. Elegans* beating in the same plane at a distance d in opposite phase ($\Delta\phi = \pi$). Nematodes swim leftward and gray level fades as time progresses. Main figure: Swimming speed of the center of mass of the system V normalized by the isolated swimming speed of *C. Elegans* V^* . \circ : in-phase motion ($\Delta\phi = 0$); \square : antiphase motion ($\Delta\phi = \pi$). 51

2.15	Helical swimming of <i>C. Elegans</i> . (Inset) Snapshot for $Sp^* = 22.6^{1/4}$ and $A_2/A_1 = 1$. $\bullet \rightarrow$ trajectory of the center of mass. (Main figure) Swimming speed of the center of mass V normalized by the planar swimming speed of <i>C. Elegans</i> V^* . —: $A_2/A_1 = 1$, -·-·-: $A_2/A_1 = 0.5$, - - - -: $A_2/A_1 = 0$ (planar motion),	53
3.1	Decomposition of squirmer velocity field for $\beta = 1$	60
3.2	Velocity field \mathbf{u}/U around a puller squirmer ($\beta = 1$) swimming to the right. (a) Blake’s solution; (b) FCM solution with σ_Θ for the degenerate quadrupole envelope. (c) FCM solution with $\sigma_\Theta/2$ for the degenerate quadrupole envelope.	63
3.3	Comparison with Blake’s solution, Eq. (3.14). (a) Normalized difference, $\ \mathbf{u}^{\text{Blake}} - \mathbf{u}^{\text{FCM}}\ /U$, between FCM and Blake’s solution for a puller squirmer ($\beta = 1$). The half-width for the degenerate quadrupole envelope is σ_Θ . —: 10% iso-value. (b) Velocity profile along the swimmer axis for Blake’s solution and the FCM approximation for the two different degenerate quadrupole envelope sizes.	63
3.4	a) $(B_1(t), B_2(t))$ phase diagram for one beat cycle. b) Power dissipation $\Pi_d(t)$ over one beat cycle. —: FCM, \circ : results from Guasto et al. (2010).	66
3.5	Snapshots of the time-dependent flow field around a model <i>Chlamydomonas</i> . Background grey levels represent the natural logarithm of the norm of the velocity field in $\text{rad} \cdot \text{s}^{-1}$. \blacksquare : position of the stagnation point given by the FCM model. \blacklozenge : position of the stagnation point measured by Guasto et al. (2010). (Insets) Swimming speed along the beat cycle.	67
3.6	Snapshots of the time-dependent (A-F) flow field around a copepod <i>Arcatia tonsa</i> at its naupliar stage. This figure is taken from Wadhwa et al. (2014).	69
3.7	Flow field around <i>Arcatia tonsa</i> at different times along the breaststroke. Vector scale is 1/100. The contours represent the norm of the velocity field $\ \mathbf{u}\ /(L/2)$ Left: experimental data. Right: model.	71
4.1	Current extensions of the Gears Model (in progress).	74
4.2	“Exotic” swimming gaits in the phase space $(B_1(t), B_2(t))$	75
6.1	Scaling of the FCM with the number of squirmers N_p . Computational time per time-step versus N_p , or equivalently, versus volumetric fraction ϕ_v . $N_c = 256$ cores work in parallel for a cubic domain with 384^3 grid points.	87
6.2	Snapshot of a concentrated suspension ($\phi_v = 0.2$) containing $N_p = 75,000$ squirmers. Micro-swimmers are colored with the norm of their velocity \mathbf{V}^n , $n = 1, N_p$, normalized by the intrinsic swimming speed U	88
6.3	Sketch showing the set-up of our computations of the interactions between squirmer “1” and inert sphere “2”.	91
6.4	The (a) Radial velocity $ U_{r,2} $, (b) Angular velocity $ \Omega_{z,2} $, (c) Stresslet component $ S_{xx,2} $, and (d) Stresslet component $ S_{xy,2} $ for the inert sphere “2” at a distance r from a puller squirmer ($\beta = 5$).	92

6.5	Initial configuration of the squirmers in the trajectory simulations.	93
6.6	Trajectories of two squirmers swimming in opposite directions with transverse initial distance $\delta y = 1a, \dots, 10a$. Lines: data from Ishikawa et al. (2006). Symbols: FCM results.	93
6.7	Influence of the collision barrier parameters on the squirmer trajectories for the case where initially $\delta y = 1a$. (a) Trajectories. Crosses: data from Ishikawa et al. (2006). (b) Force barrier profiles. The line styles correspond those showing the trajectories in a). ----: barrier used in Figure 6.6.	94
7.1	A comparison between the wall-normal mobility coefficient and the auto-correlation of the wall-normal particle velocity. —: $2k_B T \mu_{\perp}^{FCM}$, \circ : $\Delta t \left\langle \left(\tilde{V}_{\perp}^{FCM} \right)^2 \right\rangle$, —: $2k_B T \mu_{\perp}^{FCM-S}$, $+$: $\Delta t \left\langle \left(\tilde{V}_{\perp}^{FCM-S} \right)^2 \right\rangle$	112
7.2	Sketch showing a particle (and its image) in the slip channel. The black dashed line represents the periodic boundaries conditions. The index γ runs over the z -coordinate of the grid. The potential $U(z)$ provides the interaction between the particle with the slip surfaces and is given by Eq. (7.73). The force on the particle is $F_U(z) = -\partial U / \partial z$	113
7.3	The equilibrium distribution for a Brownian particle subject to the potential $U(z)$. The distribution from simulations is obtained by averaging 10 simulations of 500 non-interacting particles over the time interval $t/t_{D_a} = 6.526 - 391.60$. \ominus : DC, \diamond : Central RFD with $\delta = 10^{-6} \Delta x$, \bullet : Gibbs-Boltzmann distribution Eq. (7.74), \square : Euler-Maruyama Scheme, \blacksquare : Biased Gibbs-Boltzmann ditribution Eq. (7.75). (a) Without stresslets, (b) With stresslet corrections.	115
7.4	The evolution of the particle distribution during the time interval $t/t_{D_a} = 0 - 6.8037$. The results from the particle simulations are achieved by averaging over 20 simulations, each with 500 non-interacting particles. The stresslet corrections are included in these simulations. ----: fluctuating FCM with the DC, —: solution to the Smoluchowski equation (7.77) - (7.78).	116
7.5	The radius of gyration $R_g(t)$ (in units of Δx) during the time interval $t/t_{D_a} = 0 - 150$. The results are obtained by averaging over 150 independent simulations. ----: no hydrodynamic interactions; - - - -: FCM without stresslets, Euler-Maruyama scheme; \cdots : FCM-S, central RFD; —: FCM-S, DC.	118
7.6	Time evolution of the aggregation process for $\phi_v = 0.04 - 0.12$ and $\kappa = 4/a$. 120	
7.7	Snapshots of the aggregation process for $\phi_v = 0.08$ and $N_p = 3766$	122
9.1	Bioconvection and gyrotaxis (left) can play a role in the formation of large blooms (Durham and Stocker (2012)) (right).	131
9.2	Meso-scale turbulence in living fluids. Left: bacteria. Right: ram sperm.	132
9.3	Sudden clogging due to the exponential growth of biofilm streamers (green fluo) in a microfluidic channel. Figure extracted from Drescher et al. (2013). 133	

9.4 Experimental observations of stirring in active suspensions. 134

9.5 Active droplets are potential swimmers (a) that exhibit polar ordering (b). 135

9.6 (a) Flow field around *Volvox*. The lower panel compares the experimental flow field with a fit based on a point stresslet, a point source doublet (degenerate quadrupole) and a monopole due to buoyancy forces. Figure extracted from Drescher et al. (2010). (b) Cluster of *Volvox* moving collectively. Figure extracted from Drescher et al. (2009). 136

10.1 Polar order $P(t)$ in a semi-dilute suspension ($\phi_v = 0.1$) of squirmer pullers ($\beta = 1$). a) Time evolution of polar order depending on the number of swimmers. \ominus : $L/a = 14, N_p = 64$; \boxminus : $L/a = 19, N_p = 174$; \triangleleft : $L/a = 38, N_p = 1,395$; ∇ : $L/a = 58, N_p = 4,707$; \ast : $L/a = 77, N_p = 11,158$; \dashv : $L/a = 116, N_p = 37,659$. b) steady-state value P^∞ depending on $N_p \sim (L/a)^3$. $---$: fit linear with $1/\sqrt{N_p}$. (Inset): Dependence of P^∞ with $1/\sqrt{N_p}$ 140

10.2 Snapshots of the orientational state in a semi-dilute suspension ($\phi_v = 0.1$) containing $N_p = 37,659$ swimmers with $\beta = 1$. $\langle \mathbf{p} \rangle$ is the mean steady-state orientation vector on the unit sphere defined in Eq. (10.2). $\mathbf{p}^n \cdot \langle \mathbf{p} \rangle$ thus represents the degree of alignment along the mean direction $\langle \mathbf{p} \rangle$ of swimmer n , $n = 1, \dots, N_p$ 141

10.3 Characterization of the polar instability. (Main figure): Time evolution of polar order in semilogarithmic scale suggests an exponential growth of the instability. (Inset): Growth rate of the instability for different values of N_p (or L/a). 141

10.4 Orientational distribution on the unit sphere $\Psi(\phi, \theta)$. (a) Distribution before the transition to polar order: $t = 90a/U$. (b) Distribution once the polar ordered state is reached: $t = 1110a/U$ 142

10.5 Time-averaged steady-state orientational distribution in the frame of the mean unit orientation vector $\Psi(\theta, \phi)|_{\langle \mathbf{p} \rangle}$. (a) Distribution over the unit sphere. (b) \ominus : distribution of elevation angle θ averaged over azimuthal angle ϕ ; $---$: uniform distribution $\Psi_0(\theta) = 1/\pi$; \boxminus : distribution of azimuthal angle ϕ averaged over elevation angle θ ; $----$: uniform distribution $\Psi_0(\phi) = 1/(2\pi)$ 143

10.6 Distribution of Voronoi cell volumes. (Main figure): Time dependence of the standard deviation, σ_V , of the Voronoi volume distribution normalized by the mean value $\langle V_V \rangle$. (Inset): PDF of normalized cell sizes $V_V/\langle V_V \rangle$, time-averaged before ($---$) and after ($---$) the polar order transition. 143

10.7 Section of the computational domain showing the clustering effect. The regions delimited by red lines are particle clusters. Lines represent the fluid velocity vectors in the plane: \mathbf{u}_{2D} . They are colored with their norm normalized by the intrinsic swimming speed U . Spheres correspond to the swimmers and their size is proportional to the distance to the plane. Arrows represent the swimmers' orientation. 144

10.8 steady-state pair distribution function (a) $g(r, \theta)$. (b) $g(r)$ 145

10.9 Correlations in squirmer orientation at steady-state. (a) $I_{\mathbf{p}}(r, \theta)$. (b) $I_{\mathbf{p}}(r)$ 146

10.10 Growth of the polar order parameter $P(t)$ for $\phi_v = 0.005 - 0.15$ and $\beta = 1$. (Main figure): Time evolution of polar order in semilogarithmic scale suggests an exponential growth of the instability. —: exponential fits to obtain the growth rate τ^{-1} . (Inset): Growth rate of the instability τ^{-1} for various swimmer volume fractions ϕ_v . —: linear fit. 147

10.11 Comparison between the characteristic growth rate τ^{-1} of the polar order instability and the collisional time τ_c for various values of the volume fraction ϕ_v . - - - -: mean value 131.331 148

10.12 Polar order $P(t)$ in a semi-dilute suspension ($\phi_v = 0.1$) of squirmer with $\beta = 0$. (a) Time evolution of polar order depending on the number of swimmers. \ominus : $L/a = 14, N_p = 64$; \boxplus : $L/a = 19, N_p = 174$; \triangleleft : $L/a = 38, N_p = 1,395$; ∇ : $L/a = 58, N_p = 4,707$; \star : $L/a = 77, N_p = 11,158$. (b) Same as a) but with a semilog scale. —: exponential fits to obtain the growth rate τ^{-1} . (Inset): Growth rate of the instability for different N_p (and L/a). 149

10.13 Polar order $P(t)$ in a semi-dilute suspension ($\phi_v = 0.1$) of squirmer with $\beta = 0$. Each one of the 125 curves represents the evolution of $P(t)$ computed in one of the 125 subdomains. 150

10.14 Simulation of a dilute suspensions, $\phi_v = 0.05$, of prolate spheroidal pushers, $B_2 = -1.5, B_1 = 0$, with aspect ratio $\frac{a_1}{a_2} = \frac{a_1}{a_3} = 3$. (a) Snapshot at $t = 30U/a_1$. Colors indicate the velocity magnitude normalized by the individual swimming speed. (b) Time evolution of polar order $P(t)$. - - - -: isotropic value of the polar order parameter $1/\sqrt{N_p} = 0.026$ 153

10.15 Relative trajectories of two *C. Rheinardtii* swimming in opposite directions with stroke phase shift $\Delta\varphi$ and initial transverse distance $\delta y = 1a$ and $2a$. The grey levels lighten as $\Delta\varphi$ increases from $\Delta\varphi = 0 \rightarrow \Delta\varphi = 7\pi/4$. - - - - -: trajectory of two steady squirmers with $\beta = 0$. - - - - : trajectory of two steady squirmers with $\beta = 0.1$. (Top) $\delta y = 1a$. (Bottom) $\delta y = 2a$ 154

10.16 Polar order parameter and orientational distribution for suspensions of steady and time-dependent swimmers. —: time-dependent swimmers with random phase ($\Delta\varphi_n \in [0; 2\pi]$); \cdots : synchronized time-dependent swimmers ($\Delta\varphi_n = 0, \forall n$); - - - -: steady swimmers with $\beta = 0$; - - - -: steady swimmers with $\beta = 0.1$. (a) Time evolution of polar order. (b) steady-state orientation distribution around the mean director $\Psi(\theta)|_{\langle \mathbf{p} \rangle}$. —: uniform distribution $\Psi_0(\theta) = 1/\pi$; 156

11.1 Snapshot of the simulation domain containing $N_p = 301$ swimmers and 1255 tracers, with $a_{sw}/a = 5$. The volume fraction is $\phi_v = 10\%$. The large grey spheres are the squirmers and the small black dots correspond to the tracers. Vectors represent the swimmers' orientations $\mathbf{p}^n, n = 1, \dots, N_p$. Slices represent the norm of the fluid velocity field normalized by the intrinsic swimming speed $\|\mathbf{u}\|/U$. One can observe the fluid velocity fluctuations due to Brownian agitation. 165

11.2	Discrepancy between the experimental data and the Gaussian fit of Leptos et al. (2009).	166
11.3	Tracer displacements in dilute suspensions of squirmers with $\beta = 0.5$. Displacements are averaged over the three spatial directions.	167
11.4	Log-log plot representation of Figure 11.3a. Symbols represent the data from Leptos et al. (2009). Solid lines correspond to the simulations. ----: x^{-4} . - - - - : x^{-3} . Displacements are averaged over the three spatial directions.	167
11.5	Tracer displacements for the squirmer model at long times. Displacements are averaged over the three spatial directions.	169
11.6	Mean squared displacement of tracers at various cell concentrations for the squirmer model with $\beta = 0.5$. Displacements are averaged over the three spatial directions.	170
11.7	Effective diffusion coefficient of tracers for the squirmer model with $\beta = 0.5$. \ominus : simulations. \square : data from Leptos et al. (2009).	171
11.8	Statistics on tracer displacements for the squirmer model with $\beta = 0$	172
11.9	Tracer displacements at $\Delta t = 0.12s$ for the time-dependent and steady models with $\phi_v = 2.2\%$. \diamond : data from Leptos et al. (2009). — : $\bar{\beta} = 0.5$, time-dependent. ---- : $\beta = 0.5$, steady. - - - - : $\bar{\beta} = 0.12$, time-dependent. $\cdots\cdots$: $\beta = 0.12$, steady.	173
11.10	PDF for tracer displacements at times $\Delta t = 0.3s$ (a), and $\Delta t = 2s$ (b), for $\phi_v = 0 - 15\%$	176
11.11	Effective diffusion coefficient of tracers (a) and mean squared displacement of swimmers (b) with $\phi_v = 0 - 15\%$	177
11.12	Squirmer-tracer pair distribution function $g(r, \theta)$ for $\beta = 0.5$. The white solid line represent the swimmer's radius. The white dashed line corresponds to the excluded volume region. The white arrow is the swimming direction.	177
12.1	Steady state orientation distribution around the mean unit director $\langle \mathbf{p} \rangle$ for $\beta = 0$ and $\beta = 1$. \ominus : simulation with $\beta = 0$. — : VMF fit with $\alpha = 68.7$. \boxminus : simulation with $\beta = 1$. — : VMF fit with $\alpha = 1.55$	181
B.1	System of N_p particles interacting via non-overlapping constraints along time. Periodic images are shown for convenience.	223
B.2	Minimal surface-surface distance $\min d_{nm}$ along time for three different values of the convergence criterion ε_{uza}	224
B.3	Number of Uzawa iteration per time step.	224
B.4	Initialization of a dense ($\phi_a = 0.63$) random suspension from an arbitrary seeding of particles.	225
B.5	Minimal surface-surface distance $\min d_{nm}$ along time for initially overlapping particles at high packing fraction $\phi_a = 0.63$	226
F.1	Angular rotation of the (x, y, z) coordinate system about the axis \mathbf{u} with an angle ϕ results in (x', y', z')	242

F.2	Angular integration of an oscillating object. ϕ is the angle formed between the object and $\hat{\mathbf{x}}$: $\phi = \cos^{-1}(\mathbf{p} \cdot \hat{\mathbf{x}}) = 2 \cos^{-1} q_0$	246
F.3	Spheroid in a shear flow $u_x = \dot{\gamma}y$	247
F.4	Angular integration of Jeffery orbits. ϕ is the angle between the principal axis of the spheroid and the $\hat{\mathbf{x}}$ -axis. —: analytical solution, $-\ominus$: \mathbf{p} with EE, \boxtimes : \mathbf{q} with DM.	249
F.5	$t/T = 92 - 100$. —: analytical solution, $-\ominus$: \mathbf{p} with AB4, \boxtimes : \mathbf{q} with DM.	250
G.1	Growth rate $\text{Re}(\sigma)$ over k and θ in a suspension of nearly aligned spherical pushers (no quadrupole). (a) Eq. (37) from Saintillan and Shelley (2008) with $\gamma = 0$ and $\alpha = -1$. (b) Eq. (G.46) with $b_2 = -1$. —: long-wave limit $k \rightarrow 0$, Eq. (G.47).	259
G.2	First moment $m_1(\alpha)$ of the VMF distributions. $\alpha = 68.7$ corresponds to the value fitted to match the orientational distribution for $\beta = 0$ in Section 12.2. $m_1(68.7) = 0.985$ match very well the steady state polar order parameter in our simulations $P^\infty = 0.98$	263
G.3	Growth rate $\text{Re}(\sigma)$ along θ for $m_1 = 3 \cdot 10^{-6} - 0.995$. The amplitude of the wave number is fixed to $k = 1$. The colorbar represents the rate of alignment m_1 . Results are shown for two different magnitudes of the degenerate quadrupole: (a) $b_1 = 1$, (b) $b_1 = -1$	270
G.4	Growth rate $\text{Re}(\sigma)$ along θ and $k = 0, 2, 4$ for $m_1 = 3 \cdot 10^{-6} - 0.995$. The colorbar represents the rate of alignment m_1 . The black curves (—) correspond to Eq. (G.46) for the monokinetic closure. Results are shown for (a) $b_2 = -1$, (b) $b_2 = 0$, (c) $b_2 = 1$	273
G.5	Growth rate $\text{Re}(\sigma)$ along θ for the long-wave limit $k = 0$. The colorbar represents the rate of alignment m_1 . ----: proposed scaling Eq. (G.109).	274

Introduction and theoretical background.

Nature exhibits a wide variety of swimming patterns at the micro-scale. The interactions between self-propelled micro-organisms, also called micro-swimmers, and the surrounding fluid are complex. This complexity is well illustrated by the diversity of intricate phenomena. Some micro-swimmers stir the surrounding fluid in a non-intuitive way ([Purcell \(1977\)](#)), others swim against the flow in the presence of boundaries ([Roberts \(1970\)](#)). On larger scales, suspensions of bacteria or sperm cells organize into large coherent structures whose sizes and dynamics exceed the characteristic magnitude for one individual. This coherent motion is called “collective motion”. What makes these phenomena even more complex is the coupling between length scales. What happens on large scales depends on sophisticated mechanisms occurring two or three orders of magnitude below. Understanding these phenomena and the underlying physics is of fundamental importance, not only for the sake of knowledge, but also for a wide variety of applications, among which, nano-technologies, health issues, medicine, fertility, ecology, fishing industry or biofuel productions.

To address this complexity, scientists combine experiments with theoretical approaches. Researchers and engineers perform experimental studies on swimming mechanisms and active suspensions to evidence new phenomena and design bioinspired self-propelled micro- and nano-devices, which hold promising applications for nano-technologies and medicine.

These important advances need to be assisted by theoretical and numerical studies. Theory allows to isolate mechanisms and go beyond experimental capacities. The scientific discipline which studies the relative motion between living micro-organisms and fluids is called Biofluidmechanics ([Lighthill \(1976\)](#)). The fluid mechanics of locomotion at small scales has been investigated mathematically for more than 60 years. The pioneering models of Taylor in 1951 ([Taylor \(1951\)](#)), on flagellar beating, and Lighthill in 1952 ([Lighthill \(1952\)](#)), on ciliary propulsion, are still actively used nowadays. Collective motion has been investigated for approximately 30 years. In the early 80’s, Stephen Childress ([Childress \(1981\)](#)) and John Kessler ([Kessler \(1984\)](#)) investigated the mechanisms responsible for the formation of bioconvection patterns in cultures of algae. Continuum models, based on kinetic theory for dilute suspensions, appeared in the late 80’s ([Kessler \(1986\)](#); [Pedley et al. \(1988\)](#)) with the same purpose: model bioconvection to understand the origin of flow instabilities. Since the late 90’s, theoretical and numerical works tried

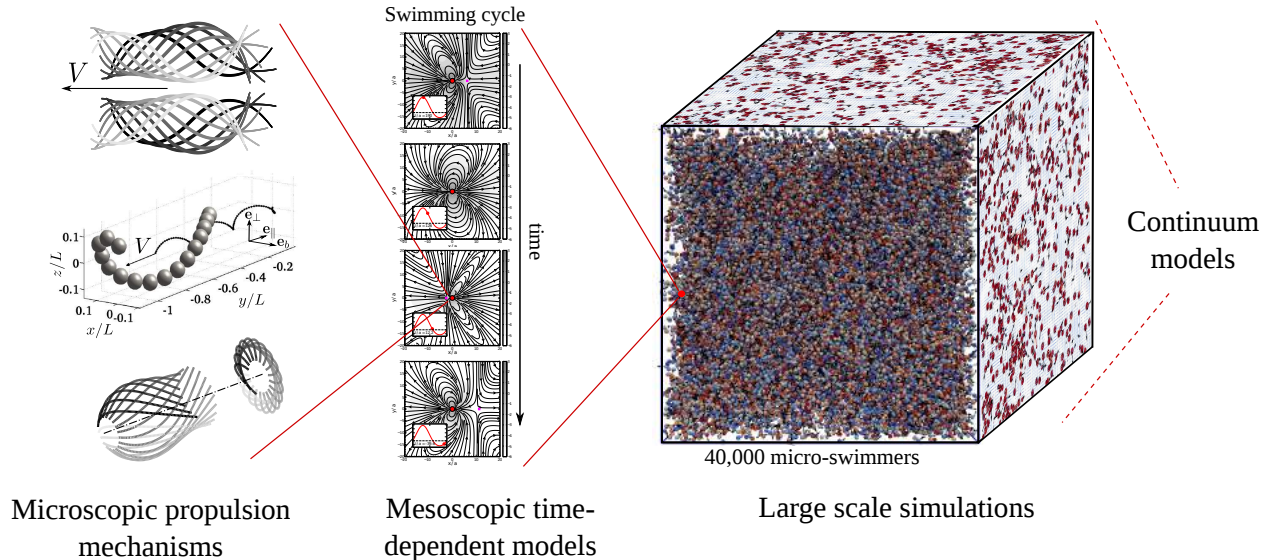


Figure 1: Pathway of the thesis: we first focus on the details of swimming mechanisms, then change scale with mesoscopic models that we incorporate in large scale simulations to address the physics of active suspensions at the lab scale.

to provide a better description of the phenomena involved in active suspensions by combining length scales in particle-based simulations. The length scales involved in active suspensions span several orders of magnitudes: the smallest micro-swimmers, swimming appendages and tracer particles used in experiments are typically micron-sized ($10^{-6}m$), collective motion and/or mixing occur at larger scales ($10^{-5} - 10^{-4}m$), while typical sample sizes or interrogation windows at the lab/*in situ* scale can reach several millimeters ($10^{-3}m$). Modeling such systems thus requires addressing both the physics at the small scales, where Brownian motion plays an important role, and at the large scales, where several thousands ($10^3 - 10^5$ and more) individuals are involved.

To introduce the pathway we will follow along this thesis, we quote Eric Lauga and Thomas Powers in their exhaustive review (Lauga and Powers (2009)): “A further challenge will be to integrate the understanding of basic mechanisms across multiple scales, from the levels of molecular motors to individual cells to large populations of cells.”

Not many numerical methods can afford to take this challenge yet. The goal of this Ph.D is thus to provide a contribution in this direction. Along the thesis we try to develop a modeling approach that accounts for the swimming mechanisms at the scale of the micro-organism in order to shed light on the phenomena occurring at the lab/*in situ* scale.

Context of the Ph.D

This Ph.D partly belongs to the ANR MOTIMO project. MOTIMO stands for ‘MOTility Imaging and Modeling’. This scientific, collaborative and multidisciplinary project

focuses on ovine sperm fertility. Ovine sperm is an example of dense suspensions which exhibit collective motion. When looking at a drop of ram sperm in a phase contrast microscope, one observes large coherent structures which contain thousands of sperm cells. In the artificial insemination industry, the motion of these structures is called Massal Motility. It has been shown that Massal Motility is positively correlated to fertility. It is thus used to score ejaculates. However, the scoring is done by one observer, based on his subjective evaluation criteria. In order to make this procedure more rigorous, efficient and reproducible, the MOTIMO project aims at developing a tool which systematizes the evaluation of the motility of an ovine sperm sample within an operational time frame.

The MOTIMO project gathers several structures, the Institut de Mécanique des Fluides de Toulouse (IMFT) and the Institut de Mathématiques de Toulouse (IMT) in Toulouse, the Institut National de la Recherche Agronomique de Tours (INRA Tours), the Laboratoire d'Informatique, Signaux et Systèmes de Sophia-Antipolis (I3S) in Nice, the Department of Mathematics at Imperial College in London and a transnational company, IMV-Technologies, the world leader in the reproduction biotechnologies.

The whole project, which should lead to an industrialized process, is supervised by IMV-Technologies. The Laboratoire de Physiologie de la Reproduction et du Comportement of INRA-Tours is in charge of the microscope measurements and of the process validation through the realization of an artificial insemination campaign with scored samples. The IMFT performs complementary experiments, and is in charge of the processing of the collected images, through the dual use of Particle Imaging Velocimetry (PIV) and Optical Flow Reconstruction (OFR) techniques. The I3S of Sophia-Antipolis is in charge of the learning-scoring step, which, from the reconstructed flows, should provide an automatic score of the considered sample. The IMT and Imperial College take care of the continuum modeling issues, which should lead to a detailed understanding and a better flow reconstruction.

My Ph.D aims at providing a broader fluid mechanics picture to the modeling part of this project. The particle-based models developed in this thesis address both the modeling of swimming mechanisms and collective motion in dense active suspensions. The preliminary study on continuum models carried out during this Ph.D. is also part of the mathematical modeling section of the MOTIMO project.

This work also results from a 1.5 years collaboration with Pr. Eric Keaveny, Lecturer in the Department of Mathematics at Imperial College. His expertise in the modeling of active and Brownian suspensions fits squarely within the scope of this Ph.D and has provided invaluable help over the course of this work.

Before outlining the content of this manuscript, we shortly remind the basics and derive the set of equations necessary to study the fluid mechanics of active particles.

The motion of active particles in flows

Consider N_p swimmers with mass m_p and moment of inertia I_p suspended in a fluid. The dynamics of each swimmer n follows Newton's second law

$$m_p \frac{d\mathbf{V}^n}{dt} = \mathbf{F}_h^n + \mathbf{F}_{ext}^n, \quad (1)$$

$$I_p \frac{d\mathbf{\Omega}^n}{dt} = \boldsymbol{\tau}_h^n + \boldsymbol{\tau}_{ext}^n. \quad (2)$$

\mathbf{V}^n and $\mathbf{\Omega}^n$ correspond to the translational and rotational particle velocities. \mathbf{F}_h^n and $\boldsymbol{\tau}_h^n$ are the hydrodynamic force and torque acting on particle n . \mathbf{F}_{ext}^n and $\boldsymbol{\tau}_{ext}^n$ correspond to the sum of external forces and torques applied on particle n . They may correspond to contact forces, magnetic fields, Brownian collisions or bottom-heavy torques among others. Note that if Brownian forces and torques are included in \mathbf{F}_{ext}^n and $\boldsymbol{\tau}_{ext}^n$, Eq. (1) - (2) are called "stochastic Langevin equations". Indeed, the Brownian forcing is stochastic due to the random collisions of solvent molecules.

Newton's second law Eq. (1) - (2) cannot be solved without the help of fluid mechanics to compute the hydrodynamic forces and torques.

Fluid mechanics: hydrodynamic forces and torques

Most of the swimming micro-organisms live in an aqueous medium which contains polymers, proteins and many other molecules. Non-Newtonian fluid mechanics are often necessary to model the complex interplay between the swimmers and these surrounding media. This area has increasingly been investigated over the last ten years, theoretically (Lauga (2007); Teran et al. (2010); Li et al. (2014) among others) and experimentally (Shen and Arratia (2011); Liu et al. (2011); Espinosa-Garcia et al. (2013); Godínez et al. (2015)). An exhaustive review is provided in Elfring and Lauga (2015).

For the sake of simplicity, the framework of this Ph.D thesis is based on Newtonian fluids.

The motion of the fluid surrounding the micro-swimmers is given by the incompressible Navier-Stokes equations for a Newtonian fluid:

$$\begin{aligned} \rho_f \left(\frac{\partial \mathbf{u}}{\partial t} + (\mathbf{u} \cdot \nabla) \mathbf{u} \right) &= \nabla p - \eta \nabla^2 \mathbf{u} \\ \nabla \cdot \mathbf{u} &= 0. \end{aligned} \quad (3)$$

subject to no-slip boundary conditions on the surface S^n of each particle n

$$\mathbf{u}(\mathbf{x}) = \mathbf{V}^n + \mathbf{\Omega}^n \times (\mathbf{x} - \mathbf{Y}^n) + \mathbf{u}_S^n(\mathbf{x}), \quad \mathbf{x} \in S^n, \quad (4)$$

where ρ_f is the volumetric mass density of the fluid and \mathbf{Y}^n is the position of the center of mass of particle n . \mathbf{u}_S^n is a prescribed swimming gait at the surface of swimmer n , which correspond to surface distortions or appendage actuation.

Here, we consider a quiescent fluid in an unbounded domain. Therefore, the fluid velocity must vanish at infinity¹

$$\mathbf{u}(\mathbf{x}) \rightarrow 0, \text{ when } \mathbf{x} \rightarrow \infty. \quad (5)$$

The fluid stress tensor is

$$\boldsymbol{\sigma} = -p\mathbf{I} + \eta (\nabla\mathbf{u} + (\nabla\mathbf{u})^T), \quad (6)$$

and is used to compute the hydrodynamic force acting on each particle

$$\mathbf{F}_h^n = \int_{S^n} \boldsymbol{\sigma} \cdot \mathbf{n} dS, \quad (7)$$

where \mathbf{n} is the unit vector normal to S^n . The hydrodynamic torque is similarly given by

$$\boldsymbol{\tau}_h^n = \int_{S^n} (\mathbf{x} - \mathbf{Y}^n) \times \boldsymbol{\sigma} \cdot \mathbf{n} dS. \quad (8)$$

The realm of zero Reynolds number

We can nondimensionalize the Navier-Stokes equations for the fluid phase

$$\begin{aligned} \text{Re} \left(\frac{\partial\mathbf{u}}{\partial t} + (\mathbf{u} \cdot \nabla)\mathbf{u} \right) &= \nabla p - \eta \nabla^2 \mathbf{u} \\ \nabla \cdot \mathbf{u} &= 0. \end{aligned} \quad (9)$$

The Reynolds number, $\text{Re} = \frac{\rho_f U L}{\eta}$, compares the contribution of the fluid inertia with the viscous dissipation. At low Re, velocity disturbances diffuse more rapidly than the rate at which fluid particles are transported by the flow. The characteristic length of swimming micro-organisms is $L \approx 1 - 100 \mu\text{m}$. Their swimming speed is $U \approx 10 - 10^3 \mu\text{m} \cdot \text{s}^{-1}$. In water ($\rho_f \approx 10^3 \text{kg} \cdot \text{m}^{-3}$, $\eta = 10^{-3} \text{Pa} \cdot \text{s}$), the typical Reynolds number associated to a micro-swimmer is $\text{Re} \approx 10^{-5} - 0.1$. The limit $\text{Re} = 0$ is therefore a reasonable approximation. In such case, the Navier-Stokes equations simplify to the Stokes equations

$$\begin{aligned} \nabla p - \eta \nabla^2 \mathbf{u} &= 0 \\ \nabla \cdot \mathbf{u} &= 0. \end{aligned} \quad (10)$$

The Stokes number, St, compares the particle relaxation time τ_p with the particle advection time scale $\text{St} = \tau_p/(L/U)$. $\tau_p = m_p/\zeta$, where ζ is the friction coefficient due to the effect of viscous stresses acting on the particle. ζ is proportional to the viscosity: $\zeta \sim \eta L$. The particle relaxation time scale thus follows $\tau_p \sim m/\eta L$. The mass of the aforementioned micro-organisms is typically $m_p \approx 10^{-16} - 10^{-13} \text{kg}$ and $L/U \approx 1$. The resulting Stokes number is very small $\text{St} \approx 10^{-7} - 10^{-4}$. Therefore, we can eliminate the inertial terms in Newton's second law

$$\mathbf{F}_h^n + \mathbf{F}_{ext}^n = 0, \quad (11)$$

$$\boldsymbol{\tau}_h^n + \boldsymbol{\tau}_{ext}^n = 0. \quad (12)$$

Eq. (11) states that micro-swimmers are force- and torque-free.

¹Unless the suspensions fills the entire space.

Solving the complex swimming problem with hydrodynamic interactions: a modeling and computational challenge

Eq. (10) subject to boundary conditions Eqs. (4)-(5), together with Eqs. (11)-(12) and Eq. (7) - (8) form a set of coupled equations where the unknowns are the swimmers' velocities \mathbf{U}^n and rotations $\mathbf{\Omega}^n$. Solving the full set for large collections of active particles is difficult and very costly. Depending on the scale considered, several reasonable approximations can help simplifying the problem.

In this thesis we address various levels of complexity. Our goal is to find the strategy which provides the optimal balance between accuracy, flexibility and computational efficiency to investigate the intricate dynamics of active suspensions.

Outline

The manuscript is organized into three parts, each divided into four chapters.

Part I is devoted to the study of self-propulsion at the scale of the micro-swimmer. The problem of locomotion at small scales has been extensively addressed both theoretically and experimentally over the last decades. In Chapter 1, we briefly present the standard mechanisms of swimming motility and explain how Nature has been a great source of inspiration for the design of artificial micro-swimmers.

Recent modeling efforts result in accurate methods that provide a good insight on the mechanisms of motility. Among them, the bead model and blob-like approaches provide a flexible, yet efficient, tool to address complex shapes and their mechanical properties. In Chapter 2, we propose an improvement of the bead model. We develop a flexible and versatile framework to enforce constraints to connect beads together. The resulting method is generic, easy to implement, numerically stable and compares well with the literature.

In Chapter 3, we switch to the mesoscopic scale by coarse-graining the representation of the swimming micro-organisms. We show that the well-known squirmer model adapts very well to breaststroke swimming by making its singularity time-dependent and by tuning their magnitude with experimental data. The proposed technique offers an interesting framework to combine experiments, theory and numerical simulations for the study of swimming mechanisms, and extends efficiently to large scale simulations of active suspensions.

Chapter 4 proposes future directions and list ongoing works for the models developed in Part I.

Part II focuses on the numerical tools developed to address the multiscale physics of active suspensions.

Coupling different scales spanning over several order of magnitudes is not an easy task. In Chapter 5 we present the state-of-the-art methods to simulate active suspensions and to incorporate Brownian motion. The main difficulties encountered by the community lie in the computational cost to compute hydrodynamic interactions, the accurate description

of the disturbances generated by the micro-swimmers, and the time-integration of the overdamped stochastic equations arising from random Brownian motion.

Chapter 6 proposes a methodology, built on the force-coupling method (FCM) framework, to extend the mesoscopic model derived in Chapter 3 to large deterministic simulations of active suspensions in the context of High Performance Computing. The very good agreement with the literature and the good scaling of the code prove the robustness of the method to accurately handle large collections of swimmers.

The incorporation of Brownian motion is addressed in Chapter 7. Using the framework of fluctuating FCM, we derive a new time-integration scheme, the Drifter-Corrector, to efficiently handle the drift term arising in the overdamped limit of Langevin equations for particle motion. We show that our scheme reduces the computational cost by, at least, a factor two compared to the state-of-the-art integration schemes for such systems. We illustrate its efficiency with large scale simulation of gelation and aggregation processes in colloidal suspensions.

Chapter 8 explains how to combine these tools to simulate active Brownian suspensions. More details are provided in Appendix E.

The physics of active suspensions is investigated in Part III.

In Chapter 9 we explicit the ubiquitous nature of active matter and provide a short overview on the physical phenomena involved in active suspensions, to discuss their potential applications and consequences on ecology, medicine, reproduction and nanotechnologies among others.

Chapter 10 investigates the dynamics of the strong orientational correlations observed in numerical simulations of interacting squirmers and in suspensions of synthetic self-propelled droplets. Using the full capacity afforded by the method developed in Chapter 6, we perform large scale simulations involving tens of thousands of micro-swimmers. We reveal that the polar ordering is purely due to pairwise interactions that generate alignment in the near field. We also provide a thorough characterization of the polar order instability. These results highlight the effectiveness of our approach to achieve near continuum-level results, allowing for better comparison with experimental measurements while complementing and informing continuum models. We simulate suspensions of spheroidal swimmers and demonstrate the new implementation of time-dependent swimming gaits developed in Chapter 3. We also present preliminary results showing the effect of time-dependence on suspension properties.

In Chapter 11 we incorporate the method developed in Chapter 7 for Brownian motion to address the complex problem of enhanced tracer diffusion in dilute and concentrated active suspensions. We find a quantitative agreement with the experiments of [Leptos et al. \(2009\)](#) and confirm various results from the literature dealing with dilute suspensions. Simulations for higher volume fractions provide promising results on the nonlinear response of enhanced particle diffusivity in concentrated active suspensions. Such achievement is new in the literature and comparisons with experiments ([Kurtuldu et al. \(2011\)](#)) are close at hand.

Chapter 12 summarizes the results of Part III and introduces recent attempts to investigate the polar order instability with continuum models. Detailed calculations are provided

in Appendix G.

The last part summarizes the results obtained over the course of the thesis and suggest future directions to adapt the multiscale modeling of active suspensions to more realistic configurations.

Publications related to this work

The content of this thesis partially appears in published or submitted papers which are listed below in chronological order:

1. Delmotte, B., Climent, E. and Plouraboué, F. (2013). Hydrodynamic interactions among large populations of swimming micro-organisms. *Computer Methods in Biomechanics and Biomedical Engineering*, 16(sup1), 6-8.
2. Delmotte, B., Climent, E. and Plouraboué, F. (2015). A general formulation of Bead Models applied to flexible fibers and active filaments at low Reynolds number. *Journal of Computational Physics*, 286, 14-37.
3. Delmotte, B., Keaveny, E., Plouraboué, F. and Climent, E. (2015). Large-scale simulation of steady and time-dependent active suspensions with the force-coupling method. *submitted to Journal of Computational Physics*, ArXiv:arXiv preprint arXiv:1501.02912.
4. Delmotte, B. and Keaveny, E. (2015). Time integration for particle Brownian motion determined through fluctuating hydrodynamics, *submitted to Journal of Chemical Physics* .

Part I

Swimming Mechanisms at Small Scales

Chapter 1

Introduction: understanding locomotion at microscales and its consequences

Contents

1.1	Short overview of swimming mechanisms	11
1.2	Why swimming mechanisms are interesting to study?	14
1.2.1	Design and optimization of micro-robots	14
1.2.2	Biology and ecology	15
1.3	How to model these mechanisms ?	16

Swimming mechanisms in the realm of Stokes flows are impressively diverse. Microorganisms or manufactured artificial micro-swimmers use a wide variety of non-reciprocal swimming gaits for their locomotion. Section 1.1 offers a glimpse of the mechanisms of swimming motility in nature. We then explain in Section 1.2 why these mechanisms draw the attention of different communities, ranging from medicine and biology to fluid mechanics, robotics and engineering. Finally, we briefly summarize the modeling efforts in this area and raise the questions that will be addressed in Chapter 2 and Chapter 3.

1.1 Short overview of swimming mechanisms

Many specific mechanisms of swimming motility were reported (Lauga and Powers (2009)). For the sake of conciseness, we will only focus on two main categories of swimming patterns: ciliary and flagellar beating.

Ciliary beating is an asymmetric beating pattern of an actuated filament that decomposes into two phases. During the first phase, called the power stroke, the swimmer bends the appendage at the base and sweep it back to pull the fluid behind it. In the second phase, the recovery stroke, the appendage folds to reduce the drag and goes back

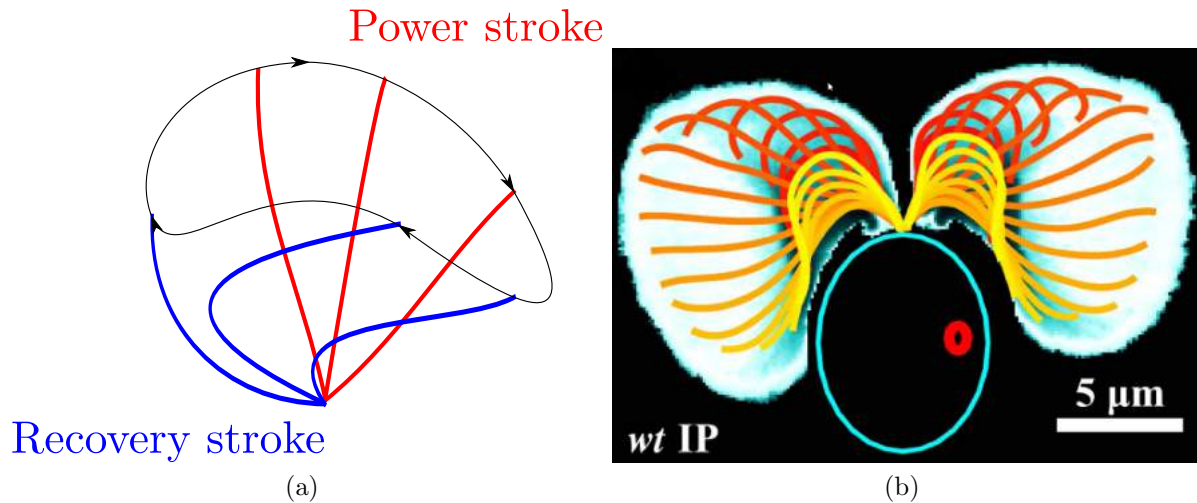


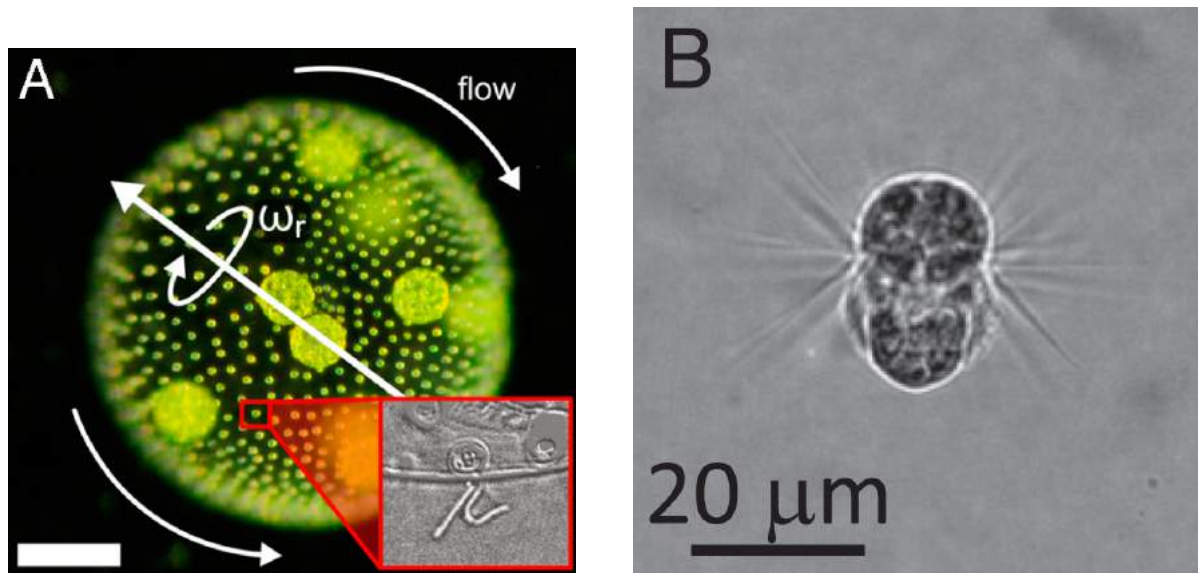
Figure 1.1: (a) Ciliary beating pattern decomposed into a **power stroke** and a **recovery stroke**. (b) *Chlamydomonas reinhardtii* uses ciliary beating to perform breaststroke swimming with its anterior appendages. Figure extracted from [Leptos et al. \(2013\)](#).

to its initial position (see Figure 1.1a). Algal cells such as *Chlamydomonas reinhardtii* (Figure 1.1b), but also zooplankton such as copepods in their naupliar stage ([Wadhwa et al. \(2014\)](#)), use this pattern to perform breaststroke swimming with their anterior appendages. The appendages can either be flagella (*Chlamydomonas reinhardtii*) or arms (plankton). Those organisms are called pullers.

Other micro-organisms use this beating pattern to propel by undulating an array of thousands of cilia in a coordinated manner at their surfaces (so-called metachronal waves). *Volvox* ([Drescher et al. \(2010\)](#); [Brumley et al. \(2012, 2014\)](#)), shown on Figure 1.2a, *Opalina* and *Paramecium* are well-known examples. The zooplankton *Mesodinium rubrum* ([Kiørboe et al. \(2014\)](#)), which forms red massive blooms in coastal areas, is less famous in the Fluid Mechanics community (Figure 1.2b). Arrays of beating cilia can also be found in the respiratory epithelium where they sweep away dust and aerosol particles. Recent experiments also showed that corals use such arrays to generate feeding currents ([Shapiro et al. \(2014\)](#)).

Flagellar beating consists in the propagation of bending waves along one or several flagella to push the fluid away from the rear of the body (those organisms are called pushers). Sperm cells use internal motors distributed regularly along their flexible flagellum to perform a whip-like motion. Their beating can either be planar or helical, depending on the confinement and the nature of the surrounding fluid ([Gaffney et al. \(2011\)](#)). Figure 1.3 shows the planar beating of a human sperm in a highly viscous liquid. When exposed to bright light *C. reinhardtii* adopts a similar pattern by propagating bending waves away from the cell body ([Mitchell \(2000\)](#)).

Bacteria such as *E. coli* propels by helical actuation of a stiff appendage with a motor at the cell wall. *B. subtilis* swims by using flagella, which are situated around their oblong bodies. Other micro-swimmers proved that swimming does not necessarily needs



(a) Photograph of *Volvox Carteri*. The inset shows one pair of cilia in a somatic cell (green dots on the main figure). Figure extracted from [Drescher et al. \(2010\)](#).

(b) *Mesodinium rubrum* with equatorial “belt” of cilia. Figure extracted from [Kjørboe et al. \(2014\)](#).

Figure 1.2: Examples of micro-swimmers using ciliary propulsion on their surface.

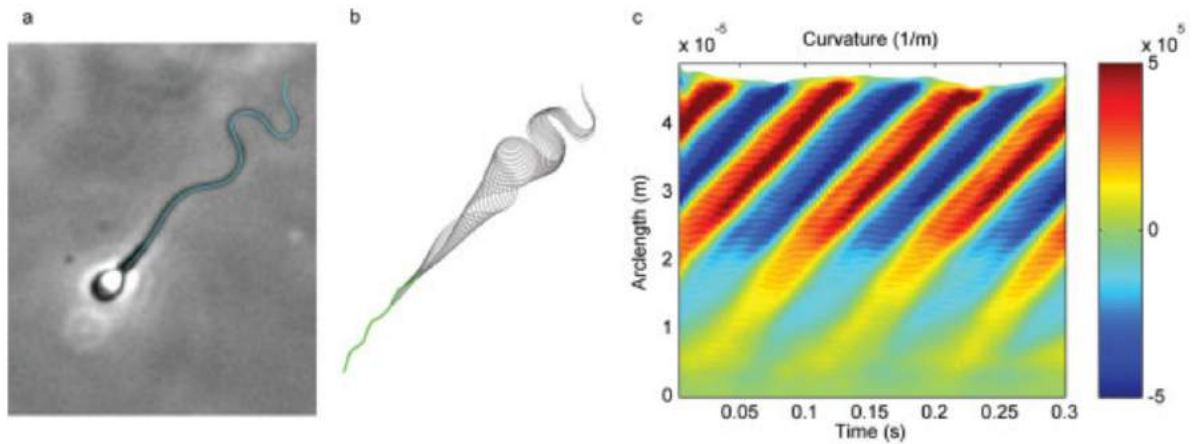


Figure 1.3: Propagation of bending waves along the flagellum of human sperm in a highly viscous liquid. Figure extracted from [Smith et al. \(2009\)](#)

appendages. *Spiroplasma* (Shaevitz et al. (2005)) as well as nematodes (Majmudar et al. (2012)) use planar or helical deformation of their body to self-propel.

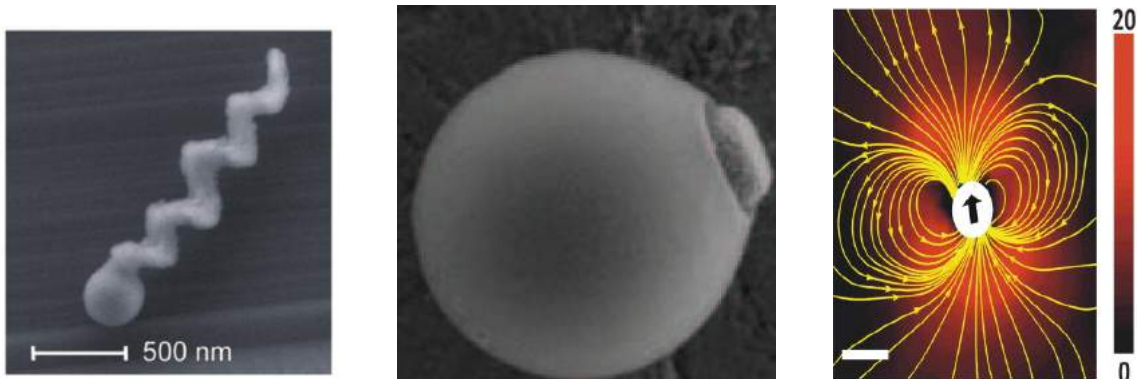
1.2 Why swimming mechanisms are interesting to study?

1.2.1 Design and optimization of micro-robots

Understanding the mechanisms responsible for locomotion at low Reynolds number is useful for the optimization and design of micro-robots (Keaveny et al. (2013); Montenegro-Johnson and Lauga (2014, 2015)). The main objective in this research area is to develop minimally invasive medicine, which confers a number of advantages to the patient, including reduced recovery time, infection risks and drug side-effects. The synthetic micro- and nano-devices designed nowadays are expected to perform drug delivery and cargo transport, advanced telemetry or bloodless surgery in the near future (Fischer and Ghosh (2011); Xi et al. (2013)). Many bioinspired micro-devices have been manufactured over the last decade. Most of them are actuated by an external oscillatory magnetic field. More recently, autophoretic particles, involving chemical reactions with the solvent, have been increasingly investigated.

Artificial micro-swimmers made of magnetic beads articulated with elastic bonds mimic flagellar beating to perform cargo transport (Dreyfus et al. (2005)). Magnetic helical rigid devices (Figure 1.4a) use the anisotropic coupling between rotation and translation to perform similar tasks (Zhang et al. (2009); Ghosh and Fischer (2009); Tottori et al. (2012)). Carpets of magnetic micro-rods are used to investigate the efficiency and the transport properties of beating arrays of cilia (Vilfan et al. (2010); Coq et al. (2011)).

Self propulsion can also be performed with chemical reactions. Suspended colloidal particles interacting chemically with a solute are able to self-propel by autophoretic motion (Michelin et al. (2013)). The resulting osmotic flow generates a slip velocity on their surface that can be thought as the “artificial equivalent” of the tangential velocity generated by ciliated micro-organisms (Michelin and Lauga (2013)). Figure 1.4b shows an example of autophoretic particle (Palacci et al. (2013)). Self-propelled liquid microdroplets use chemical reaction to induce Marangoni stresses (Thutupalli et al. (2011); Izri et al. (2014)). As shown on Figure 1.4c, the flow field they generate is similar to the one of ciliated micro-swimmers or autophoretic particles. It is worth mentioning that the self-propelled droplets of Izri et al. (2014) are able to carry external bodies such as large colloids, salt crystals, and even cells. This is a real breakthrough because these droplets are fully biocompatible and constitute the simplest realization of spontaneous motion in a system of isotropic particles.



(a) Magnetic helical swimmer designed by Ghosh and Fischer (2009).

(b) Photograph of the light-activated autophoretic swimmer designed by Palacci et al. (2013). This swimmer is rheotactic (Palacci et al. (2015)).

(c) Flow field around a self-propelled droplet (Thutupalli et al. (2011)).

Figure 1.4: Examples of artificial micro-swimmers.

1.2.2 Biology and ecology

Biologists and ecologists try to get a comprehensive view on how micro-swimmers interact with their environment (Gaffney et al. (2011); Guasto et al. (2012)). The hydrodynamic disturbances induced by a micro-organism on the surrounding fluid, either by swimming or generating feeding currents, can affect, not only its locomotion, but also its exposure to predators which are equipped with mechanical sensors (Kiørboe et al. (2014)). Experimental works evidenced the anomalous diffusion and fluid mixing hydrodynamically induced by micro-swimmers (Leptos et al. (2009); Kurtuldu et al. (2011))¹.

Vice-versa, the properties of the surrounding medium also influence the motility. At the level of individual micro-swimmers, the ocean or human body are seas of gradients (Stocker (2012)). Environmental stimuli such as chemical gradients (chemotaxis), temperature gradients (thermotaxis), light gradients (phototaxis) or flow gradients (gyrotaxis and rheotaxis) can shape their trajectory and affect their motility. Rheotaxis of undulatory swimmers has sparked much interest over the last few years (Fu et al. (2012); Kantsler et al. (2014); Tung et al. (2014); Ishimoto and Gaffney (2015); Tung et al. (2015a); Yuan et al. (2015)). Recent experimental work (Palacci et al. (2015)), echoed by numerical studies (Uspal et al. (2015)), showed that autophoretic particles also exhibit a positive rheotactic behavior: when exposed to velocity gradients in a bounded flow, they tend to swim upstream, mostly along the boundaries. The role of rheotaxis vs. peristalsis on sperm migration in the female track is still an open question (Roberts (1970)). A very nice recent experimental work (Tung et al. (2015b)) proved that the flow in the female track facilitates the sperm migration towards the site of fertilization while sweeping pathogens downstream.

¹See Part III for a numerical investigation of enhanced tracer diffusion in active suspensions.

The rheology of the fluid is also known to affect the locomotion of swimming micro-organisms. However, non-Newtonian fluids are not in the scope of this thesis. We refer the reader to the recent review by (Elfring and Lauga (2015)).

While experimental studies bring out new phenomena and, sometimes, provide physical explanations, modeling remains essential to explore and control the parameter space, suggesting new experiments and assisting the design of new devices.

1.3 How to model these mechanisms ?

Even in the “simple” Newtonian case, solving the complex problem of fluid-structure interactions is not an easy task. One has to include the internal mechanics, i.e. the elastic response to deformation and active bending, but also hydrodynamic interactions. Many different methods have been proposed to tackle this problem. The choice of the appropriate method depends on

- the geometry of the objects considered,
- their number,
- the level of accuracy required for elastic coupling and hydrodynamic interactions.

If the kinematics of an isolated swimmer is prescribed, its velocity and rotation can be obtained exactly with the reciprocal theorem (Stone and Samuel (1996)). Elongated swimmers (e.g. sperm cells, spirochetes,...) can be modeled with techniques commonly used for immersed fiber in viscous flows: resistive force theory (Hancock (1953); Gray and Hancock (1955); Lighthill (1976)) and slender body theory (Hancock (1953); Lighthill (1976); Johnson and Brokaw (1979)). Non-slender shapes require more sophisticated approaches such as boundary element methods (Pozrikidis (1992)). Both cases can be handled with the bead model (Rouse Jr (1953)) and multi-blob approaches (immersed boundaries (Peskin (2002)), force-coupling method (Maxey and Patel (2001)), regularized stokeslets (Cortez (2001))). By assembling collections of spheres (or blobs) with constraint and elastic forces, these methods provide a flexible framework to approximate the shape and the mechanical properties of complex objects. However, handling constraint forces in flexible bead (or blob) assemblies requires special care and may be challenging from a computational point of view.

In Chapter 2, we list and discuss these methods, and propose a simple formulation of the bead model which is generalized to rigid and flexible bodies either active or passive. We provide a generic formulation based on non-holonomic constraints and propose a contact model to handle flexible bead assemblies. The versatility of the method allows to simulate objects of complex shapes subject to different types of actuation mechanisms. Unlike slender body theory, there is neither limitations on the object’s aspect ratio nor need to solve the complex nonlinear equations coupling elastic and fluid stresses. When comparing bead model predictions in various configurations, we find good agreement with

experimental and numerical results in the literature. Going further, we have shown in a recent study (Thiam (2014)) that the linearity of the model provides an exact inverse modeling method for the calibration of constitutive parameters of passive or active flexible objects.

Even though the bead model and equivalent approaches accurately reproduce the detailed features of swimming micro-organisms, including them in simulations containing thousands of individuals is too costly. Modeling arrays of beating cilia is also very complex. Some successful efforts have been made in this direction using the bead model on flat surfaces (Osterman and Vilfan (2011)), but they cannot be used to model several interacting individuals. Instead, one can use a coarse-grained representation of the swimmer. The simplest approach is to model it as a force dipole without considering the actual boundary conditions at its surface nor its shape. Other models, more sophisticated, approximate the swimming gait with appropriate singularities which can be tuned with experimental measurements. This is the goal of a simplified mesoscopic model which has been proposed for ciliary propulsion: the squirmer model (Lighthill (1952); Blake (1971); Ishikawa et al. (2006)). A squirmer is a swimmer that prescribes constant tangential and radial velocities on its surface. Surface velocities are written in terms of infinite series of Legendre polynomials whose magnitude correspond to squirming modes. The resulting flow corresponds to the time-averaged disturbances created by ciliary beating over one period. With minor modifications, the mesoscopic squirmer model is also able to reproduce the slip velocity on the surface of autophoretic particles (Nishiguchi and Sano (2015)) or self-propelled droplets (Thutupalli et al. (2011)). The squirmer model has been widely used to investigate the behavior of an isolated or a pair of steady (i.e. period-averaged) swimmers (Doostmohammadi et al. (2012); Wang et al. (2012); Michelin and Lauga (2013); Zhu et al. (2013)).

Recent experiments (Guasto et al. (2010); Wadhwa et al. (2014); Kiørboe et al. (2014), and viewpoints (Saintillan (2010b)), suggest that modeling the flow generated by time-dependent swimming gait might be more realistic and should be included in mathematical models and computer simulations.

In Chapter 3 we show that the mesoscopic squirmer model can be used to model effective swimming gaits of real micro-swimmers as well as the hydrodynamic disturbances they generate along their beating pattern. The surface modes of the squirmer model are matched with a regularized singularity distribution, using a blob approach called the force-coupling method (FCM). Using experimental micro-PIV measurements, an automated algorithm is proposed to calibrate the squirming modes to make them time-dependent and thus reproduce the oscillatory flow around breaststroke swimmers. The proposed technique offers an interesting framework to combine experiments, theory and numerical simulations for the study of swimming mechanisms, and extends efficiently to large scale simulations of active suspensions.

Chapter 2

A general formulation of bead models applied to flexible fibers and active filaments at low Reynolds number.

Contents

2.1	Introduction	20
2.2	The bead model	22
2.2.1	Detailed review of previous bead models	22
2.2.2	Generalized forces, virtual work principle and Lagrange multipliers	26
2.2.3	The gears model	28
2.2.4	Elastic forces and torques	30
2.2.5	Hydrodynamic coupling	32
2.2.6	Numerical implementation	33
2.3	Validations	37
2.3.1	Jeffery orbits of rigid fibers	37
2.3.2	Flexible fiber in a shear flow	38
2.3.3	Settling fiber	41
2.3.4	Actuated filament	42
2.3.5	Planar swimming nematode	47
2.3.6	Cooperative swimming	50
2.3.7	Spiral swimming	52
2.4	Conclusions	54
2.5	Addendum: correspondence between \mathcal{M} and \mathcal{M}^*	54

Remark: this chapter is directly extracted from the eponymous paper. Several modifications have been made to incorporate it in the manuscript. We propose a general framework using Lagrange multipliers for the simulation of fiber dynamics at low Reynolds number based on bead models (BM). This formalism provides an efficient method to account for kinematic constraints. We illustrate, with several examples, to which extent the proposed formulation offers a flexible and versatile framework for the quantitative modeling of flexible fibers deformation and rotation in shear flow, the dynamics of actuated filaments and the propulsion of active swimmers. Furthermore, a new contact model called gears model is proposed and successfully tested. It avoids the use of numerical artifices such as repulsive forces between adjacent beads, a source of numerical difficulties in the temporal integration of previous bead models.

2.1 Introduction

The dynamics of solid-liquid suspensions is a longstanding topic of research while it combines difficulties arising from the coupling of multi-body interactions in a viscous fluid with possible deformations of flexible objects such as fibers (Lindner and Shelley (2014)). A vast literature exists on the response of suspensions of solid spherical or non-spherical particles due to its ubiquitous interest in natural and industrial processes. When the objects have the ability to deform many complications arise. The coupling between suspended particles will depend on the positions (possibly orientations) but also on the shape of individuals, introducing intricate effects of the history of the suspension.

When the aspect ratio of deformable objects is large, those are generally designated as fibers. Many previous investigations of fiber dynamics, have focused on the dynamics of rigid fibers or rods (Cox (1971); Meunier (1994)). Compared to the very large number of references related to particle suspensions, lower attention has been paid to the more complicated system of flexible fibers in a fluid.

Suspension of flexible fibers are encountered in the study of polymer dynamics (Yamakawa (1970); Yamanoi et al. (2010)) whose rheology depends on the formation of networks and the occurrence of entanglement. The motion of fibers in a viscous fluid has a strong effect on its bulk viscosity, micro-structure, drainage rate, filtration ability, and flocculation properties. The dynamic response of such complex solutions is still an open issue while time-dependent structural changes of the dispersed fibers can dramatically modify the overall process (such as operation units in wood pulp and paper industry, flow molding techniques of composites, water purification). Biological fibers such as DNA or actin filaments have also attracted many researches to understand the relation between flexibility and physiological properties (Jian et al. (1997)).

Flexible fibers do not only passively respond to carrying flow gradients but can also be dynamically activated. Many micro-organisms that self-propel in a fluid utilize a long flagellum connected to the cell body. Spermatozoa (and more generally one-armed swimmers) swim by propagating bending waves along their flagellum tail to generate a net translation using cyclic non-reciprocal strategy at low Reynolds number (Purcell (1977)). These natural swimmers have been modeled by artificial swimmers (joint micro-beads)

actuated by an oscillating ambient electric or magnetic field which opens breakthrough technologies for drug on-demand delivery in the human body (Dreyfus et al. (2005)).

Many numerical methods have been proposed to tackle the elasto-hydrodynamic coupling between a fluid flow and deformable objects, i.e. the balance between viscous drag and elastic stresses. Among those, “mesh-oriented” approaches have the ambition of solving a complete continuum mechanics description of the fluid/solid interaction, even though some approximations are mandatory to describe those at the fluid/solid interface. Without being all-comprehensive, one can cite immerse boundary methods (Fogelson and Peskin (1988); Stockie and Green (1998); Zhu and Peskin (2002, 2007)), extended finite elements (Wagner et al. (2001)), penalty methods (Glowinski et al. (1998); Decoene et al. (2011)), force-coupling Method (FCM) (Majmudar et al. (2012)). The method of regularized stokeslets has also been successfully adapted to locomotion problems (O’Malley and Bees (2012); Rodenborn et al. (2013)) and fluid-structure interactions (Olson et al. (2013); Simons et al. (2014)).

In the specific context of low Reynolds number *elastohydrodynamics* (Wiggins and Goldstein (1998)), difficulties arise when numerically solving the dynamics of rigid objects since the time scale associated with elastic waves propagation within the solid can be similar to the viscous dissipation time-scale. In the context of self-propelled objects the ratio of these time scales is called “Sperm number”. When the Sperm number is smaller or equal to one, the object temporal response is stiff, and requires small time steps to capture fast deformation modes. In this regime, fluid/structure interaction effects are difficult to capture. One possible way to circumvent such difficulties is to use the knowledge of hydrodynamic interactions of simple objects in Stokes flow.

This strategy is the one pursued by the bead model (BM) whose aim is to describe a complex deformable object by the flexible assembly of simple rigid ones. Such flexible assemblies are generally composed of beads (spheres or ellipsoids) interacting by some elastic and repulsive forces, as well as with the surrounding fluid. For long elongated structures, alternative approaches to BM are indeed possible such as slender body theory (Tornberg and Shelley (2004)) or resistive force theory (Lauga (2007); Coq et al. (2009); Gadêlha et al. (2010)).

One important advantage of BM which might explain their use among various communities (polymer physics (Gao et al. (2012); Jendrejack et al. (2002); Montesi et al. (2005); Yamanoi and Maia (2011)), micro-swimmer modeling in Biofluidmechanics (Swan et al. (2011); Bilbao et al. (2013); Gauger and Stark (2006); Majmudar et al. (2012)), flexible fiber in chemical engineering (Lindström and Uesaka (2007); Ross and Klingenberg (1997); Slowicka et al. (2012); Wang et al. (2012))), relies on their parametric versatility, their ubiquitous character and their relative easy implementation. Another major strength of BM is that it can model non-linear elastic regimes for a reduced cost and no additional complexity, whereas methods like resistive force theory and slender body theory require solving nonlinear stiff equations with special care. We provide a deeper, comparative and critical discussion about BM in Section 2.2. However, we would like to stress that the presented model is clearly oriented toward micro-swimmer modeling rather than polymer dynamics.

One should also add that BM can be coupled to mesh-oriented approaches in order

to provide accurate description of hydrodynamic interactions among large collection of deformable objects at moderate numerical cost (Majmudar et al. (2012)). Many authors only consider *free drain*, i.e. no hydrodynamic interactions (no HI), (Yamamoto and Matsuoka (1993); Skjetne et al. (1997); Ross and Klingenberg (1997); Schmid et al. (2000)) or far field interactions associated with the Rotne-Prager-Yamakawa tensor (Gauger and Stark (2006); Manghi et al. (2006); Wada and Netz (2006); Wajnryb et al. (2013)). This is supported by the fact that far-field hydrodynamic interactions already provide accurate predictions for the dynamics of a single flexible fiber when compared to experimental observations or numerical results. In order to illustrate our method, we use, for convenience, the Rotne-Prager-Yamakawa tensor to model hydrodynamic interactions. We wish to stress here that this is not a limitation of the presented method, since our formulation holds for any mobility matrix. However, it turns out that for each configuration we tested, our model gave very good comparisons with other predictions, including those providing more accurate description of the hydrodynamic interactions.

The chapter is organized as follows. First, we give a detailed presentation of the bead model for the simulation of flexible fibers. In this section, we propose a general formulation of kinematic constraints using the framework of Lagrange multipliers. This general formulation is used to present a new bead model, namely the gears model which surpasses existing models on numerical aspects. The second part of the chapter is devoted to comparisons and validations of bead models for different configurations of flexible fibers (experiencing a flow or actuated filaments).

Finally, we conclude the chapter by summarizing the achievements we obtain with our model and open new perspectives to this work.

2.2 The bead model

2.2.1 Detailed review of previous bead models

The bead model (BM) aims at discretizing any flexible object with interacting beads. Interactions between beads break down into three categories: hydrodynamic interactions, elastic and kinematic constraint forces. Hydrodynamics of the whole object result from multibody hydrodynamic interactions between beads. In the context of low Reynolds number, the relationship between stresses and velocities is linear. Thus, the velocity of the assembly depends linearly on the forces and torques applied on each of its elements. Elastic forces and torques are prescribed according to classical elasticity theory (Landau and Lifshitz (1975)) of flexible matter. Constraint forces ensure that the beads obey any imposed kinematic constraint, e.g. fixed distance between adjacent particles. All of these interactions can be treated separately as long as they are addressed in a consistent order. The latter is the cornerstone which differentiates previous works in the literature from ours. Numerous strategies have been employed to handle kinematic constraints.

Schlagberger and Netz (2005); Gauger and Stark (2006); Wada and Netz (2006); Yamanoi and Maia (2011)) and Slowicka et al. (2012) used a linear spring to model the resistance to stretching and compression without any constraint on the bead rotational

motion (Fig. 2.1). The resulting stretching force reads:

$$\mathbf{F}_s = -k_s(\mathbf{r}_{n,n+1} - \mathbf{r}_{n,n+1}^0) \quad (2.1)$$

where

- k_s is the spring stiffness,
- $\mathbf{r}_{n,n+1} = \mathbf{Y}^{n+1} - \mathbf{Y}^n$ is the distance vector between two adjacent beads (for simplicity, equations and figures will be presented for beads 1 and 2 and can easily be generalized to beads n and $n + 1$),
- \mathbf{Y}^n is the position of the center of mass of bead n ,
- $\mathbf{r}_{1,2}^0$ is the vector corresponding to equilibrium.

However, regarding the connectivity constraint, the spring model is somehow approximate. A linear spring is prone to uncontrolled oscillations and the problem may become unstable. Many other authors, among which [Jendrejck et al. \(2000, 2002\)](#); [Schroeder et al. \(2004\)](#), thus use non-linear spring models for a better description of polymer physics. Nevertheless, the repulsive force stiffness has an important numerical cost in time-stepping as will be discussed in section 2.2.6. Furthermore, unconstrained bead rotational motion leads to spurious hydrodynamic interactions and thus limits the range of applications for these BM.

Alternatively, [Skjetne et al. \(1997\)](#); [Ross and Klingenberg \(1997\)](#); [Schmid et al. \(2000\)](#); [Qi \(2006\)](#) and [Lindström and Uesaka \(2007\)](#) constrained the motion of the beads such that the contact point for each pair c_n remains the same. While more representative of a flexible object, this approach exhibits two main drawbacks:

1. a gap between beads is necessary to allow the object to bend (see Fig. 2.2),
2. it requires an additional center to center repulsive force, and thus more tuning numerical parameters to prevent overlapping between adjacent beads.

Consider two adjacent beads, with radius a , linked by a hinge c_1 (typically called ball and socket joint). The gap ε_g defines the distance between the sphere surfaces and the joint (see Fig. 2.3). Denote \mathbf{p}^n the vector attached to bead n pointing towards the next joint, i.e. the contact point c_n .

The connectivity between two contiguous bodies writes:

$$[\mathbf{Y}^1 + (a + \varepsilon_g)\mathbf{p}^1] - [\mathbf{Y}^2 - (a + \varepsilon_g)\mathbf{p}^2] = \mathbf{0} \quad (2.2)$$

and its time derivative

$$[\mathbf{V}^1 - (a + \varepsilon_g)\mathbf{p}^1 \times \boldsymbol{\Omega}^1] - [\mathbf{V}^2 + (a + \varepsilon_g)\mathbf{p}^2 \times \boldsymbol{\Omega}^2] = \mathbf{0}. \quad (2.3)$$

\mathbf{V}^n and $\boldsymbol{\Omega}^n$ are the translational and rotational velocities of bead n . The constraint forces and torques associated to Eq. (2.3) are obtained either by solving a linear system

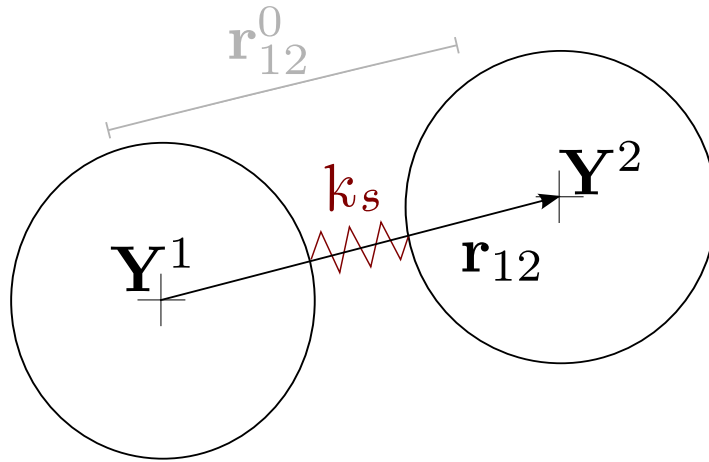


Figure 2.1: The spring model uses a linear spring with stiffness k_s to keep constant the inter-particle distance.

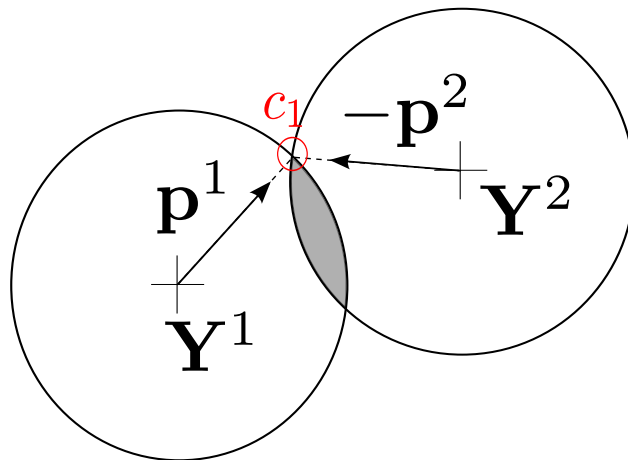


Figure 2.2: joint model: if there is no gap between adjacent beads, particles overlap when beading occurs. c_1 is the contact point between bead 1 and 2.

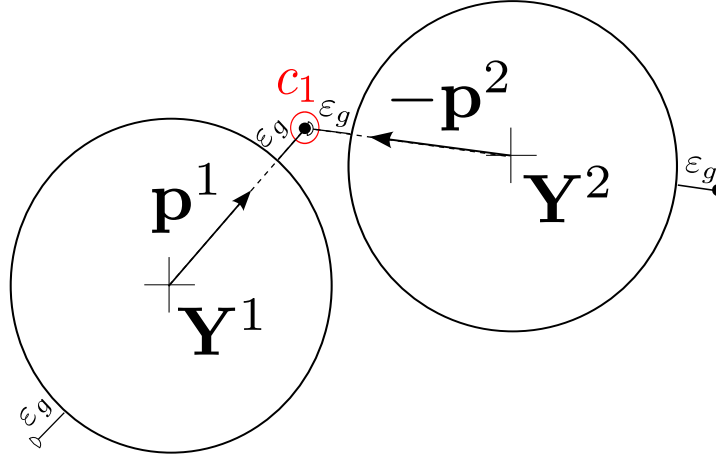


Figure 2.3: joint model: the contact point c_1 is separated by a gap ε_g from the bead surfaces to prevent overlapping in case of bending.

of equations involving beads velocities (Schmid et al. (2000)), or by inserting Eq. (2.3) into the equations of motion when neglecting hydrodynamic interactions (Skjetne et al. (1997); Ross and Klingenberg (1997)).

The gap width $2\varepsilon_g$ controls the maximum curvature κ_{\max}^J allowed without overlapping. From the sine rule, one can derive the simple equation relating ε_g and κ_{\max}^J

$$\kappa_{\max}^J = \frac{\sqrt{1 - \left(\frac{a}{a+\varepsilon_g}\right)^2}}{a} \quad (2.4)$$

Once aware of these limitations, the gap ε_g , range and strength of the repulsive force should be prescribed depending on the problem to be addressed.

Keaveny and Maxey (2008c) and Majmudar et al. (2012) proposed a more sophisticated joint model than those hitherto cited, using a full description of the links dynamics along the curvilinear abscissa. They derived a subtle constraint formulation which ensures that the tangent vector to the centerline is continuous and that the length of links remains constant. These two works are worth mentioning since they avoid an empirical tuning of repulsive forces. Yet, Keaveny and Maxey (2008c) computed the constraint forces and torques with an iterative penalty scheme instead of using an explicit formulation.

Finally, it is worth mentioning that the bead model proposed in Montesi et al. (2005) circumvents the inextensibility difficulty by imposing constraints on the relative velocities of each successive segments, so that their relative distance is kept constant. Using bending potential, Montesi et al. (2005) permit overlap between beads with restoring torque (cf. Fig. 2.2). A Lagrangian multiplier formulation of tensile forces is also used in Doyle et al. (1997), which is equivalent to a prescribed equal distance between successive beads. Again, inextensibility condition does not prevent bead overlapping due to bending in this formulation. The computation of contact forces which is proposed in the following section 2.2.2 generalizes the Lagrangian multiplier formulation of Montesi et al. (2005)

to generalized forces. Using more complex constraints involving both translational and angular velocities, we show that it is possible to accommodate both non-overlapping and inextensibility conditions without additional repulsive forces (using the rolling no-slip contact with the gears model detailed in 2.2.3). This proposed general formulation is also well suited for any type of kinematic boundary conditions as illustrated in Section 2.3.4.

2.2.2 Generalized forces, virtual work principle and Lagrange multipliers

The model and formalism proposed in this chapter rely on earlier work in Analytical Mechanics and Robotics (Nikravesh (2005); Joshi et al. (2010)). The concept of generalized coordinates and constraints which has proven to be very useful in these contexts is described here. Generalized coordinates refer to a set of parameters which uniquely describes the configuration of the system relative to some reference parameters (positions, angles,...). For describing objects of complex shape, let us consider the position \mathbf{Y}^n of each bead $n \in \{1, N_p\}$ with associated orientation vector \mathbf{p}^n which is defined by three Euler angles (θ, ϕ, ψ) . In the following, any collection of vector population $(\mathbf{Y}^1, ..\mathbf{Y}^n, ..\mathbf{Y}^{N_p}) \equiv \mathcal{Y}$ will be capitalized, so that \mathcal{Y} is a vector in \mathbb{R}^{3N_p} . Hence the collection of orientation vectors \mathbf{p}^n will be denoted \mathcal{P} , which is a vector of length $3N_p$, the collection of velocities \mathbf{V}^n , will be denoted \mathcal{V} , the collection of angular velocity $\mathbf{\Omega}^n$ will be \mathcal{W} , the collection of forces \mathbf{F}^n , \mathcal{F} , the collection of torques $\boldsymbol{\tau}^n$, \mathcal{T} . All \mathcal{V} , \mathcal{W} , \mathcal{F} and \mathcal{T} are vectors in \mathbb{R}^{3N_p} .

Let us then define some generalized coordinate \mathbf{q}^n for each bead, which is defined by $\mathbf{q}^n \equiv (\mathbf{Y}^n, \mathbf{p}^n)$ so that the collection of generalized positions $(\mathbf{q}^1, ..\mathbf{q}^n, ..\mathbf{q}^{N_p}) \equiv \mathcal{Q}$ is a vector in \mathbb{R}^{6N_p} . Generalized velocities are then defined by vectors $\dot{\mathbf{q}}^n \equiv (\mathbf{V}^n, \mathbf{\Omega}^n)$ with associated generalized collection of velocities $\dot{\mathcal{Q}}$.

Articulated systems are generically submitted to constraints which are either holonomic, non-holonomic or both (Bailey et al. (2008)). Holonomic constraints do not depend on any kinematic parameter (i.e any translational or angular velocity) whereas non-holonomic constraints do.

In the following we consider non-holonomic linear kinematic constraints associated with generalized velocities of the form (Greenwood (1997))

$$\mathcal{J}\dot{\mathcal{Q}} + \mathcal{B} = \mathbf{0}, \tag{2.5}$$

such that \mathcal{J} is a $N_c \times 6N_p$ matrix and \mathcal{B} is a vector of N_c components. N_c is the number of constraints acting on the N_p beads. \mathcal{B} and \mathcal{J} might depend (even non-linearly) on time t and generalized positions \mathcal{Q} , but do not depend on any velocity of vector $\dot{\mathcal{Q}}$, so that relation (2.5) is linear in $\dot{\mathcal{Q}}$. In subsequent sections, we provide specific examples for which this class of constraints are useful. Here we describe, following Greenwood (1997); Nikravesh (2005), how such constraints can be handled thanks to some generalized force that can be defined from Lagrange multipliers. The idea formulated to include constraints in the dynamics of articulated systems is to search additional forces which could permit to satisfy these constraints. First, one must rely on generalized forces $\mathbf{f}^n \equiv (\mathbf{F}^n, \boldsymbol{\tau}^n)$ which

include forces and torques acting on each bead, whose collection $(\mathbf{f}^1, \mathbf{f}^n, \dots, \mathbf{f}^{N_p})$ is denoted \mathfrak{F} . Generalized forces are defined such that the total work variation δW is the scalar product between them and the generalized coordinates variations $\delta \mathcal{Q}$

$$\delta W = \mathfrak{F} \cdot \delta \mathcal{Q} = \mathcal{F} \cdot \delta \mathcal{Y} + \mathcal{T} \cdot \delta \mathcal{P}, \quad (2.6)$$

so that, on the right hand side of (2.6) one also gets the translational and the rotational components of the work. Then, the idea of virtual work principle is to search some virtual displacement $\delta \mathcal{Q}$ that will generate no work, so that

$$\mathfrak{F} \cdot \delta \mathcal{Q} = 0. \quad (2.7)$$

At the same time, by rewriting Eq. (2.5) in differential form

$$\mathcal{J} d\mathcal{Q} + \mathcal{B} dt = \mathbf{0}, \quad (2.8)$$

admissible virtual displacements, i.e. those satisfying constraints (2.8), should satisfy

$$\mathcal{J} \delta \mathcal{Q} = \mathbf{0}. \quad (2.9)$$

Combining the N_c constraints (2.9) with (2.7) is possible using any linear combination of these constraints. Such linear combination involves N_c parameters, the so-called Lagrange multipliers which are the components of a vector $\boldsymbol{\lambda}$ in \mathbb{R}^{N_c} . Then from the difference between (2.7) and the N_c linear combination of (2.9) one gets

$$(\mathfrak{F} - \boldsymbol{\lambda} \mathcal{J}) \cdot \delta \mathcal{Q} = 0. \quad (2.10)$$

Prescribing an adequate constraint force

$$\mathfrak{F}_c = \boldsymbol{\lambda} \mathcal{J}, \quad (2.11)$$

permits to satisfy the required equality for any virtual displacement. Hence, the constraints can be handled by forcing the dynamics with additional forces, the amplitude of which are given by Lagrange multipliers, yet to be found. Note also, that this first result implies that both forces and torques associated with the N_c constraints are both associated with the same Lagrange multipliers.

This formalism is particularly suitable for low Reynolds number flows for which translational and angular velocities are linearly related to forces and torques acting on beads by the mobility matrix \mathcal{M}

$$\begin{pmatrix} \mathcal{V} \\ \mathcal{W} \end{pmatrix} = \mathcal{M} \begin{pmatrix} \mathcal{F} \\ \mathcal{T} \end{pmatrix} + \begin{pmatrix} \mathcal{V}_\infty \\ \mathcal{W}_\infty \end{pmatrix}. \quad (2.12)$$

$\mathcal{V}_\infty = (\mathbf{V}_\infty^1, \dots, \mathbf{V}_\infty^{N_p})$ and $\mathcal{W}_\infty = (\boldsymbol{\Omega}_\infty^1, \dots, \boldsymbol{\Omega}_\infty^{N_p})$ correspond to the ambient flow evaluated at the centers of mass \mathcal{Y} . Matrix \mathcal{M} can also be re-organized into a generalized mobility matrix \mathcal{M}^* in order to define the linear relation between the previously defined generalized velocity and generalized force

$$\dot{\mathcal{Q}} = \mathcal{M}^* \mathfrak{F} + \mathcal{V}_\infty^*, \quad (2.13)$$

where $\mathcal{V}_\infty^* = (\mathbf{V}_\infty^1, \boldsymbol{\Omega}_\infty^1, \dots, \mathbf{V}_\infty^{N_p}, \boldsymbol{\Omega}_\infty^{N_p})$. The explicit correspondence between the classical matrix \mathcal{M} and the hereby proposed generalized coordinate formulation \mathcal{M}^* is given in the Addendum 2.5. Hence, as opposed to the Euler-Lagrange formalism of classical mechanics, the dynamics of low Reynolds number flows does not involve any inertial contribution, and provide a simple linear relationship between forces and motion. In this framework, it is then easy to handle constraints with generalized forces, because the total external force will be the sum of the known elastic forces \mathfrak{F}_e , inner forces associated to active fibers \mathfrak{F}_a and the hereby discussed and yet unknown contact forces \mathfrak{F}_c to verify kinematic constraints

$$\mathfrak{F} = \mathfrak{F}' + \mathfrak{F}_c, \quad \text{with} \quad (2.14)$$

$$\mathfrak{F}' = \mathfrak{F}_e + \mathfrak{F}_a. \quad (2.15)$$

Hence, if one is able to compute the Lagrange multipliers $\boldsymbol{\lambda}$, the contact forces will provide the total force by linear superposition (2.14), which gives the generalized velocities with (2.13). Now, let us show how to compute the Lagrange multiplier vector. Since the generalized force is decomposed into known forces \mathfrak{F}' and unknown contact forces $\mathfrak{F}_c = \boldsymbol{\lambda}\mathcal{J}$, relations (2.14) and (2.13) can be pooled together yielding

$$\mathcal{M}^*\mathfrak{F}_c = \mathcal{M}^*\boldsymbol{\lambda}\mathcal{J} = \dot{\mathcal{Q}} - \mathcal{M}^*\mathfrak{F}' - \mathcal{V}_\infty^*. \quad (2.16)$$

So that, using (2.5),

$$\mathcal{J}\mathcal{M}^*\mathcal{J}^T\boldsymbol{\lambda} = -\mathcal{B} - \mathcal{J}(\mathcal{M}^*\mathfrak{F}' + \mathcal{V}_\infty^*), \quad (2.17)$$

one gets a simple linear system to solve for finding $\boldsymbol{\lambda}$, where \mathcal{J}^T stands for the transposition of matrix \mathcal{J} .

2.2.3 The gears model

The Euler-Lagrange formalism can be readily applied to any type of non-holonomic constraint such as Eq. (2.3). In the following, we propose an alternative model based on no-slip condition between the beads: the gears model. This constraint, first introduced in a bead model (BM) by Yamamoto and Matsuoka (1993), conveniently avoid numerical tricks such as artificial gaps and repulsive forces.

However, Yamamoto and Matsuoka (1993) and Yamamoto and Matsuoka (1995) relied on to an iterative procedure to meet requirements. Here, we use the Euler-Lagrange formalism to handle the kinematic constraints associated to the gears model.

Considering two adjacent beads, denoted “1” and “2”, (Fig. 2.4), the velocity \mathbf{v}_{c_1} at the contact point must be the same for each sphere:

$$\mathbf{v}_{c_1}^1 - \mathbf{v}_{c_1}^2 = \mathbf{0}. \quad (2.18)$$

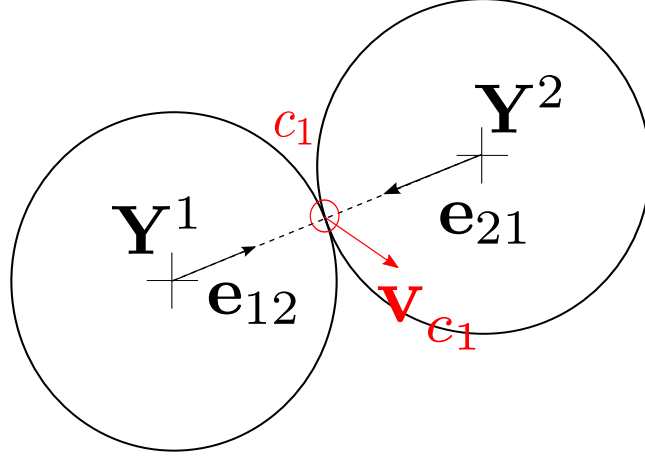


Figure 2.4: gears model: the velocity at the contact point c_1 must be the same for each bead (Eq. (2.18)).

$\mathbf{v}_{c_1}^1$ and $\mathbf{v}_{c_1}^2$ are respectively the rigid body velocity at the contact point between bead 1 and bead 2.

Denote $\boldsymbol{\sigma}^1$ the vectorial no-slip constraint. Eq. (2.18) becomes

$$\boldsymbol{\sigma}^1(\mathbf{V}^1, \boldsymbol{\Omega}^1, \mathbf{V}^2, \boldsymbol{\Omega}^2) = \mathbf{0}, \quad (2.19)$$

i.e.

$$[\mathbf{V}^1 - a\mathbf{e}_{12} \times \boldsymbol{\Omega}^1] - [\mathbf{V}^2 - a\mathbf{e}_{21} \times \boldsymbol{\Omega}^2] = \mathbf{0}, \quad (2.20)$$

where \mathbf{e}_{12} is the unit vector connecting the center of bead 1, located at \mathbf{Y}^1 , to the center of bead 2, located at \mathbf{Y}^2 ($\mathbf{e}_{12} = \mathbf{r}_{12}/\|\mathbf{r}_{12}\|$). The orientation vector \mathbf{p}^n attached to bead n , is not necessary to describe the system. Hence, from (2.20) one realizes that $\boldsymbol{\sigma}^1$ is linear in translational and rotational velocities. Therefore Eq. (2.19) can be reformulated as

$$\boldsymbol{\sigma}^1(\dot{\mathbf{Q}}) = \mathbf{J}^1 \dot{\mathbf{Q}} = \mathbf{0}. \quad (2.21)$$

where, $\dot{\mathbf{Q}}$ is the collection vector of generalized velocities of the two-bead assembly

$$\dot{\mathbf{Q}} = [\mathbf{V}^1, \boldsymbol{\Omega}^1, \mathbf{V}^2, \boldsymbol{\Omega}^2]^T, \quad (2.22)$$

\mathbf{J}^1 is the Jacobian matrix of $\boldsymbol{\sigma}^1$:

$$J_{kl}^1 = \frac{\partial \sigma_k^1}{\partial \dot{Q}_l}, \quad k = 1, \dots, 3, \quad l = 1, \dots, 12, \quad (2.23)$$

$$\begin{aligned} \mathbf{J}^1 &= [\mathbf{J}_1^1 \quad \mathbf{J}_2^1] \\ &= [\mathbf{I}_3 \quad -a\mathbf{e}_{12}^\times \quad -\mathbf{I}_3 \quad a\mathbf{e}_{21}^\times], \end{aligned} \quad (2.24)$$

and

$$\mathbf{e}^\times = \begin{pmatrix} 0 & -e_3 & e_2 \\ e_3 & 0 & -e_1 \\ -e_2 & e_1 & 0 \end{pmatrix}. \quad (2.25)$$

For an assembly of N_p beads, $N_p - 1$ no-slip vectorial constraints must be satisfied. The total Jacobian matrix \mathcal{J}^{GM} of the gears model (GM) is block bi-diagonal and reads

$$\mathcal{J}^{GM} = \begin{pmatrix} \mathbf{J}_1^1 & \mathbf{J}_2^1 & & & & \\ & \mathbf{J}_2^2 & \mathbf{J}_3^2 & & & \\ & & \ddots & \ddots & & \\ & & & \mathbf{J}_{N_p-1}^{N_p-1} & \mathbf{J}_{N_p}^{N_p-1} & \\ & & & & & \end{pmatrix} \quad (2.26)$$

where \mathbf{J}_β^α is the 3×6 Jacobian matrix of the vectorial constraint α for the bead β . The kinematic constraints for the whole assembly then read

$$\mathcal{J}^{GM} \dot{\mathbf{Q}} = \mathbf{0}. \quad (2.27)$$

The associated generalized forces \mathfrak{F}_c are obtained following Section 2.2.2.

2.2.4 Elastic forces and torques

We are considering *elastohydrodynamics* of homogeneous flexible and inextensible fibers. These objects experience bending torques and elastic forces to recover their equilibrium shape. Bending moments derivation and discretization are provided.

Bending moments

The bending moment of an elastic beam is provided by the constitutive law (Landau and Lifshitz (1975); Bishop et al. (2004))

$$\mathbf{m}(s) = K_b \mathbf{t} \times \frac{d\mathbf{t}}{ds}, \quad (2.28)$$

where $K_b(s)$ is the bending rigidity, \mathbf{t} is the tangent vector along the beam centerline and s is the curvilinear abscissa. Using the Frenet-Serret formula

$$\frac{d\mathbf{t}}{ds} = \kappa \mathbf{n}, \quad (2.29)$$

the bending moment writes

$$\mathbf{m}(s) = K_b \kappa \mathbf{b}, \quad (2.30)$$

where $\kappa(s)$ defines the local curvature, $\mathbf{n}(s)$ and $\mathbf{b}(s)$ are the normal and binormal vectors of the Frenet-Serret frame. When the link considered is not straight at rest, with an equilibrium curvature $\kappa^{eq}(s)$, Eq. (2.30) is modified into

$$\mathbf{m}(s) = K_b (\kappa - \kappa^{eq}) \mathbf{b}. \quad (2.31)$$

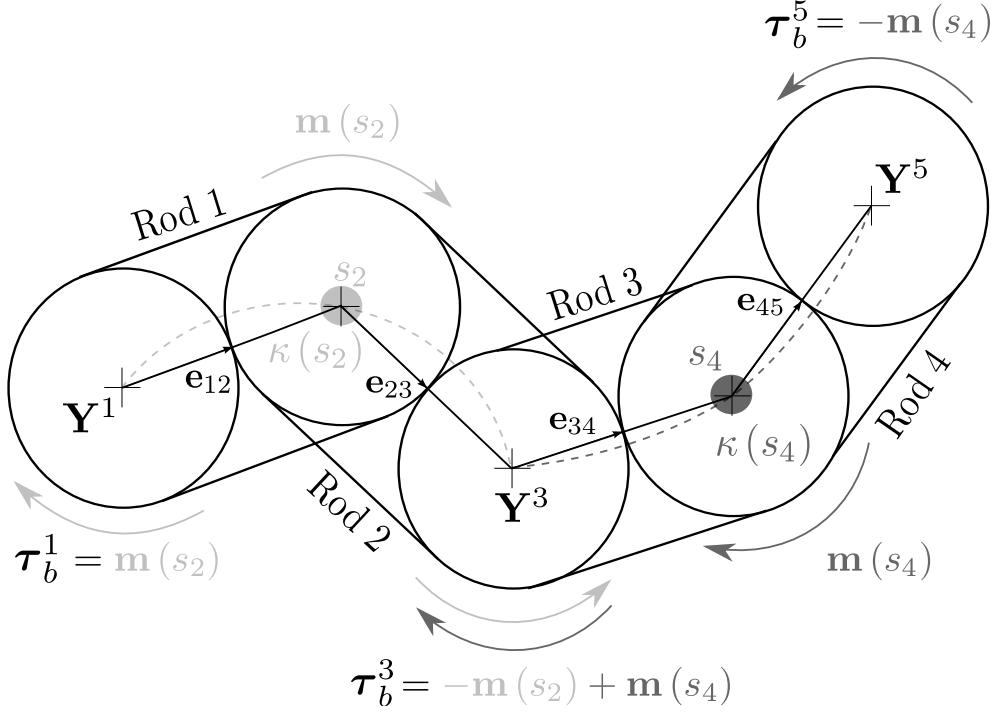


Figure 2.5: Beam discretization and bending torques computation of beads 1, 3 and 5. Remaining torques are accordingly obtained: $\tau_b^2 = \mathbf{m}(s_3)$ and $\tau_b^4 = -\mathbf{m}(s_3)$.

Here, the beam is discretized into $N_p - 1$ rigid rods of length $l = 2a$ (cf. Fig. 2.5). Inextensible rods are made up of two bonded beads and are linked together by a flexible joint with bending rigidity K_b . Bending moments are evaluated at joint locations $s_n = (n-1)l$ for $n = 2, \dots, N_p - 1$, where s_n correspond to the curvilinear abscissa of the center of mass bead n .

The bending torque on bead n is then given by

$$\tau_b^n = \mathbf{m}(s_{n+1}) - \mathbf{m}(s_{n-1}), \quad (2.32)$$

with $\mathbf{m}(s_n) = K_b \kappa(s_n) \mathbf{b}(s_n)$. See Fig. 2.5 for the torque computation on a beam discretized with four rods.

The local curvature $\kappa(s_n)$ is approximated using the sine rule (Lowe (2003))

$$\kappa(s_n) = \frac{1}{a} \sqrt{\frac{1 + \mathbf{e}_{n-1,n} \cdot \mathbf{e}_{n,n+1}}{2}} \quad (2.33)$$

where $\mathbf{e}_{n-1,n}$ is the unit vector connecting the center of mass of bead $n-1$ to the center of mass of bead n . This elementary geometric law provides the radius of curvature $R(s_n) = 1/\kappa(s_n)$ of the circle circumscribing neighboring bead centers \mathbf{Y}^{n-1} , \mathbf{Y}^n and \mathbf{Y}^{n+1} .

A more general version of the discrete curvature proposed in Fauci and Peskin (1988) can also be used in the case of three dimensional motion. In that case, the curvature of

the fiber is discretized as in [Fauci and Peskin \(1988\)](#)

$$\boldsymbol{\kappa}(s_n) = \frac{\mathbf{e}_{n-1,n} \times \mathbf{e}_{n,n+1}}{2a}, \quad (2.34)$$

where, again, $\mathbf{e}_{n-1,n}$ is the unit vector connecting the center of mass of bead $n - 1$ to the center of mass of bead n . The bending moment reads

$$\mathbf{m}(s_n) = K_b \boldsymbol{\kappa}(s_n). \quad (2.35)$$

To include the effect of torsional twisting about the axis of the fiber, one would have to compute the relative orientation between the frames of reference attached to the beads using Euler angles ([Keaveny and Maxey \(2008c\)](#)) (see Section 2.2.2) or unit quaternions as in [Schmid et al. \(2000\)](#). This would provide the rate of change of the twist angle along the fiber centerline and thus the twisting torque acting on each bead. In the following, only bending effects are considered.

2.2.5 Hydrodynamic coupling

Moving objects (rigid or flexible fibers) in a viscous fluid experience hydrodynamic forcing. The interactions are mediated by the fluid flow perturbations which can alter the motion and the deformation of the fibers in a moderately concentrated suspension. The existence of hydrodynamic interactions has also an effect on a single fiber dynamics while different parts of the fiber can respond to the ambient flow but also to local flow perturbations related to the fiber deformation. Resistive force theory (RFT) can be used to estimate the fiber response to a given flow assuming that the fiber is modeled by a large series of slender objects ([Coq et al. \(2010\)](#); [Lauga \(2007\)](#)). Slender body theory (SBT) has also been used ([Tornberg and Shelley \(2004\)](#); [Li et al. \(2013\)](#)) to relate local balance of drag forces with the filament forces upon the fluid resulting in a dynamical system to model the deformation of the fiber centerline. This model accounts for hydrodynamic interactions and provides interesting results on the stretch-coil transition of fibers in vortical flows ([Young and Shelley \(2007\)](#)).

In our beads model, the fiber is composed of spherical particles to account for the finite width of its cross-section. The hydrodynamic interactions are provided through the solution of the mobility problem which relates forces, torques to the translational and rotational velocities of the beads. This many-body problem is non-linear in the instantaneous positions of all particles of the system. Approximate solutions of this complex mathematical problem can be achieved by limiting the mobility matrices to their leading order. The simplest model is called free drain as the mobility matrix is assumed to be diagonal neglecting the HI with neighboring spheres. Pairwise interactions are required to account for anisotropic drag effects within the beads composing the fiber. The Rotne-Prager-Yamakawa (RPY) approximation is one of the most commonly used methods of including hydrodynamic interactions. This widely used approach has been recently updated by [Wajnryb et al. \(2013\)](#) for the RPY translational and rotational degrees of freedom.

2.2.6 Numerical implementation

Integration scheme and algorithm

The kinematics of the constrained system results from the superposition of individual bead motions. Positions are obtained from the temporal integration of the equation of motion with a third order Adams-Bashforth scheme

$$\frac{d\mathbf{Y}^n}{dt} = \mathbf{V}^n, \quad (2.36)$$

where \mathbf{Y}^n , \mathbf{V}^n are the position and translational velocity of bead n .

The time step Δt used to integrate Eq. (2.36) is fixed by the characteristic bending time (Lindström and Uesaka (2007))

$$\Delta t < \frac{\eta(2a)^4}{K_b}. \quad (2.37)$$

where η is the suspending fluid viscosity.

The evaluation of bead interactions must follow a specific order. Elastic and active forces can be computed in any order. Constraint forces and torques must be estimated afterwards as they depend on \mathfrak{F}' . Then velocities and rotations are obtained from the mobility relation. And finally, bead positions are updated.

- Initialization: positions \mathcal{Y}^0 ,
- Time loop on index k
 1. Evaluate mobility matrix $\mathcal{M}^*(Q^k)$ (see Section 2.2.5),
 2. Calculate local curvatures (Eq. (2.33)) and bending torques \mathcal{T}_b^k (Eq. (2.32)) to get \mathfrak{F}_e^k ,
 3. Add active forcing \mathfrak{F}_a^k and ambient velocity $\mathcal{V}_\infty^{k;*}$ if any,
 4. Compute the Jacobian matrix associated with non-holonomic constraints $\mathcal{J}^k = \mathcal{J}(Q^k)$,
 5. Solve Eq. (2.17) to get the constraint forces $\mathfrak{F}_c^k = \boldsymbol{\lambda}^k \mathcal{J}^k$,
 6. Sum all the forcing terms $\mathfrak{F}^k = \mathfrak{F}_e^k + \mathfrak{F}_a^k + \mathfrak{F}_c^k$,
 7. Apply mobility relation (Eq. (2.13)) to obtain the bead velocities \dot{Q}^k ,
 8. Integrate Eq. (2.36) to get the new bead positions \mathcal{Y}^{k+1} .

Implementation of the joint model

To provide a comprehensive comparison with previous works, we exploit the flexibility of the Euler-Lagrange formalism to implement the joint model, as described in Skjetne

et al. (1997), supplemented with hydrodynamic interactions. The joint constraint for two neighboring beads reads

$$[\mathbf{V}^n - (a + \varepsilon_g)\mathbf{p}^n \times \boldsymbol{\Omega}^n] - [\mathbf{V}^{n+1} + (a + \varepsilon_g)\mathbf{p}^{n+1} \times \boldsymbol{\Omega}^{n+1}] = \mathbf{0}. \quad (2.38)$$

Using the Euler-Lagrange formalism, Eq. (2.38) is reformulated with the joint model (JM) Jacobian matrix

$$\mathcal{J}^{JM} \dot{\mathbf{Q}} = \mathbf{0}, \quad (2.39)$$

where \mathcal{J}^{JM} has the same structure as in Eq. (2.26) and

$$\begin{aligned} \mathbf{J}^n &= \begin{bmatrix} \mathbf{J}_1^n & \mathbf{J}_2^n \end{bmatrix} \\ &= \begin{bmatrix} \mathbf{I}_3 & -(a + \varepsilon_g)\mathbf{p}_\times^n & -\mathbf{I}_3 & -(a + \varepsilon_g)\mathbf{p}_\times^{n+1} \end{bmatrix}. \end{aligned} \quad (2.40)$$

Accordingly, the corresponding set of forces and torques \mathfrak{F}_c are obtained from Section 2.2.2. As mentioned in Section 2.2.1, such formulation does not prevent beads from overlapping when bending occurs. A repulsive force \mathbf{F}_r is added according to Lindström and Uesaka (2007) (the force profile proposed by Skjetne et al. (1997) is very stiff, thus very constraining for the time step):

$$\mathbf{F}_r^{nm} = \begin{cases} -F_0 \exp\left(-\frac{d_{nm} + \delta_D}{d_0}\right) \mathbf{e}_{nm}, & d_{nm} \leq -\delta_D, \\ -F_0 \left(\frac{1}{2} - \frac{d_{nm}}{2\delta_D}\right) \mathbf{e}_{nm}, & -\delta_D < d_{nm} \leq \delta_D, \\ \mathbf{0}, & r_{nm} > \delta_D. \end{cases} \quad (2.41)$$

δ_D is an artificial surface roughness, d_{nm} is the surface to surface distance. $d_{nm} < 0$ indicates overlapping between beads n and m . d_0 is a numerical damping distance which has to be tuned to prevent overlapping. F_0 is the repulsive force scale chosen in order to avoid numerical instabilities. To deal with this issue, Lindström and Uesaka (2007) proposed to evaluate F_0 from bending and viscous stresses. A slight modification of their formula for inertialess particles yields

$$F_0 = C_1 6\pi\eta L (\overline{\mathbf{V}^\infty} - \overline{\mathbf{V}}) + C_2 \sqrt{\frac{\overline{K_b} E_b}{L^3}}. \quad (2.42)$$

The bar denotes the average over the constitutive beads or joints and C_1 and C_2 are adjustable constants. E_b is the bending energy

$$E_b = \sum_{n=1}^{N_p-1} K_b (\kappa(s_n) - \kappa^{eq}(s_n))^2, \quad (2.43)$$

Bending moments are evaluated at the joint locations $s_n^J = (a + \varepsilon_g) + (n - 1) \times 2(a + \varepsilon_g)$, $n = 1, \dots, N_p - 1$. joint curvature is given by

$$\kappa(s_n^J) = \frac{2}{a + \varepsilon_g} \sqrt{\frac{1 + \mathbf{p}^n \cdot \mathbf{p}^{n+1}}{2}}, \quad (2.44)$$

Similarly to Eq. (2.32), the bending torque on bead n is

$$\boldsymbol{\tau}_b^n = \mathbf{m}(s_n^J) - \mathbf{m}(s_{n-1}^J). \quad (2.45)$$

bead orientation \mathbf{p}^n is integrated with a third order Adams-Bashforth scheme

$$\frac{d\mathbf{p}^n}{dt} = \boldsymbol{\Omega}^n \times \mathbf{p}^n. \quad (2.46)$$

The procedure is similar to the gears model. \mathbf{p}^n are initialized together with the positions. The repulsive force \mathbf{F}_r is added to \mathfrak{F}' and can be computed between step 1 and 5 of the aforementioned algorithm. Time integration of Eq. (2.46) is performed at step 8.

Constraints and numerical stability

At each time step, the error on kinematic constraints ϵ is evaluated, after application of the mobility relation (Eq. (2.13)), between step 7 and step 8:

$$\epsilon^{GM}(t) = \left\| \mathcal{J}^{GM} \dot{\mathbf{Q}} \right\|_2 = \left(\sum_{n=1}^{N_p-1} (\mathbf{v}_{c_n}^n - \mathbf{v}_{c_n}^{n+1})^2 \right)^{1/2} \quad (2.47)$$

for the gears model, and

$$\epsilon^{JM}(t) = \left\| \mathcal{J}^{JM} \dot{\mathbf{Q}} \right\|_2 \quad (2.48)$$

for the joint model.

To verify the robustness of both models and Lagrange formulation, a numerical study is carried out on a stiff configuration.

A fiber of aspect ratio $r_p = 10$ with bending ratio $BR = 0.01$ (see Section 2.3.2 for the definition) is initially aligned with a shear flow of magnitude $\dot{\gamma} = 5s^{-1}$. For this aspect ratio, $N_p = 10$ beads are used to model the fiber with the gears model.

The joint model involves additional items to be fixed. $N_p = 9$ spheres are separated by a gap width $2\varepsilon_g = 0.25a$. The repulsive force is activated when the surface to surface distance d_{nm} reaches the artificial surface roughness $\delta_D = 2(a + \varepsilon_g)/10$. The remaining coefficients are set to reduce numerical instabilities without affecting the physics of the

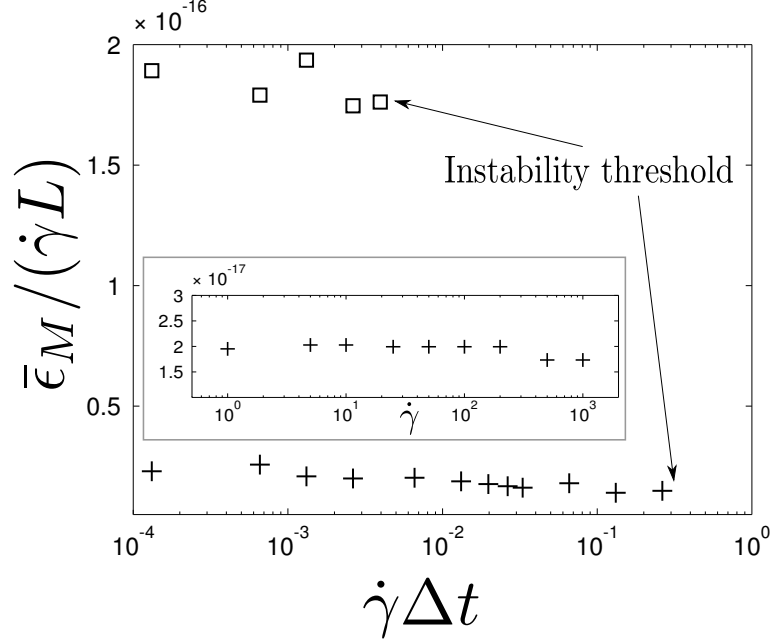


Figure 2.6: Dependence of the constraints $\bar{\epsilon}_M/\dot{\gamma}L$ on the time step $\dot{\gamma}\Delta t$, + : gears model, \square : joint model. Inset: $\bar{\epsilon}_M/\dot{\gamma}L$ with the gears model for a fixed time step given by Eq. (2.37) for different values of $\dot{\gamma}$.

system: $d_0 = (a + \varepsilon_g)/4$, $C_1 = 5$ and $C_2 = 0.5$.

Fig. 2.6 shows the evolution of the maximal mean deviation from the no-slip/joint constraint $\bar{\epsilon}_M = \max_t \epsilon(t)/(N_p - 1)$ normalized with the maximal shear velocity $\dot{\gamma}L$ depending on the dimensionless time step $\dot{\gamma}\Delta t$. First, one can observe that for both the joint and gears models, $\bar{\epsilon}_M/\dot{\gamma}L$ weakly depends on $\dot{\gamma}\Delta t$ and the resulting motion of the beads complies very precisely with the set of constraints, within a tolerance close to unit round-off ($< 2.10^{-16}$). Secondly, the joint model is unstable for time steps 100 times smaller than the gears model. The onset for numerical instability indicates that the repulsive force stiffness dominates over bending, thus dictating and restricting the time step.

As a comparison, Lindström and Uesaka (2007) matched connectivity constraints within 1% error for each fiber segment. To do so, they had to use an iterative scheme reducing the time step by 1/3 each iteration to meet requirements and limit overlapping between adjacent segments. For similar results, a stiff configuration, such as the sheared fiber, is therefore more efficiently simulated with the gears model.

Thirdly, inset of Fig. 2.6 shows that, for a given time step, the gears model constraints $\bar{\epsilon}_M/\dot{\gamma}L$ are satisfied whatever the shear magnitude. Hence, Eq. (2.37) ensures unconditionally numerical stability as bending is the only limiting effect for the gears model.

Hence, the robustness of the Euler-Lagrange formalism and the numerical integration we chose provide a strong support to the gears model over the joint model.

As a final remark to this section, it is important to mention that the numerical cost

of the proposed method strongly depends on the choice for the mobility matrix computation, as usual for bead models. If the mobility matrix is computed taking into account hydrodynamic interactions with Stokesian Dynamics, most of the numerical cost will come from its evaluation in this case. This limitation could be overcome using more sophisticated methods such as Accelerated Stokesian Dynamics (Sierou and Brady (2001)) or the force-coupling method (Yeo and Maxey (2010b)). When considering the Rotne-Prager-Yamakawa mobility matrix, its evaluation only requires the computation of $O((6N_p)^2)$ terms. Furthermore, the main algorithmic complexity of bead models does not come from the time integration of the bead positions which only requires a matrix-vector multiplication (Eq. (2.13)) at an $O((6N_p)^2)$ cost. Fast-multipole formulation of a Rotne-Prager-Yamakawa matrix can even provide an $O(6N_p)$ cost for such matrix-vector multiplication (Liang et al. (2013)).

The main numerical cost indeed comes from the inversion of the contact forces problem (Eq. (2.17)). It is worth noting that this linear problem is $N_c \times N_c$ which is slightly different from $N_p \times N_p$, but of the same order. Furthermore, Eq. (2.17) gives a direct, single step procedure to compute the contact forces, as opposed to previous other attempts (Yamamoto and Matsuoka (1993); Lindström and Uesaka (2007); Keaveny and Maxey (2008c)) which required iterative procedures to meet forces requirements, involving the mobility matrix inversion at each iteration. The cost for the inversion of Eq. (2.17) lies in-between $O(N_c^2)$ and $O(N_c^3)$ depending on the inversion method.

2.3 Validations

2.3.1 Jeffery orbits of rigid fibers

Much of our current understanding of the behavior of fibers experiencing a shear flow has come from the work of Jeffery (Jeffery (1922)) who derived the equation for the motion of an ellipsoidal particle in Stokes flow. The same equation can be used for the motion of an axisymmetric particle by using an equivalent ellipsoidal aspect ratio. Rigid fibers can be approximated by elongated prolate ellipsoids. An isolated fiber in simple shear flow rotates in a periodic orbit while the center of mass simply translates in the flow (no migration across streamlines). The period T (Eq. (2.49)) is a function of the aspect ratio of the fiber and the flow shear rate while the orbit depends on the initial orientation of the object relative to the shear plane

$$T = \frac{2\pi(r_e + 1/r_e)}{\dot{\gamma}}. \quad (2.49)$$

$\dot{\gamma}$ is the shear rate of the carrying flow. r_e is the equivalent ellipsoidal aspect ratio which is related to the fiber aspect ratio r_p (length of the fiber over diameter of the cross-section which turns out to $r_p = N_p$ with N_p beads). The fiber is initially placed in the plane of shear and is composed on N_p beads. No gaps between beads is required in the joint model because the fiber is rigid and flexibility deformations are negligible. We have

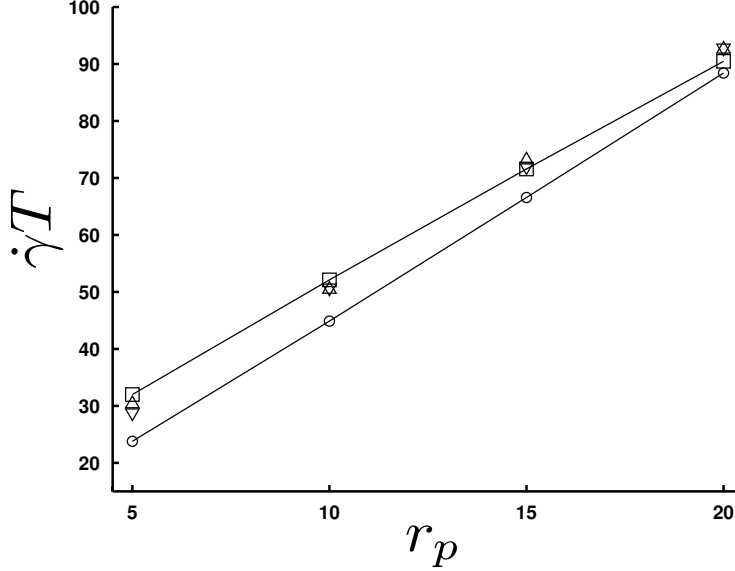


Figure 2.7: Tumbling period T depending on fiber aspect ratio r_p . \circ : theoretical law Eq. (2.49) with r_e given by Eq. (2.51), \square : theoretical law Eq. (2.49) with r_e given by Eq. (2.50), \triangle : gears model, ∇ : joint model.

compared the results with two relations for r_e : Cox (Cox (1971))

$$r_e = \frac{1.24r_p}{\sqrt{\ln(r_p)}}, \quad (2.50)$$

and Larson (Larson (1999))

$$r_e = 0.7r_p. \quad (2.51)$$

This classic and simple test case has been successfully validated in Yamamoto and Matsuoka (1993); Skjetne et al. (1997); Yamanoi and Maia (2011). Both the joint and gears models give a correct prediction of the period of Jeffery orbits (Fig. 2.7). The scaled period $\dot{\gamma}T$ of simulations remains within the two evolutions based on Eq. (2.50) and Eq. (2.51). We have tried to compare it with the linear spring model proposed by Gauger and Stark (Gauger and Stark (2006)) (and used by Slowicka et al. (Slowicka et al. (2012)) with a more detailed formulation of hydrodynamic interactions). In this latter model, there is no constraint on the rotation of beads and the simulations failed to reproduce Jeffery orbits (the fiber does not flip over the axis parallel to the flow).

2.3.2 Flexible fiber in a shear flow

The motion of flexible fibers in a shear flow is essential in paper making or composite processing. Prediction and control of fiber orientations and positions are of particular interest in the study of flocks disintegration. Many models have been designed to predict

fiber dynamics and much experimental work has been conducted. The wide variety of fiber behaviors depends on the ratio of bending stresses over shear stress, which is quantified by a dimensionless number, the bending ratio BR (Forgacs and Mason (1959a); Schmid et al. (2000))

$$\text{BR} = \frac{E(\ln 2r_e - 1.5)}{\eta\dot{\gamma}2r_p^4} \quad (2.52)$$

E is the material Young's Modulus and η is the suspending fluid viscosity. In the following, we investigate the response of the gears model with known results on flexible fiber dynamics.

Effect of permanent deformation

Forgacs and Mason (1959a,b) analyzed the motion of flexible threadlike particles in a shear flow depending on BR. They observed important drifts from the Jeffery orbits and classified them into categories. Yet, the goal of this section is not to carry out an in-depth study on these phenomena. Instead, the objective is to show that our model can reproduce basic features characteristic of sheared flexible filaments. We analyze first the influence of intrinsic deformation on the motion.

If a fiber is straight at rest, it will symmetrically deform in a shear flow. When aligned with the compressive axes of the ambient rate of strain \mathbf{E}^∞ , the fiber adopts the ‘‘S-shape’’ observed in Fig. 2.8a. When aligned with the extensional axes, tensile forces turn the rod back to its equilibrium shape. This symmetry is broken when the filament is initially slightly deformed or has a permanent deformation at rest, i.e. a nonzero equilibrium curvature $\kappa^{eq} > 0$. An initial small perturbation of the shape of a straight filament aligned with flow can induce large deformations during the orbit. This phenomenon is known as the buckling instability whose onset and growth are quantified with BR (Becker and Shelley (2001); Guglielmini et al. (2012)). Fig. 2.8b illustrates the evolution of a flexible sheared filament with $\text{BR} = 0.04$ and a very small intrinsic deformation $\kappa^{eq} = 1/(100L)$. The equilibrium dimensionless radius of curvature is $2R^{eq}/L = 200$. During the tumbling motion it decreases to a minimal value of $2R_{min}/L = 0.26$. Buckling thus increases by 770 times the maximal fiber curvature.

Maximal fiber curvature

Salinas and Pittman (1981) measured the radius of curvature R of sheared fiber for aspect ratios r_p ranging from 283 to 680. They reported on the evolution of the minimal value R_{min} , i.e. the maximal curvature κ_{max} , with BR. Schmid et al. (2000) used the joint model with prolate spheroids but no hydrodynamic interactions and compared their results with Salinas and Pittman (1981). Both experimental results from Salinas and Pittman (1981) and simulations from Schmid et al. (2000) are accurately reproduced by the gears model.

Hydrodynamic interactions between fiber elements play an important role in the bending of flexible filaments (Salinas and Pittman (1981); Lindström and Uesaka (2007); Slowicka et al. (2012)). As mentioned in Section 2.2.5 the use of spheres to build any arbitrary

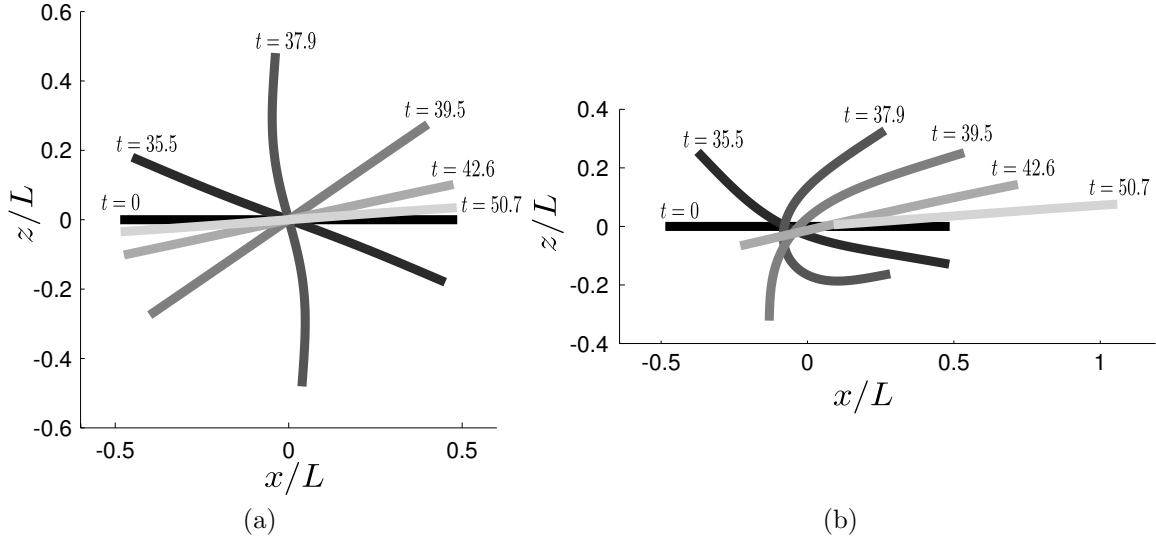


Figure 2.8: Orbit of a flexible filament in a shear flow with $BR = 0.04$. Temporal evolution is shown in the plane of shear flow. (a) Symmetric “S-shape” of a straight filament, $\kappa^{eq} = 0$. (b) Buckling of a permanently deformed rod with an intrinsic curvature $\kappa^{eq} = 1/(100L)$.

object is well suited to compute these hydrodynamic interactions. However, modeling rigid slender bodies in a strong shear flow becomes costly when increasing the fiber aspect ratio. First, the aspect ratio of a fiber made up of N_p spheres is $r_p = N_p$. Each time iteration requires the computation of \mathcal{M}^* and the inversion of a linear system (Eq. (2.17)) corresponding to N_c relations of constraints with $N_c \geq 3(N_p - 1)$. Secondly, for a given shear rate $\dot{\gamma}$ and bending ratio BR , Young’s modulus increases as r_p^4 . According to Eq. (2.37), the time step becomes very small for large Young’s modulus E . Schmid et al. (2000) partially avoided this issue by neglecting pairwise hydrodynamic interactions (\mathcal{M}^* is diagonal), and by assembling prolate spheroids of aspect ratios $r_e \sim 10$.

Yet, it is shown in Fig. 2.9a that for a fixed BR , $2R_{min}/L$ converges asymptotically to a constant value with r_p . An asymptotic regime (relative variation less than 2%) is reached for $r_p \geq 25$. Choosing $r_p = 35$ thus enables a valid comparison with previous results.

Our simulation results compare well with the literature data (Fig. 2.9b) and better match with to experiments than Schmid et al. (2000). When $BR \geq 0.04$, the gears model clearly underestimates measurements for $\kappa^{eq} = 1/(10L)$ and overestimates them for $\kappa^{eq} = 0$. However, Salinas and Pittman (Salinas and Pittman (1981)) indicated that the error quantification on parameters and measurements is difficult to estimate as the fibers were hand-drawn. Notably, drawing accuracy decreases for large radii of curvature, which leads to the conclusion that the hereby observed discrepancy might not be critical. They did not report the value of permanent deformation κ^{eq} for the fibers they designed, whereas, as evidenced by Forgacs and Mason (1959b), it has a strong impact on R_{min} . A numerical study of this dependence should be conducted to compare with Forgacs and

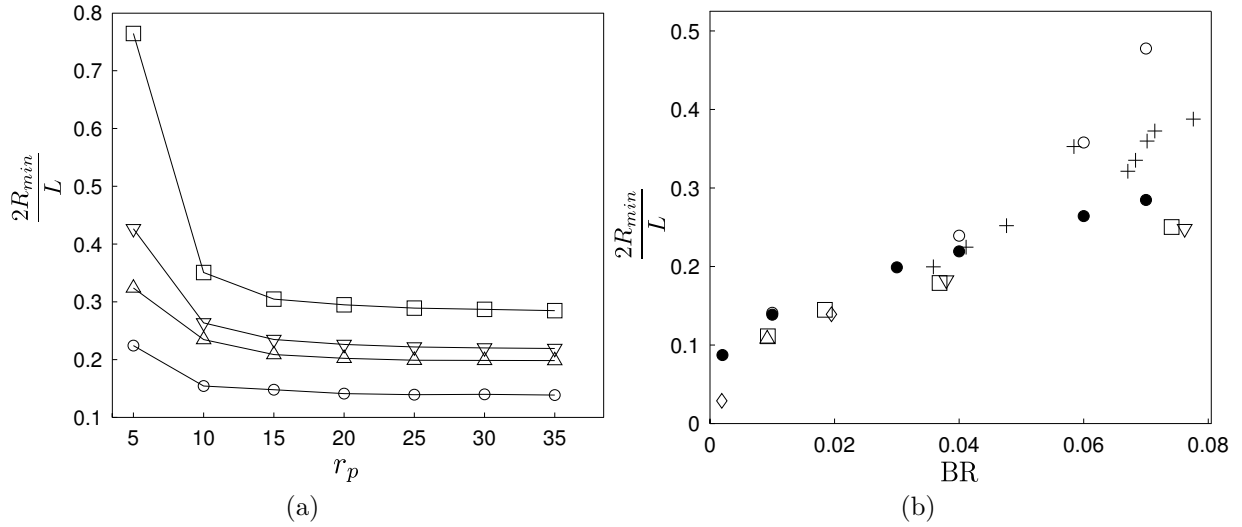


Figure 2.9: (a) Minimal radius of curvature depending on fiber length for several bending ratios. \square : BR = 0.01, \circ : BR = 0.03, ∇ : BR = 0.04, \triangle : BR = 0.07. (b) Minimal radius of curvature along BR. \circ : current simulations with aspect ratio $r_p = 35$ and intrinsic curvature $\kappa^{eq} = 0$; \bullet : current simulations with aspect ratio $r_p = 35$ and intrinsic curvature $\kappa^{eq} = 1/(10L)$; simulation results from Schmid et al. (2000) with $\kappa^{eq} = 1/(10L)$: (\diamond : $r_p = 50$, \triangle : $r_p = 100$, ∇ : $r_p = 150$, \square : $r_p = 280$); $+$: experimental measurements from Salinas and Pittman (1981), $r_p = 283$.

Mason (1959b), Fig. 7.

Lindström and Uesaka (2007) used the same approach as Schmid et al. (2000) with hydrodynamic interactions to repeat numerically the experiments from Salinas and Pittman (1981); but their results, though reliable, were displayed such that direct comparison with previous work is not possible.

To conclude, it should be noted that, in Schmid et al. (2000), the aspect ratio does not affect $2R_{min}/L$ for a fixed BR, confirming the asymptotic behavior observed in Fig. 2.9a.

2.3.3 Settling fiber

Consider a fiber settling under constant gravity force $\mathbf{F}_\perp = F_\perp \mathbf{e}_\perp$ acting perpendicularly to its major axis. The dynamics of the system depends on three competing effects: the elastic stresses which tend to return the object to its equilibrium shape, the gravitational acceleration which uniformly translates the object and the hydrodynamic interactions which creates local drag along the filament. After a transient regime, the filament reaches steady state and settles at a constant velocity with a fixed shape (see Figs. 2.10a and 2.10b). This steady state depends on the elasto-gravitational number

$$B = F_\perp L / K_b. \quad (2.53)$$

Cosentino Lagomarsino et al. (2005); Keaveny (2008) and Li et al. (2013) examined the contribution of each competing effect by measuring the normal deflection A , i.e. the distance between the uppermost and the lowermost point of the filament along the direction of the applied force (Fig. 2.10b) ; and the normal friction coefficient $\gamma_{\perp}/\gamma_{\perp}^0$ as a function of B . γ_{\perp}^0 is the normal friction coefficient of a rigid rod. To compute hydrodynamic interactions Cosentino Lagomarsino et al. (2005) used Stokeslet ; Keaveny (2008), the Force Coupling Method (FCM); Li et al. (2013), Slender Body Theory.

Similar simulations were carried out with both the joint model described in Section 2.2.6 and the gears model. Fiber of length $L = 68a$ is made out of $N_p = 31$ beads with gap width $2\varepsilon_g = 0.2a$ for the joint model and $N_p = 34$ for the gears model. To avoid both overlapping and numerical instabilities with the joint model, the following repulsive force coefficients were selected: $d_0 = (a + \varepsilon_g)/4$, $\delta_D = (a + \varepsilon_g)/5$, $C_1 = 0.01$ and $C_2 = 0.01$. No adjustable parameters are required for gears model.

Fig. 2.11 shows that our simulations agree remarkably well with previous results except slight differences with Li et al. (2013) in the linear regime $B < 100$. Using Slender Body Theory, Li et al. (2013) made the assumption of a spheroidal filament instead of a cylindrical one, with aspect ratio $r_p = 100$, i.e. three times larger than other simulations, whence such discrepancies. The normal friction coefficient (Fig. 2.11b), resulting from hydrodynamic interactions, perfectly matches the value obtained by Keaveny (2008) with the Force Coupling Method. The FCM is known to better describe multibody hydrodynamic interactions. Such a result thus supports the use of the simple Rotne-Prager-Yamakawa tensor for this hydrodynamic system.

The differences between the gears (GM) and joint model (JM) implemented here are quantified by measuring the relative discrepancies on the vertical deflection A

$$\epsilon_A = \frac{A_{GM} - A_{JM}}{A_{GM}}, \quad (2.54)$$

and on the normal friction coefficient $\gamma_{\perp}/\gamma_{\perp}^0$

$$\epsilon_{\gamma_{\perp}} = \frac{(\gamma_{\perp}/\gamma_{\perp}^0)_{GM} - (\gamma_{\perp}/\gamma_{\perp}^0)_{JM}}{(\gamma_{\perp}/\gamma_{\perp}^0)_{GM}}. \quad (2.55)$$

Discrepancies between joint and gears models remain below 5% except at the threshold of the non-linear regime ($B \approx 100$) where ϵ_A reaches 15% and $\epsilon_{\gamma_{\perp}} \approx 7.5\%$.

In accordance with Cosentino Lagomarsino et al. (2005), a metastable “W” shape is reached for $B > 3000$ (Fig. 2.10a) until it converges to the stable “horseshoe” state (Fig. 2.10b).

2.3.4 Actuated filament

The goal of the following sections is to show that the model we proposed is not only valid for passive objects but also for active ones. *Elastohydrodynamics* also concern swimming

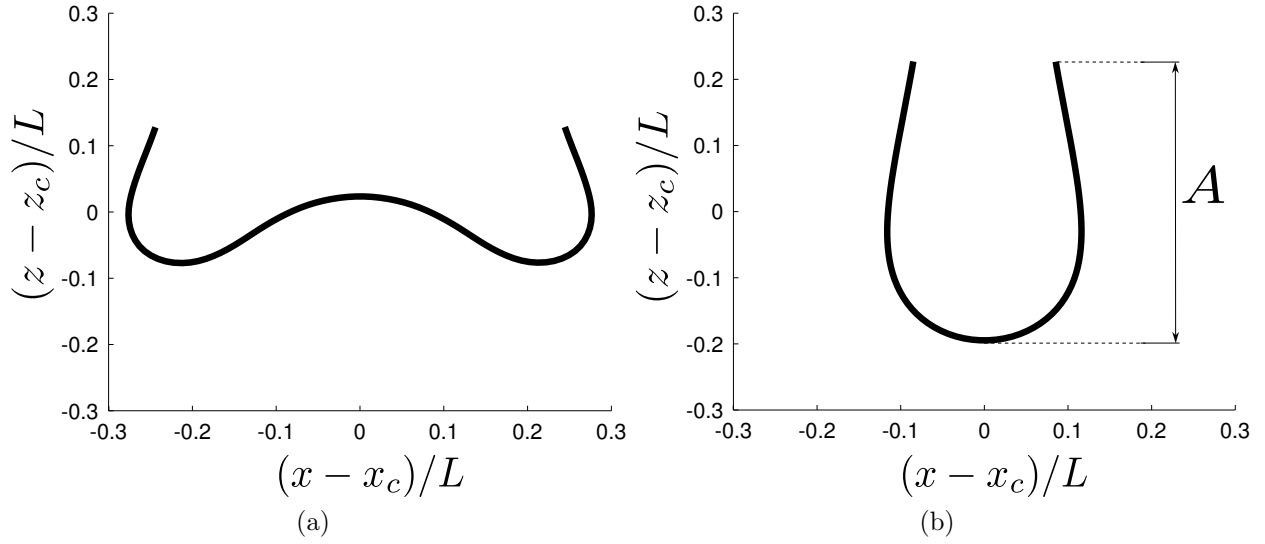


Figure 2.10: Shape of settling fiber for $B = 10000$ in the frame moving with the center of mass (x_c, z_c) . (a) Metastable “W” shape, $t = 12L/V_s$. (b) Steady “horseshoe” shape at $t = 53L/V_s$. V_s is the terminal settling velocity once steady state is reached.

at low Reynolds number (Purcell (1977)). Many type of micro-swimmers have been studied both from the experimental and theoretical point of view. Within that scope, the propagation of bending wave along passive elastic filament has been investigated by Wiggins et al. (1998), Yu et al. (2006) and Coq et al. (2008, 2009).

The experiment of Yu et al. (2006) consists in a flexible filament tethered and actuated at its base. The base angle was oscillated sinusoidally in a plane with an amplitude $\alpha_0 = 0.435\text{rad}$ and frequency ζ .

Deformations along the tail result from the competing effects of bending and drag forces acting on it. A dimensionless quantity called the Sperm number compares the contribution of viscous stresses to elastic response (Wiggins and Goldstein (1998))

$$\text{Sp} = L \left(\frac{\zeta (\gamma^\perp / L)}{K_b} \right)^{1/4} = \frac{L}{l_\zeta}. \quad (2.56)$$

γ^\perp is the normal friction coefficient. When using resistive force theory, (γ^\perp / L) is changed into a drag per unit length coefficient ξ^\perp . l_ζ can be seen as the length scale at which bending occurs. $\text{Sp} \lesssim 1$ corresponds to a regime at which bending dominates over viscous friction: the whole filament oscillates rigidly in a reversible and symmetrical way. $\text{Sp} \gg 1$ corresponds to a regime at which bending waves are immediately damped and the free end is motionless (Wiggins and Goldstein (1998)).

The experiment of Coq et al. (2008) is similar to Yu et al. (2006) except for that the actuation at the base is rotational. Here, the filament was rotated at a frequency ζ

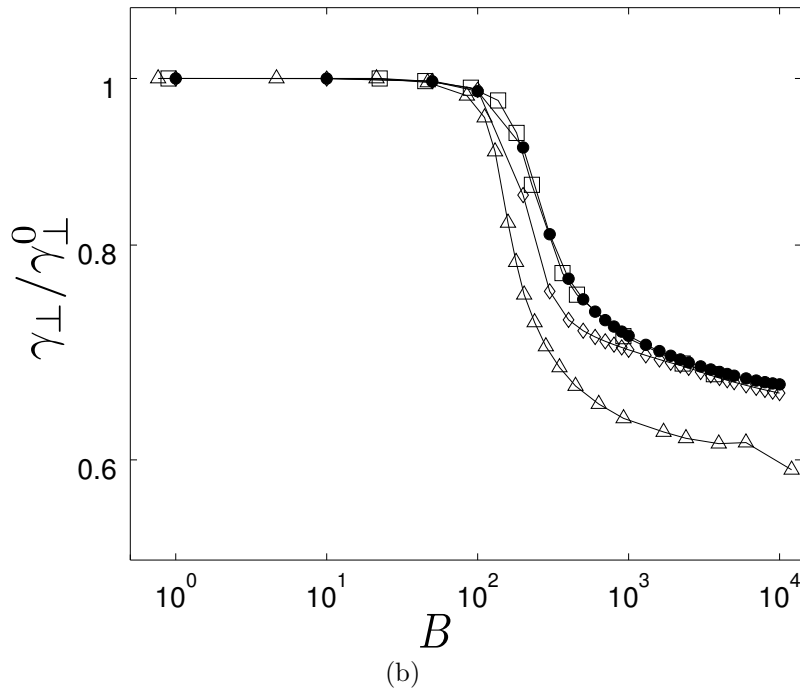
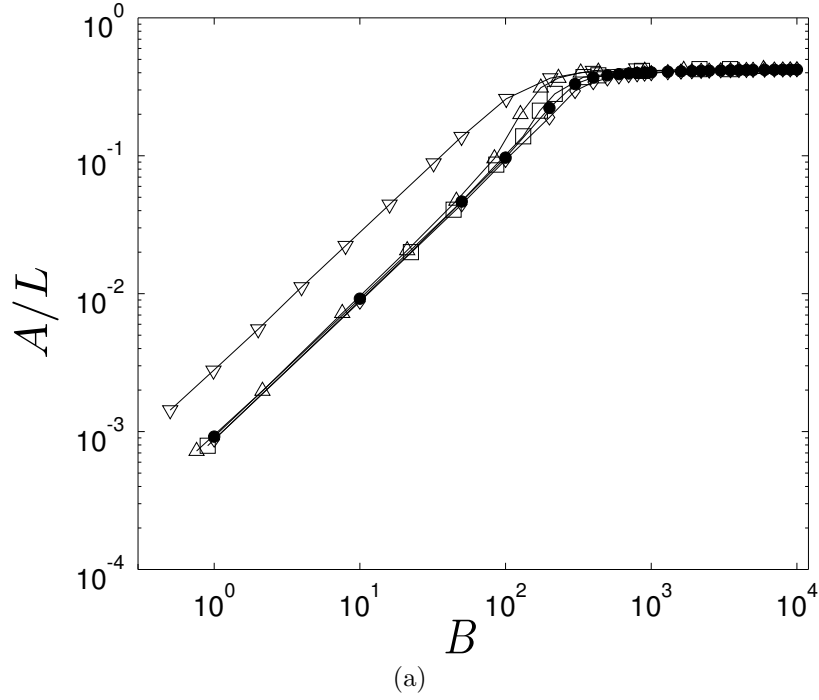


Figure 2.11: (a) Scaled vertical deflection A/L depending on the elasto-gravitational number B . \bullet : gears model, \diamond : joint model, \square : FCM results from [Keaveny \(2008\)](#), \triangle : Stokeslets results from [Cosentino Lagomarsino et al. \(2005\)](#), ∇ : Slender body theory results from [Li et al. \(2013\)](#). (b) Normal friction coefficient *vs.* B . \bullet : gears model, \diamond : joint model, \square : FCM results from [Keaveny \(2008\)](#), \triangle : Stokeslets results from [Cosentino Lagomarsino et al. \(2005\)](#).

forming a base angle $\alpha_0 = 0.262\text{rad}$ with the rotation axis.

In both contributions, the resulting fiber deformations were measured and compared to Resistive Force Theory for several values of Sp . Simulations of such experiments (Yu et al. (2006); Coq et al. (2008)) were performed with the gears model.

Numerical setup and boundary conditions at the tethered base element

Corresponding kinematic boundary conditions for BM are prescribed with the constraint formulation of the Euler-Lagrange formalism.

Planar actuation. In the case of planar actuation (Yu et al. (2006)), we consider that the tethered, i.e. the first, bead is placed at the origin and has no degree of freedom

$$\begin{cases} \mathbf{V}^1 = \mathbf{0}, \\ \boldsymbol{\Omega}^2 = \mathbf{0}. \end{cases} \quad (2.57)$$

Denote α_0 the angle formed between $\hat{\mathbf{x}}$ and $\mathbf{e}_{1,2}$. The trajectory of bead 2 must follow

$$\mathbf{Y}^2(t) = \begin{pmatrix} 2a \cos(\alpha_0 \sin(\zeta t)) \\ 0 \\ 2a \sin(\alpha_0 \sin(\zeta t)) \end{pmatrix}. \quad (2.58)$$

The constrained translational velocity of the second bead $\mathbf{V}^2(t)$ is thus obtained by taking the time derivative of Eq. (2.58)

$$\mathbf{V}^2(t) = \begin{pmatrix} -2a\alpha_0\zeta \cos(\zeta t) \sin(\alpha_0 \sin(\zeta t)) \\ 0 \\ 2a\alpha_0\zeta \cos(\zeta t) \cos(\alpha_0 \sin(\zeta t)) \end{pmatrix}. \quad (2.59)$$

The rotational velocity $\boldsymbol{\Omega}^2$ is constrained by the no-slip condition of the gears model.

Helical actuation. In the case of helical beating (Coq et al. (2008, 2009)), the anchor point of the filament is slightly off-centered with respect to the rotation axis $\hat{\mathbf{x}}$ (Coq et al. (2009): $r(0) = \delta_0$ (cf. Fig. 2.13, left inset). Coq et al. (2009) measured a value $\delta_0 = 2\text{mm}$ with a filament length varying from $L = 2\text{cm}$ to 10cm . Here we take $\delta_0 = \tilde{\delta}_0 \sin \alpha_0$ with $\tilde{\delta}_0 = 2.7a$ and vary the filament length by changing the number of beads N_p to match the experimental range $\delta_0/L = 0.1 \rightarrow 0.02$. The position of bead 1 must then follow

$$\mathbf{Y}^1(t) = \begin{pmatrix} \tilde{\delta}_0 \cos(\alpha_0 \sin(\zeta t)) \cos(\alpha_0 \cos(\zeta t)) \\ \tilde{\delta}_0 \cos(\alpha_0 \sin(\zeta t)) \sin(\alpha_0 \cos(\zeta t)) \\ \tilde{\delta}_0 \sin(\alpha_0 \sin(\zeta t)) \end{pmatrix}. \quad (2.60)$$

The constrained translational velocity of the first bead $\mathbf{V}^1(t)$ is thus obtained by taking the time derivative of Eq. (2.60)

$$\mathbf{V}^1(t) = \begin{pmatrix} \tilde{\delta}_0 \alpha_0 \zeta [-\cos(\zeta t) \sin(\alpha_0 \sin(\zeta t)) \cos(\alpha_0 \cos(\zeta t)) \\ + \sin(\zeta t) \sin(\alpha_0 \cos(\zeta t)) \cos(\alpha_0 \sin(\zeta t))] \\ \tilde{\delta}_0 \alpha_0 \zeta [-\cos(\zeta t) \sin(\alpha_0 \sin(\zeta t)) \sin(\alpha_0 \cos(\zeta t)) \\ - \sin(\zeta t) \cos(\alpha_0 \cos(\zeta t)) \cos(\alpha_0 \sin(\zeta t))] \\ \tilde{\delta}_0 \alpha_0 \zeta \cos(\zeta t) \cos(\alpha_0 \sin(\zeta t)) \end{pmatrix}. \quad (2.61)$$

And the rotational velocity is set to zero $\boldsymbol{\Omega}^1 = \mathbf{0}$.

The velocity of the second bead $\mathbf{V}^2(t)$ is prescribed in synchrony with bead 1:

$$\mathbf{V}^2(t) = \begin{pmatrix} (\tilde{\delta}_0 + 2a) \alpha_0 \zeta [-\cos(\zeta t) \sin(\alpha_0 \sin(\zeta t)) \cos(\alpha_0 \cos(\zeta t)) \\ + \sin(\zeta t) \sin(\alpha_0 \cos(\zeta t)) \cos(\alpha_0 \sin(\zeta t))] \\ (\tilde{\delta}_0 + 2a) \alpha_0 \zeta [-\cos(\zeta t) \sin(\alpha_0 \sin(\zeta t)) \sin(\alpha_0 \cos(\zeta t)) \\ - \sin(\zeta t) \cos(\alpha_0 \cos(\zeta t)) \cos(\alpha_0 \sin(\zeta t))] \\ (\tilde{\delta}_0 + 2a) \alpha_0 \zeta \cos(\zeta t) \cos(\alpha_0 \sin(\zeta t)) \end{pmatrix}. \quad (2.62)$$

The rotational velocity $\boldsymbol{\Omega}^2$ is constrained by the no-slip condition. The three-dimensional curvature $\boldsymbol{\kappa}$ is discretized with Eq. (2.34).

In both cases, imposing actuation at the base of the filament therefore requires the addition of three vectorial kinematic constraints, Eq. (2.57) and Eq. (2.59), to the no-slip conditions: $N_c = 3(N_p - 1) + 3 \times 3$. The additional Jacobian matrix \mathbf{J}^{act} writes

$$\mathbf{J}^{act} = \begin{pmatrix} \mathbf{I}_3 & \mathbf{0}_3 & \mathbf{0}_3 & \mathbf{0}_3 & \cdots & \mathbf{0}_3 & \mathbf{0}_3 \\ \mathbf{0}_3 & \mathbf{I}_3 & \mathbf{0}_3 & \mathbf{0}_3 & \cdots & \mathbf{0}_3 & \mathbf{0}_3 \\ \mathbf{0}_3 & \mathbf{0}_3 & \mathbf{I}_3 & \mathbf{0}_3 & \cdots & \mathbf{0}_3 & \mathbf{0}_3 \end{pmatrix}. \quad (2.63)$$

The corresponding right-hand side \mathbf{B}^{act} contains the imposed velocities

$$\mathbf{B}^{act} = \begin{pmatrix} \mathbf{0} \\ \mathbf{0} \\ -\mathbf{V}^2 \end{pmatrix} \quad (2.64)$$

for planar beating, and

$$\mathbf{B}^{act} = \begin{pmatrix} -\mathbf{V}^1 \\ \mathbf{0} \\ -\mathbf{V}^2 \end{pmatrix} \quad (2.65)$$

for helical beating.

\mathbf{J}^{act} and \mathbf{B}^{act} are simply appended to \mathcal{J} and \mathcal{B} respectively. The corresponding forces and torques \mathfrak{F}_c are computed as explained in Section 2.2.2.

Comparison with experiments and theory

The dynamics of the system can be described by balancing elastic stresses (flexion and tension) with viscous drag. Subsequent coupled non-linear equations can be linearized with the approximation of small deflections or solved with an adaptive integration scheme (Camalet and Jülicher (2000); Lauga (2007); Gadêlha et al. (2010)).

Planar actuation. Yu et al. (2006) considered both linear and non-linear theories and included the effect of a sidewall by using the corrected RFT coefficients of Mestre and Russel (1975).

Simulations are in good agreement with experiments, linear and non-linear theories for $Sp = 1.73, 2.2,$ and 3.11 (Fig. 2.12). Even though sidewall effects were neglected here, the gears model provides a good description of non-linear dynamics of an actuated filament in Stokes flow.

Helical actuation. Once steady state was reached, Coq et al. (2008) measured the distance of the tip of the rotated filament to the rotation axis $d = r(L)$ (cf. Fig. 2.13, left inset). Figure 2.13 compares their measures with our numerical results. Insets show the evolution of the filament shape with Sp . The agreement is quite good. Numerical simulations slightly overestimate d for $30 < Sp^4 < 90$. This may be due to the lack of information to reproduce experimental conditions and/or to measurement errors. As stated in Coq et al. (2009), taking the anchoring distance δ_0 into account is important to match the low Sperm number configurations where δ_0/L is non-negligible and the filament is stiff. If the anchoring point was aligned with the rotation axis ($\delta_0 = 0$), the distance to the axis of the rod free end would be $d/L = \sin \alpha_0 = 0.259$ for small Sp , as shown on Fig. 2.13.

2.3.5 Planar swimming nematode

Locomotion of the nematode *Caenorhabditis Elegans* is addressed here as its dynamics and modeling are well documented (Majmudar et al. (2012); Bilbao et al. (2013)). *C. Elegans* swims by propagating a contraction wave along its body length, from the fore to the aft (Fig. 2.14a). modeling such an active filament in the framework of BM just requires the addition of an oscillating driving torque $\boldsymbol{\tau}_D(s, t)$ to mimic the internal muscular contractions. To do so, Majmudar et al. (2012) used the preferred curvature model. In this model, the driving torque results from a deviation in the centerline curvature from

$$\kappa^D(s, t) = -\kappa_0^D(s) \sin(ks - 2\pi ft), \quad (2.66)$$

where $\kappa_0^D(s)$ is prescribed to reproduce higher curvature near the head:

$$\kappa_0^D(s) = \begin{cases} K_0, & s \leq 0.5L \\ 2K_0(L - s)/L, & s > 0.5L. \end{cases} \quad (2.67)$$

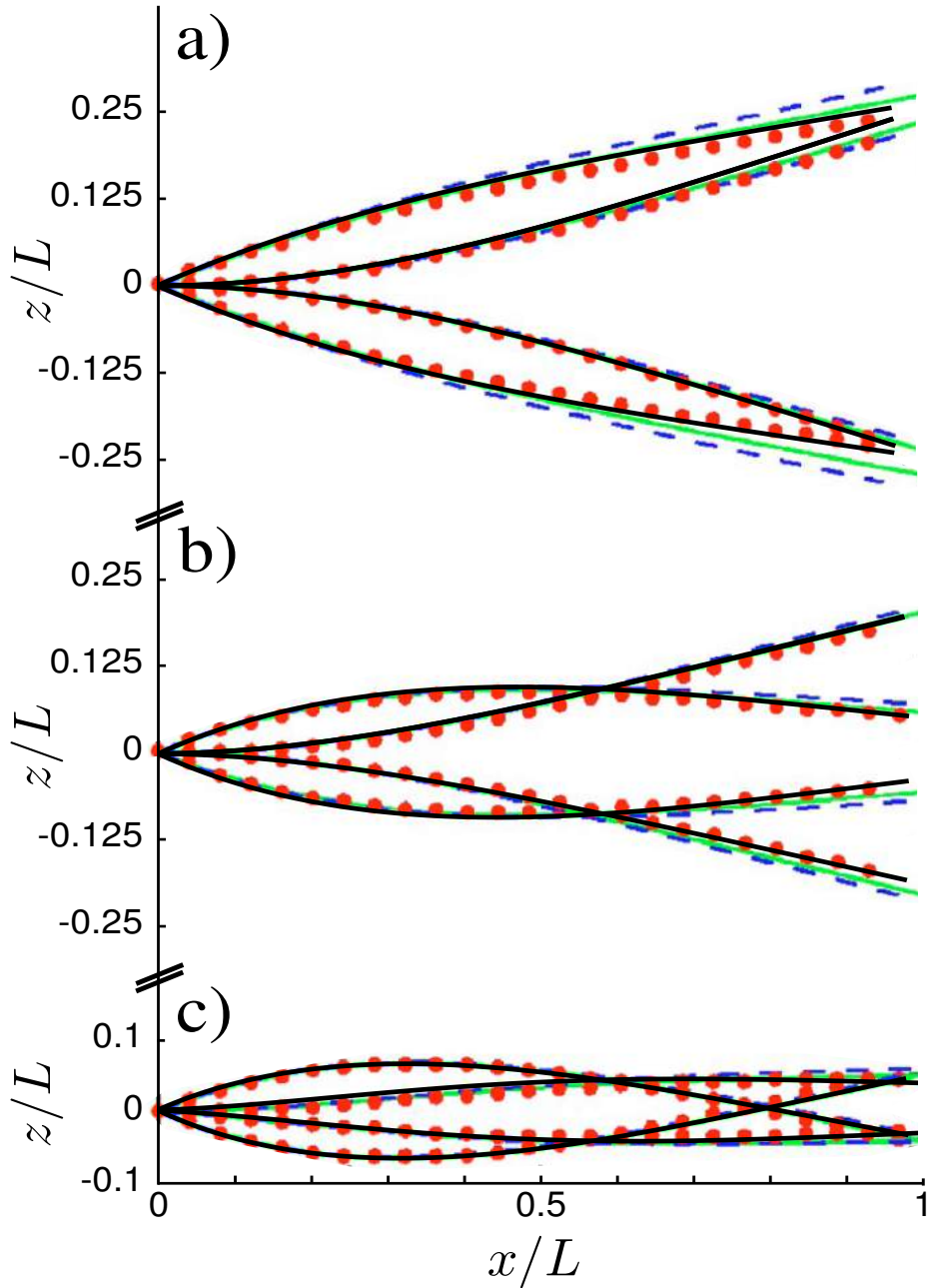


Figure 2.12: Comparison with experiments and numerical results from Yu et al. (2006). gears model results are superimposed on the original Fig. 3 of Yu et al. (2006). Snapshots are shown for four equally spaced intervals during the cycle for one tail with $\alpha_0 = 0.435\text{rad}$.
 • : experiment, — : linear theory, - - - : non-linear theory, — : gears model, a) $\zeta = 0.5 \text{ rad}\cdot\text{s}^{-1}$, $\text{Sp} = 1.73$. b) $\zeta = 1.31 \text{ rad}\cdot\text{s}^{-1}$, $\text{Sp} = 2.2$. c) $\zeta = 5.24 \text{ rad}\cdot\text{s}^{-1}$, $\text{Sp} = 3.11$.

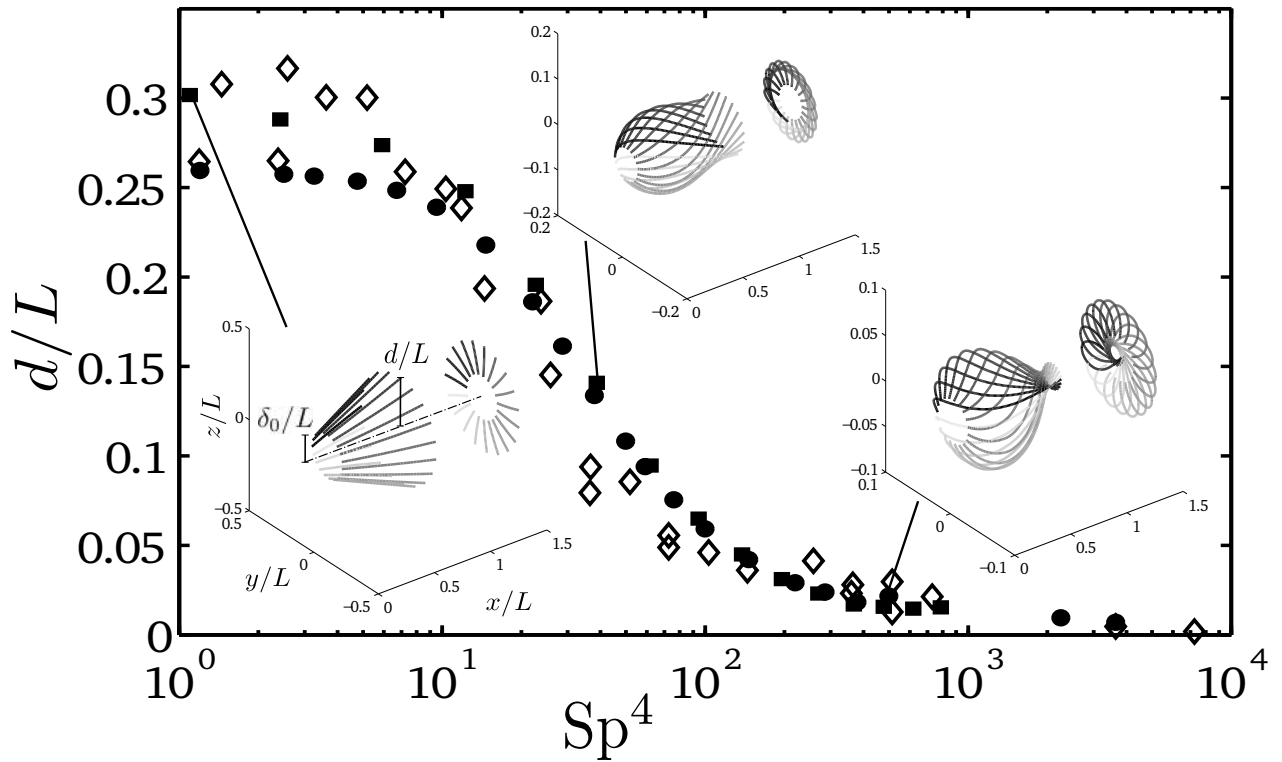


Figure 2.13: Comparison with experiments from [Coq et al. \(2008\)](#). (Insets) Evolution of the filament shape with Sp^4 . Snapshots are shown for twenty equally spaced intervals during one period at steady state. Gray level fades as time progresses. Left inset: δ_0/L is the distance of the tethered bead to the rotation axis, d/L is the distance of the free end to the rotation axis. (Main figure) Distance of the rod free end to the rotation axis normalized by the filament length d/L . \diamond : experiment, \bullet : gears model with no anchoring distance $\delta_0/L = 0$, \blacksquare : gears model with $\delta_0/L = 0.1 \rightarrow 0.02$ as in [Coq et al. \(2009\)](#).

The amplitude K_0 , wave number k and the associated Sperm number

$$\text{Sp} = L (f\eta/K_b)^{1/4} \quad (2.68)$$

were tuned to reproduce the measured curvature wave of the free-swimming nematode. They obtained the following set of numerical values: $K_0 = 8.25/L$, $k = 1.5\pi/L$ and $\text{Sp}^* = 22.6^{1/4}$. The quantity of interest to compare with experiments is the distance the nematode travels per stroke $V/(fL)$. K_b is assumed to be constant along s and is deduced from the other parameters. As for Eq. (2.32), the torque applied on bead n results from the difference in active bending moments across neighboring links

$$\tau_D^n(t) = \mathbf{m}^D(s_{n+1}, t) - \mathbf{m}^D(s_{n-1}, t), \quad (2.69)$$

with $\mathbf{m}^D(s_n, t) = K_b \kappa^D(s_n, t) \mathbf{b}(s_n)$. τ_D is added to \mathfrak{F}_a at step 3 of the algorithm in Section 2.2.6.

To match the aspect ratio of *C. Elegans*, $r_p = 16$, Majmudar et al. (2012) put $N_p = 15$ beads together separated by gaps of width $2\epsilon_g = 0.2a$. Here we assemble $N_p = 16$ beads, avoiding the use of gaps, and employ the same target-curvature wave and numerical coefficient values.

The net translational velocity $V^* = V/(fL) = 0.0662$ obtained with our model matches remarkably well with the numerical results $V/(fL) = 0.0664$ (Majmudar et al. (2012)) and experimental measurements $V/(fL) \approx 0.07$ (Bilbao et al. (2013)).

2.3.6 Cooperative swimming

One of the configurations explored in Llopis et al. (2013) has been chosen as a test case for the interactions between in-phase or out-of phase swimmers. Two identical, coplanar *C. Elegans* swim in the same direction with a phase difference $\Delta\phi$ which is introduced in the target curvature, and thus in the driving torque, of the second swimmer

$$\kappa^{D,2}(s, t) = -\kappa_0^D(s) \sin(ks - 2\pi ft + \Delta\phi). \quad (2.70)$$

The initial shape of the swimmers is taken from their steady state. We define d as the distance between their center of mass at initial time (see inset of Fig. 2.14b). Similarly to Llopis et al. (2013) Fig. 3, our results (Fig. 2.14b) show that antiphase beating enhance the propulsion, whereas in-phase swimming slows the system as swimmers get closer. Even though the model swimmer here is different, the quantitative agreement with Llopis et al. (2013) is strikingly good. Numerical work by Fauci (1990) also revealed that the average swimming speed of infinite sheets in finite Reynolds number flow is maximized when they beat in opposite phase. The conclusion that closer swimmers do not necessarily swim faster than individual ones has also been reported in Immler et al. (2007). They measured a decrease in the swimming speed of 25% for synchronized groups of house mouse sperm, as obtained on Fig. 2.14b for $d/L = 0.2$.

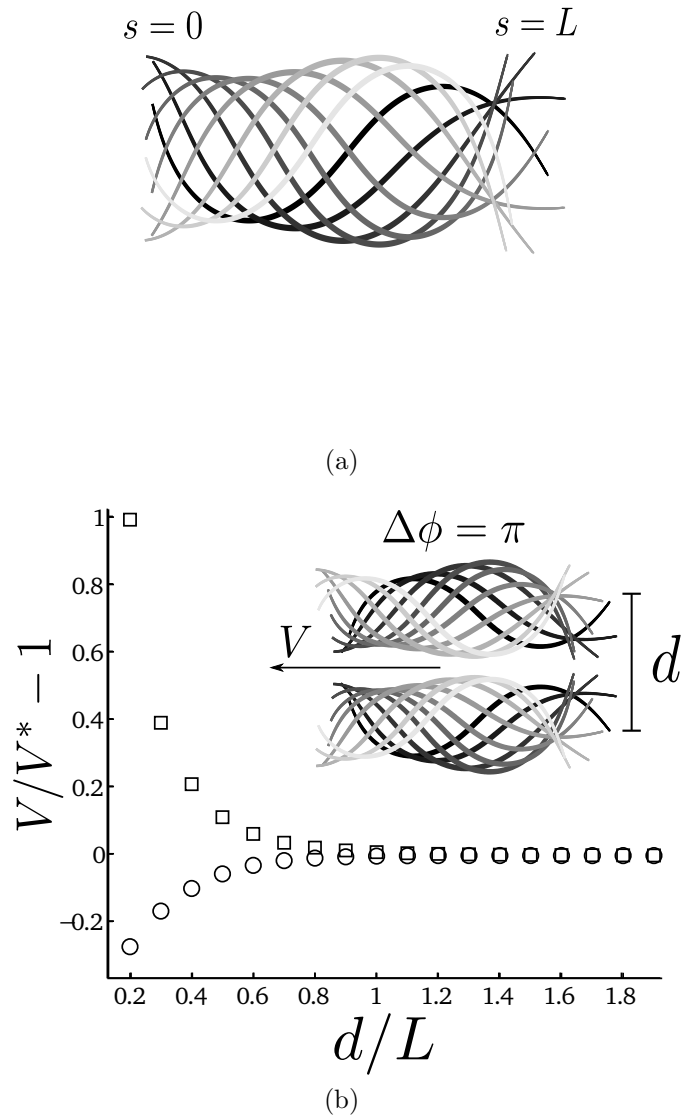


Figure 2.14: (a) Simulated wave motion of a swimming model *C. Elegans*. The nematode swims leftward and gray level fades as time progresses. Motion is shown in a frame moving with the micro-swimmer center of mass. (b) Inset: two *C. Elegans* beating in the same plane at a distance d in opposite phase ($\Delta\phi = \pi$). Nematodes swim leftward and gray level fades as time progresses. Main figure: Swimming speed of the center of mass of the system V normalized by the isolated swimming speed of *C. Elegans* V^* . \circ : in-phase motion ($\Delta\phi = 0$) ; \square : antiphase motion ($\Delta\phi = \pi$).

2.3.7 Spiral swimming

Many of the flagellate micro-organisms such as spermatozoa, bacteria or artificial micro-devices use spiral swimming to propel through viscous fluid. Propulsion with rotating rigid or flexible filaments has been thoroughly investigated in the past years (Cortez et al. (2005); Manghi et al. (2006); Qian et al. (2008); Keaveny and Maxey (2008c); Coq et al. (2009); Hsu and Dillon (2009); Keaveny et al. (2013)). In this section we illustrate the versatility of the proposed model by investigating the effect of the Sperm number and the eccentricity of the swimming gait on the swimming speed of *C. Elegans*.

Numerical configuration

The target curvature of *C. Elegans* κ^D remains unchanged except for that it is now directed along two components which are orthogonal to the helix axis. A phase difference $\Delta\phi = \pi/2$ is introduced between these two components. The resulting driving moment writes:

$$\mathbf{m}^D(s_n, t) = A_1 K_b \kappa^D(s_n, t) \mathbf{e}_\perp + A_2 K_b \kappa^D(s_n, t, \Delta\phi = \pi/2) \mathbf{e}_b. \quad (2.71)$$

$\{\mathbf{e}_\parallel, \mathbf{e}_\perp, \mathbf{e}_b\}$ are body fixed orthonormal vectors. \mathbf{e}_\parallel is directed along the axis of the helix, \mathbf{e}_\perp is a perpendicular vector and \mathbf{e}_b is the binormal vector completing the basis (Fig. 2.15 inset). The magnitude of the curvature wave along \mathbf{e}_\perp (resp. \mathbf{e}_b) is weighted by a coefficient A_1 (resp. A_2). The trajectory of a body element in the plane $\{\mathbf{e}_\perp, \mathbf{e}_b\}$ describes an ellipse whose eccentricity depends on the value of the ratio A_2/A_1 . When $A_2/A_1 = 0$ the driving torque is two-dimensional and identical to the one used in Section 2.3.5. When $A_2/A_1 = 1$ the magnitude of the driving torque is equal in both direction, the swimming gait describes a circle in the plane $\{\mathbf{e}_\perp, \mathbf{e}_b\}$ (see Fig. 2.15 inset). For the sake of simplicity, here we take $\{\mathbf{e}_\parallel, \mathbf{e}_\perp, \mathbf{e}_b\} = \{\hat{\mathbf{x}}, \hat{\mathbf{y}}, \hat{\mathbf{z}}\}$. As in 2.3.4, the curvature is evaluated with Eq. (2.34). In the following, $A_1 = 1$ and only A_2 is varied in the range $[0; 1]$.

Results

Figure 2.15 compares the planar swimming speed of *C. Elegans* V^* , with its “helical” version V , depending on the Sperm number defined in Section 2.3.5 Eq. (2.66) and on the ratio A_2/A_1 . The Sperm number Sp lies in the range $[17^{1/4}; 1000^{1/4}] = [2.03; 5.62]$. The lower bound is dictated by the stability of the helical swimming. When $\text{Sp} < 2.03$, the imposed curvature reaches a value such that the swimmer experiences a change in shape which is not helical. This sudden change in shape breaks any periodical motion and makes irrelevant the measurement of a net translational motion. Such limitation is only linked to the choice of the numerical coefficients of the target curvature model.

For the characteristic value $\text{Sp}^* = 22.6^{1/4}$ chosen by Majmudar et al. (2012), the purely helical motion provides a swimming speed four times faster than planar beating. Even though the model swimmer is different here, this result qualitatively agrees with those of Keaveny and Maxey (2008c) for which spiral swimming was faster than planar beating. Beyond a critical value $\text{Sp} \approx 2.6$, planar beating is faster. For $A_2/A_1 = 0.5$ the swimming speed is always smaller than for planar beating except when $\text{Sp} < 2.15$. This

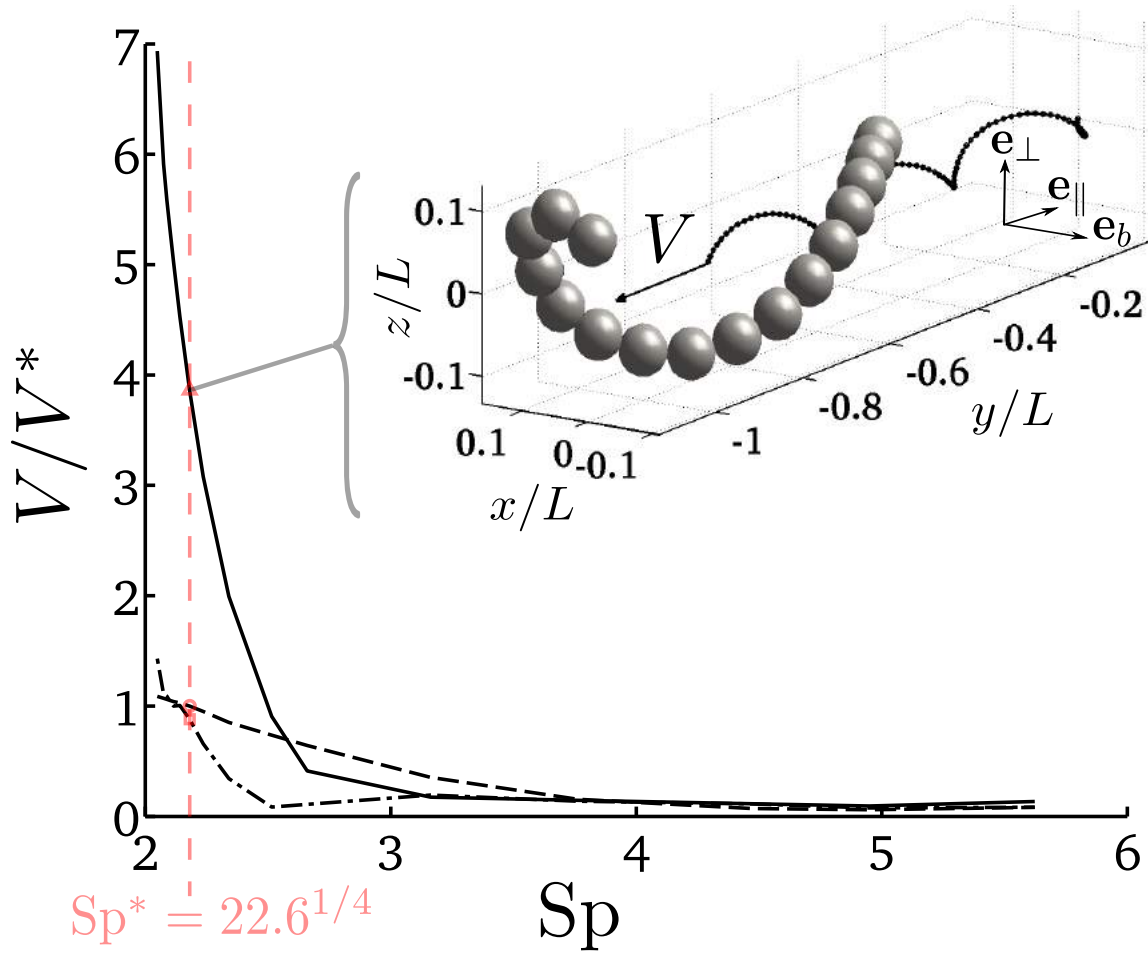


Figure 2.15: Helical swimming of *C. Elegans*. (Inset) Snapshot for $Sp^* = 22.6^{1/4}$ and $A_2/A_1 = 1$. \bullet : trajectory of the center of mass. (Main figure) Swimming speed of the center of mass V normalized by the planar swimming speed of *C. Elegans* V^* . — : $A_2/A_1 = 1$, - - - : $A_2/A_1 = 0.5$, - \cdot - \cdot : $A_2/A_1 = 0$ (planar motion),

last observation is not intuitive. A more extensive study on the effect of the eccentricity of the swimming gait on the swimming speed would be of interest.

2.4 Conclusions

We have provided a simple theoretical framework for kinematic constraints to be used in three-dimensional bead models (BM). This framework permits to handle versatile and complex kinematic constraints between flexible assembly of spheres, and/or more complex objects at low Reynolds numbers. Using Stokes linearity, this formulation requires, at each time step, the inversion of an $O(N_c \times N_c)$ linear system for an assembly having N_c constraints. Constraints are exactly matched (up to machine precision) and their evaluation is insensitive to the time-step. Furthermore, since the formulation explicitly handles mobility matrices, it can be used with any approximation for hydrodynamics interactions, from free drain (no HI) to Stokesian Dynamics. The proposed framework also implicitly incorporates the generic influence of external flows on kinematic constraints, as opposed to previous BM formulation which necessitates some adjustments to the ambient flow in most cases.

We also proposed a simple gears model to describe flexible objects, and we showed that such model successfully predicts the fiber dynamics in an external flow, its response to an external mechanical forcing and the motion of internally driven swimmers. Quantitative agreement with previous works is obtained for both slender objects (fibers, actuated filaments) and non-slender swimmers (*C. Elegans*), allowing its use in a wide variety of contexts. The gears model is easy to implement and it fulfills several important improvements over previous BM :

- There is no limitation on the fiber curvature, since the gears model does not need any repulsive force nor gap width to be defined.
- The gears model is more generic than previous ones, since there is no need for numerical parameter to be tuned.
- When compared with the joint model, the gears model is also much more stable by two orders of magnitude in time-step, a drastic improvement which offers nice prospects for the modeling of complex flexible assemblies.

Finally it should be noted that even if we only consider simple collections of spheres, any complex assembly can be easily treated within a similar framework, which provide interesting prospects in the future modeling of complex micro-organisms, membranes or cytoskeleton micro-mechanics.

2.5 Addendum: correspondence between \mathcal{M} and \mathcal{M}^*

The matrix \mathcal{M}^* defined in Eq. (2.13) results from the rearrangement of the well-known mobility matrix \mathcal{M} . This operation is necessary in order to combine the constraints (Eq.

(2.5)) and the mobility relation (Eq. (2.12)) to obtain the constraint forces \mathfrak{F}_c .

Matrix \mathcal{M} relates the collection of velocities $\mathcal{V} = (\mathbf{V}^1, \dots, \mathbf{V}^{N_p})$ and rotations $\mathcal{W} = (\boldsymbol{\Omega}^1, \dots, \boldsymbol{\Omega}^{N_p})$ to the collection of forces $\mathcal{F} = (\mathbf{F}^1, \dots, \mathbf{F}^{N_p})$ and torques $\mathcal{T} = (\boldsymbol{\tau}^1, \dots, \boldsymbol{\tau}^{N_p})$

$$\begin{pmatrix} \mathcal{V} \\ \mathcal{W} \end{pmatrix} = \begin{pmatrix} \mathcal{M}^{\mathcal{V}\mathcal{F}} & \mathcal{M}^{\mathcal{V}\mathcal{T}} \\ \mathcal{M}^{\mathcal{W}\mathcal{F}} & \mathcal{M}^{\mathcal{W}\mathcal{T}} \end{pmatrix} \begin{pmatrix} \mathcal{F} \\ \mathcal{T} \end{pmatrix}, \quad (2.72)$$

where $\mathcal{M}^{\mathcal{V}\mathcal{F}}$ is the $3N_p \times 3N_p$ matrix relating all the bead velocities to the forces applied to their center of mass

$$\mathcal{M}^{\mathcal{V}\mathcal{F}} = \begin{pmatrix} \mathbf{M}^{VF;11} & \dots & \mathbf{M}^{VF;1N_p} \\ \vdots & \ddots & \vdots \\ \mathbf{M}^{VF;N_p1} & \dots & \mathbf{M}^{VF;N_pN_p} \end{pmatrix}. \quad (2.73)$$

Eq. (2.72) is not consistent with the structure of the generalized velocities $\dot{\mathcal{Q}} = (\mathbf{V}^1, \boldsymbol{\Omega}^1, \dots, \mathbf{V}^{N_p}, \boldsymbol{\Omega}^{N_p})$ and forces $\mathfrak{F} = (\mathbf{F}^1, \boldsymbol{\tau}^1, \dots, \mathbf{F}^{N_p}, \boldsymbol{\tau}^{N_p})$ vectors. Thus we rearrange \mathcal{M} into \mathcal{M}^* such that

$$\mathcal{M}^{nm;*} = \begin{pmatrix} \mathbf{M}^{VF;nm} & \mathbf{M}^{VT;nm} \\ \mathbf{M}^{\Omega F;nm} & \mathbf{M}^{\Omega T;nm} \end{pmatrix}, \quad (2.74)$$

to obtain a mobility equation suited for the Euler-Lagrange formalism

$$\begin{pmatrix} \dot{\mathbf{q}}^1 \\ \vdots \\ \dot{\mathbf{q}}^{N_p} \end{pmatrix} = \begin{pmatrix} \mathcal{M}^{11;*} & \dots & \mathcal{M}^{1N_p;*} \\ \vdots & \ddots & \vdots \\ \mathcal{M}^{N_p1;*} & \dots & \mathcal{M}^{N_pN_p;*} \end{pmatrix} \begin{pmatrix} \mathfrak{f}^1 \\ \vdots \\ \mathfrak{f}^{N_p} \end{pmatrix}. \quad (2.75)$$

Which, in compact form, and in the absence of external flow, provides

$$\dot{\mathcal{Q}} = \mathcal{M}^* \mathfrak{F}. \quad (2.76)$$

Eq. (2.76) is strictly equivalent to Eq. (2.13).

Chapter 3

Biologically-relevant mesoscopic models.

Contents

3.1 Squirmers using the force-coupling method	58
3.1.1 FCM for an isolated passive particle	58
3.1.2 Squirmer model	59
3.1.3 Comparison with Blake’s solution	62
3.2 A time-dependent squirmer model based on experimental data	64
3.2.1 Time-dependent model for <i>Chlamydomonas reinhardtii</i>	64
3.2.2 Time-dependent model for the copepod <i>Arcatia tonsa</i> : preliminary investigations	66

In this chapter, we introduce an extension of the force-coupling method (FCM) (Maxey and Patel (2001); Lomholt and Maxey (2003)), an approach for the large-scale simulation of passive particles, to reproduce the disturbances generated by active particles. FCM relies on a regularized, rather than a singular, multipole expansion to account for the hydrodynamic interactions between the particles. We extend FCM to active particles by introducing the regularized singularities in the FCM multipole expansion that have a direct correspondence to the surface velocity modes of the squirmer model (Blake (1971)).

We explore in detail how to incorporate biologically-relevant, time-dependent swimming gaits by tuning our model to the recent measurements of the oscillatory flow around *Chlamydomonas reinhardtii* (Guasto et al. (2010)) and around a copepod at its naupliar stage (Wadhwa et al. (2014)). These experiments suggest that considering time-averaged flows for such micro-organisms may oversimplify the hydrodynamic interactions between neighbors. Time-dependency is also closely associated with the way zooplankton feed, mix the surrounding fluid, and interact with each other (Croze et al. (2013); Kiørboe et al. (2014)). As stated in Saintillan (2010b), modeling micro-swimmers with a time-dependent swimming gait might be more realistic and should be included in mathematical models and computer simulations.

3.1 Squirmers using the force-coupling method

The force-coupling method (FCM) developed by Maxey and collaborators (Maxey and Patel (2001); Lomholt and Maxey (2003)) is an effective approach for the large-scale simulation of particulate suspensions, especially for moderately concentrated suspensions at low Reynolds number. In this context, it has been used to address a variety of problems in micro-fluidics (Climent et al. (2004)), biofluid dynamics (Pivkin et al. (2006)), and micron-scale locomotion (Keaveny and Maxey (2008c,a); Majmudar et al. (2012)). FCM has also been extended to incorporate finite Reynolds number effects (Xu et al. (2002)), thermal fluctuations (Keaveny (2014)), near contact lubrication hydrodynamics (Dance and Maxey (2003); Yeo and Maxey (2010b)), and ellipsoidal particle shapes (Liu et al. (2009)). With these additional features, FCM has been used to address questions in fundamental fluid dynamics in regimes where inertial effects are important and/or there is a high volume fraction of particles (Yeo and Maxey (2010b,a)). At the same time, FCM has been used to address problems of technological importance, such as micro-bubble drag reduction (Xu et al. (2002)) and the dynamics of colloidal particles (Keaveny (2014)). In this section, we expand on Keaveny (2008) and develop the theoretical underpinnings of FCM's further extension to active particle suspensions using the squirmer model proposed by Lighthill (Lighthill (1952)), advanced by Blake (Blake (1971)), and employed by Ishikawa et al. (2006).

To begin this presentation, we give an overview of FCM for an isolated particle, establishing also the notation that will be used later on.

3.1.1 FCM for an isolated passive particle

Consider a rigid spherical particle, having radius a , in unbounded fluid at rest at infinity. The particle is centered at \mathbf{Y} and subject to force \mathbf{F} and torque $\boldsymbol{\tau}$. To determine its motion through the surrounding fluid, we first represent it by a low order, finite-force multipole expansion in the Stokes equations

$$\begin{aligned}\nabla p - \eta \nabla^2 \mathbf{u} &= \mathbf{F} \Delta(\mathbf{x}) + \frac{1}{2} \boldsymbol{\tau} \times \nabla \Theta(\mathbf{x}) \\ \nabla \cdot \mathbf{u} &= 0.\end{aligned}\tag{3.1}$$

In Eq. (3.1) are the two Gaussian envelopes,

$$\begin{aligned}\Delta(\mathbf{x}) &= (2\pi\sigma_\Delta^2)^{-3/2} e^{-|\mathbf{x}-\mathbf{Y}|^2/2\sigma_\Delta^2} \\ \Theta(\mathbf{x}) &= (2\pi\sigma_\Theta^2)^{-3/2} e^{-|\mathbf{x}-\mathbf{Y}|^2/2\sigma_\Theta^2},\end{aligned}\tag{3.2}$$

used to project the particle force and torque onto the fluid.

The flow solution of Eq. (3.1) is

$$\mathbf{u}^{FCM} = \mathbf{N}(\mathbf{x}, \sigma_\Delta) \cdot \mathbf{F} + \mathbf{T}(\mathbf{x}, \sigma_\Theta) \cdot \boldsymbol{\tau},\tag{3.3}$$

where \mathbf{N} and \mathbf{T} are second rank tensors, i.e. FCM's Green's functions, given by (Maxey and Patel (2001); Lomholt and Maxey (2003))

$$\begin{aligned}
 N_{ij}(\mathbf{x}, \sigma) &= \frac{1}{8\pi\eta r} \left(\delta_{ij} + \frac{x_i x_j}{r^2} \right) \operatorname{erf} \left(\frac{r}{\sigma\sqrt{2}} \right) + \frac{1}{8\pi\eta} \left(\frac{\delta_{ij}}{r^3} - 3\frac{x_i x_j}{r^5} \right) \sigma^2 \operatorname{erf} \left(\frac{r}{\sigma\sqrt{2}} \right) \\
 &\quad - \frac{\sigma^2}{2\eta(2\pi\sigma^2)^{3/2}} \left(\delta_{ij} - 3\frac{x_i x_j}{r^2} \right) \frac{\sigma^2}{r^2} \exp \left(-\frac{r^2}{2\sigma^2} \right), \tag{3.4}
 \end{aligned}$$

and,

$$T_{ij}(\mathbf{x}, \sigma) = -\frac{1}{8\pi\eta r^3} \left[\operatorname{erf} \left(\frac{r}{\sigma\sqrt{2}} \right) - \frac{r}{\sigma} \left(\frac{2}{\pi} \right)^{1/2} \right] \exp \left(-\frac{r^2}{2\sigma^2} \right) \varepsilon_{ijk} x_k. \tag{3.5}$$

After solving Eq. (3.1), the velocity, \mathbf{V} , angular velocity, $\mathbf{\Omega}$ of the particle is found by volume averaging of the resulting fluid flow (Eq. 3.3),

$$\mathbf{V} = \int \mathbf{u} \Delta(\mathbf{x}) d^3 \mathbf{x} \tag{3.6}$$

$$\mathbf{\Omega} = \frac{1}{2} \int [\nabla \times \mathbf{u}] \Theta(\mathbf{x}) d^3 \mathbf{x}, \tag{3.7}$$

where the integration is performed over \mathbb{R}^3 . In order for Eqs. (3.6) – (3.7) to recover the correct mobility relations for a single, isolated sphere, namely that $\mathbf{V} = \mathbf{F}/(6\pi a\eta)$ and $\mathbf{\Omega} = \boldsymbol{\tau}/(8\pi a^3\eta)$, the envelope length scales need to be $\sigma_\Delta = a/\sqrt{\pi}$ and $\sigma_\Theta = a/(6\sqrt{\pi})^{1/3}$.

3.1.2 Squirmer model

In addition to undergoing rigid body motion in the absence of applied forces or torques, active and self-propelled particles are also characterized by the flows they generate. To model such particles, we will need to incorporate these flows into FCM. We accomplish this by adapting the squirmer model (Lighthill (1952); Blake (1971); Ishikawa et al. (2006)) to the FCM framework.

The squirmer model consists of a spherically shaped, self-propelled particle that utilizes axisymmetric surface distortions to move through fluid with speed U in the direction \mathbf{p} . If the amplitude of the distortions is small compared to the radius, a , of the squirmer, their effect can be represented by the surface velocity, $\mathbf{v}(r = a) = v_r \hat{\mathbf{r}} + v_\theta \hat{\boldsymbol{\theta}}$ where

$$v_r = U \cos \theta + \sum_{n=0}^{\infty} A_n(t) P_n(\cos \theta), \tag{3.8}$$

$$v_\theta = -U \sin \theta - \sum_{n=1}^{\infty} B_n(t) V_n(\cos \theta). \tag{3.9}$$

Here, $P_n(x)$ are the Legendre polynomials,

$$V_n(\cos \theta) = \frac{2}{n(n+1)} \sin \theta P'_n(\cos \theta), \tag{3.10}$$

the angle θ is measured with respect to the swimming direction \mathbf{p} , and $P'_n(x) = dP_n/dx$. In order for the squirmer to be force-free, we have

$$U = \frac{1}{3}(2B_1 - A_1). \quad (3.11)$$

Following [Ishikawa et al. \(2006\)](#), we consider a reduced squirmer model where $A_n = 0$ for all n and $B_n = 0$ for all $n > 2$. We therefore only have the first two terms of the series. For this case, the resulting flow field in the frame moving with the swimmer is given by

$$\mathbf{u}_r(r, \theta) = \frac{2}{3}B_1 \frac{a^3}{r^3} P_1(\cos \theta) + \left(\frac{a^4}{r^4} - \frac{a^2}{r^2} \right) B_2 P_2(\cos \theta) \quad (3.12)$$

$$\mathbf{u}_\theta(r, \theta) = \frac{1}{3}B_1 \frac{a^3}{r^3} V_1(\cos \theta) + \frac{a^4}{r^4} B_2 V_2(\cos \theta) \quad (3.13)$$

where we have used $U = 2B_1/3$ from Eq. (3.11). In terms of \mathbf{p} , \mathbf{x} , and r , this becomes

$$\begin{aligned} \mathbf{u}(\mathbf{x}) &= -\frac{B_1 a^3}{3 r^3} \left(\mathbf{I} - 3 \frac{\mathbf{x}\mathbf{x}^T}{r^2} \right) \mathbf{p} + \left(\frac{a^4}{r^4} - \frac{a^2}{r^2} \right) B_2 P_2 \left(\frac{\mathbf{p} \cdot \mathbf{x}}{r} \right) \frac{\mathbf{x}}{r} \\ &\quad - 3 \frac{a^4}{r^4} B_2 \left(\frac{\mathbf{p} \cdot \mathbf{x}}{r} \right) \left(\mathbf{I} - \frac{\mathbf{x}\mathbf{x}^T}{r^2} \right) \mathbf{p}. \\ &= \mathbf{u}_{B_1} + \mathbf{u}_{B_2} \end{aligned} \quad (3.14)$$

Fig. 3.1 shows an example of a flow field given by Eq. (3.14), as well as the flows \mathbf{u}_{B_1} and \mathbf{u}_{B_2} related to the B_1 and B_2 contributions.

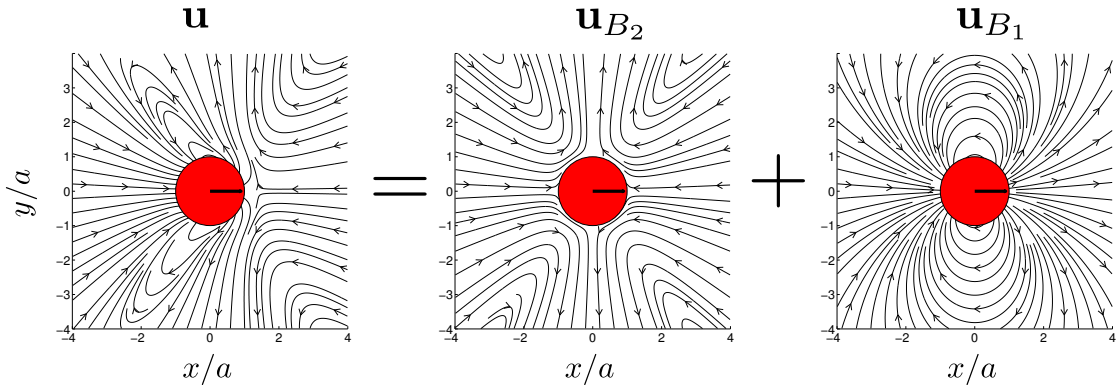


Figure 3.1: Decomposition of squirmer velocity field for $\beta = 1$.

While we have already seen that B_1 is related to the swimming speed, it can be shown ([Ishikawa et al. \(2006\)](#)) that B_2 is directly related to the stresslet

$$\mathbf{G} = \frac{4}{3} \pi \eta a^2 (3\mathbf{p}\mathbf{p} - \mathbf{I}) B_2 \quad (3.15)$$

generated by the surface distortions. This term sets the leading-order flow field that decays like r^{-2} . We can introduce the parameter $\beta = B_2/B_1$ which describes the relative stresslet strength. In addition, if $\beta > 0$, the squirmer behaves like a ‘puller,’ bringing

fluid in along \mathbf{p} and expelling it laterally, whereas if $\beta < 0$, the squirmer is a ‘pusher’, expelling fluid along \mathbf{p} and bringing it in laterally.

To adapt this model to the FCM framework, we first recognize that the flow given by Eq. (3.14) can be represented by the following singularity system in the Stokes equations

$$\nabla p - \eta \nabla^2 \mathbf{u} = \mathbf{G} \cdot \nabla \left(\delta(\mathbf{x}) + \frac{a^2}{6} \nabla^2 \delta(\mathbf{x}) \right) + \mathbf{H} \nabla^2 \delta(\mathbf{x}) \quad (3.16)$$

$$\nabla \cdot \mathbf{u} = 0 \quad (3.17)$$

where the degenerate quadrupole is related to B_1 through

$$\mathbf{H} = -\frac{4}{3} \pi \eta a^3 B_1 \mathbf{p}. \quad (3.18)$$

and the stresslet \mathbf{G} is given by Eq. (3.15). We can draw a parallel between these singularities and the regularized singularities used with FCM. The stresslet term in Eq. (3.16) is the gradient of the singularity system for a single sphere subject to an applied force. Accordingly, the corresponding regularized singularity in FCM is $\nabla \Delta(\mathbf{x})$, where $\Delta(\mathbf{x})$ is given by Eq. (6.2). It is important to note that even though we replace two singular force distributions with the one regularized FCM distribution, the particular choice of $\Delta(\mathbf{x})$ will yield flows that are asymptotic to both singular flow fields (Maxey and Patel (2001)). For the degenerate quadrupole, however, there is not a corresponding natural choice for the regularized distribution. Following Keaveny and Maxey (2008b), we choose a Gaussian envelope with a length-scale small enough to yield an accurate representation of the singular flow, but not so small as to significantly increase the resolution needed in a numerical simulation (see Section 3.1.3). We therefore employ the FCM envelope for the force dipole and replace the singular distribution by $\nabla^2 \Theta(\mathbf{x})$.

Thus, for a single squirmer the Stokes equations with the FCM squirmer force distribution are

$$\begin{aligned} \nabla p - \eta \nabla^2 \mathbf{u} &= \mathbf{G} \cdot \nabla \Delta(\mathbf{x}) + \mathbf{H} \nabla^2 \Theta(\mathbf{x}) \\ \nabla \cdot \mathbf{u} &= 0. \end{aligned} \quad (3.19)$$

With FCM, additional effects can readily be incorporated into the squirmer model and in our subsequent simulations, we consider several of them to demonstrate the versatility of our approach. In the case of an isolated swimmer, gravitational forces and external torques experienced by heavy, magnetotactic or gyrotactic organisms can be considered by including them in \mathbf{F} and $\boldsymbol{\tau}$.

Adding such features to Eq. (3.19), one obtains

$$\begin{aligned} \nabla p - \eta \nabla^2 \mathbf{u} &= \mathbf{F} \Delta(\mathbf{x}) + \frac{1}{2} \boldsymbol{\tau} \times \nabla \Theta(\mathbf{x}) \\ &+ \mathbf{G} \cdot \nabla \Delta(\mathbf{x}) + \mathbf{H} \nabla^2 \Theta(\mathbf{x}) \end{aligned} \quad (3.20)$$

$$\nabla \cdot \mathbf{u} = 0. \quad (3.21)$$

The resulting velocity field generated by an isolated squirmer subject to external forces and torques is then given by

$$\mathbf{u}^{FCM} = \mathbf{N}(\mathbf{x}, \sigma_\Delta) \cdot \mathbf{F} + \mathbf{T}(\mathbf{x}, \sigma_\Theta) \cdot \boldsymbol{\tau} + \mathbf{A}(\mathbf{x}, \sigma_\Theta) \cdot \mathbf{H} + \mathbf{R}(\mathbf{x}, \sigma_\Delta) : \mathbf{G}. \quad (3.22)$$

\mathbf{A} is a second rank tensors given by (Maxey and Patel (2001); Lomholt and Maxey (2003))

$$\begin{aligned} A_{ij}(\mathbf{x}, \sigma) &= \frac{1}{4\pi\eta r^3} \left[\delta_{ij} - \frac{3x_i x_j}{r^2} \right] \operatorname{erf} \left(\frac{r}{\sigma\sqrt{2}} \right) \\ &\quad - \frac{1}{\eta(2\pi\sigma^2)^{3/2}} \left[\left(\delta_{ij} - \frac{x_i x_j}{r^2} \right) + \left(\delta_{ij} - \frac{3x_i x_j}{r^2} \right) \left(\frac{\sigma}{r} \right)^2 \right] \exp(-\mathbf{x}^2/2\sigma^2). \end{aligned} \quad (3.23)$$

The expression for the third rank tensor \mathbf{R} is (Lomholt and Maxey (2003))

$$\begin{aligned} R_{ijk}(\mathbf{x}, \sigma) &= -\frac{3}{8\pi\eta r^5} x_i x_j x_k \operatorname{erf} \left(\frac{r}{\sigma\sqrt{2}} \right) + \frac{3\sigma^2}{8\pi\eta r^7} \operatorname{erf} \left(\frac{r}{\sigma\sqrt{2}} \right) (5x_i x_j x_k - 2r^2 \delta_{ij} x_k) \\ &\quad + \frac{1}{8\pi\eta r^4 \sigma} \frac{1}{\sqrt{2\pi}} \exp \left(-\frac{r^2}{2\sigma^2} \right) \left[4(r^2 \delta_{ij} x_k - x_i x_j x_k) - \frac{6\sigma^2}{r^2} (5x_i x_j x_k - 2r^2 \delta_{ij} x_k) \right] \end{aligned} \quad (3.24)$$

It is important to remind that the flow generated by a squirmer results from a real boundary condition associated the swimming gait. This model is thus more realistic than the far-field dipolar approximation resulting from the force- and torque-free requirements at zero Reynolds number.

3.1.3 Comparison with Blake's solution

Fig. 3.2 shows, Blake's solution Eq. (3.14), and the velocity field provided by Eq. (3.22) with two different values for the degenerate quadrupole Gaussian envelope size, σ_Θ and $\sigma_\Theta/2$, that appears in the tensor \mathbf{A} . The streamlines are identical, except for a near-field recirculating region that appears when the width of the degenerate quadrupole envelope is σ_Θ (Fig. 3.2b). In this region, however, the magnitude of the velocity is small compared to the swimming speed. This region should not significantly impact the squirmer-squirmer hydrodynamic interactions that we are aiming to resolve.

A quantitative comparison of the velocity field is provided in Fig. 3.3. The agreement with Blake's solution is very good for $r/a > 1.25$ when using σ_Θ for the width of the degenerate quadrupole envelope. As shown in Fig. 3.3b, the smaller envelope size ($\sigma_\Theta/2$) matches Blake's solution more closely for $r/a < 1.2$, with clear improvement at the front and rear of the squirmer. For this envelope size, the velocity field induced by the degenerate quadrupole $\mathbf{u}_{B_1}^{FCM}$ matches exactly the analytical solution \mathbf{u}_{B_1} in Eq. (3.14) (not shown here). Below this width no quantitative improvement is observed as the remaining error comes from the dipolar contribution, \mathbf{u}_{B_2} .

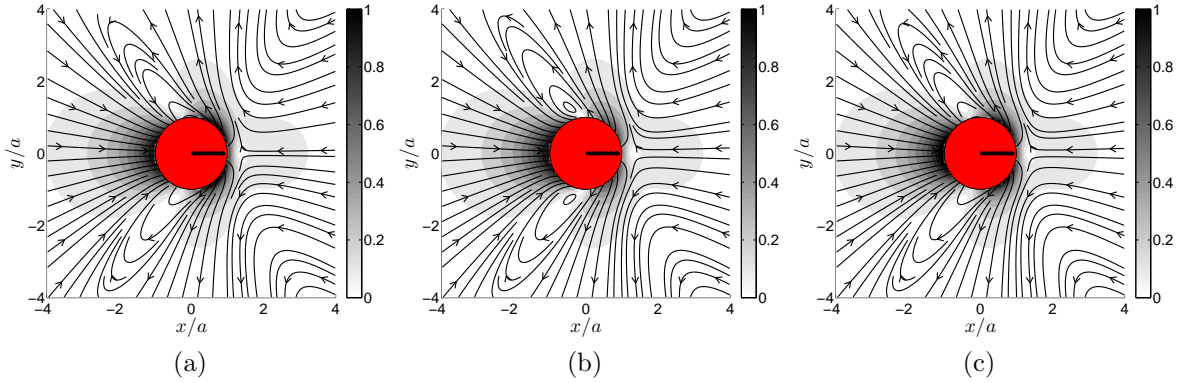


Figure 3.2: Velocity field \mathbf{u}/U around a puller squirmer ($\beta = 1$) swimming to the right. (a) Blake's solution; (b) FCM solution with σ_Θ for the degenerate quadrupole envelope. (c) FCM solution with $\sigma_\Theta/2$ for the degenerate quadrupole envelope.

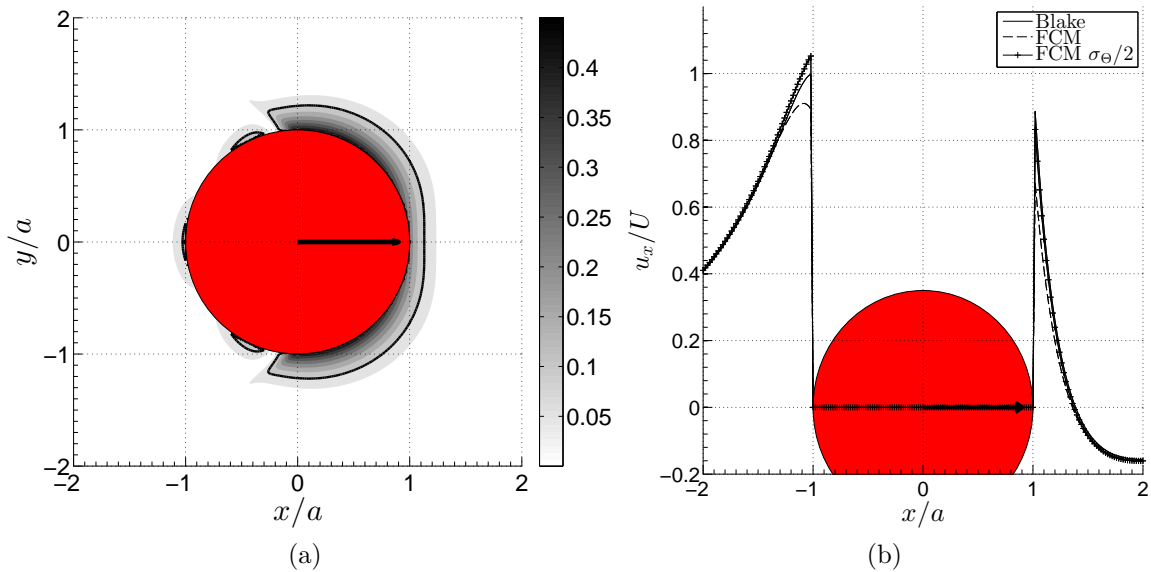


Figure 3.3: Comparison with Blake's solution, Eq. (3.14). (a) Normalized difference, $\|\mathbf{u}^{\text{Blake}} - \mathbf{u}^{\text{FCM}}\|/U$, between FCM and Blake's solution for a puller squirmer ($\beta = 1$). The half-width for the degenerate quadrupole envelope is σ_Θ . — : 10% iso-value. (b) Velocity profile along the swimmer axis for Blake's solution and the FCM approximation for the two different degenerate quadrupole envelope sizes.

While this quantitative comparison provides a nice way to choose the degenerate quadrupole envelope size, we must also keep in mind the computational cost associated with decreasing this length scale. As we will show in Section 6.1.1, even though it would yield a flow field slightly more in register with Blake’s solution, resolving the length scale $\sigma_\Theta/2$ in a 3D simulation would require a grid with 8 times as many points as that needed for σ_Θ , the smallest length-scale already in FCM. This would increase computation times by at least an order of magnitude. In addition, the FCM volume averaging detailed in Section 6.1.1 to determine the squirmer translational and angular velocities will reduce the contribution of the localized velocity field discrepancies to the squirmer-squirmer interactions. In our subsequent simulations, we therefore utilize σ_Θ for the degenerate quadrupole envelope size since reducing this length-scale would significantly increase the computational cost, but only provide a minimal improvement.

3.2 A time-dependent squirmer model based on experimental data

Here, we show how to incorporate time-dependence into our model. Using the procedure outlined in Ghose and Adhikari (2014), we determine the time-dependent multipole coefficients $B_1(t)$ and $B_2(t)$ from the experimental data provided in Guasto et al. (2010) for *Chlamydomonas reinhardtii*. By allowing these parameters to be functions of time, the FCM squirmer model can be used to explore how the swimmers’ strokes disturb the surrounding fluid and affect the overall suspension dynamics. In Section 3.2.2, we perform a preliminary investigation to check whether the model proposed here is applicable to larger micro-swimmers such as the *Arcatia tonsa* copepod.

3.2.1 Time-dependent model for *Chlamydomonas reinhardtii*

Recent experiments (Guasto et al. (2010)) quantified the periodic swimming gait and resulting flow field of the algae cell *Chlamydomonas reinhardtii*. They extracted the swimming speed, the induced velocity field, and the power dissipation, showing also that all can be represented as periodic functions of time. A recent theoretical investigation (Ghose and Adhikari (2014)) showed that these quantities could be reproduced using a multipole-based model. In their study, they consider three time-dependent multipoles: a stresslet, a degenerate quadrupole (or potential dipole) and a “septlet.” The stresslet decays as r^{-2} whereas the degenerate quadrupole and the “septlet” decay as r^{-3} . Here, we utilize only the stresslet and degenerate quadrupole terms and find that they are sufficient to reproduce Guasto et al. (2010)’s measurements.

The measured swimming speed from Guasto et al. (2010), $U(t)$, can be represented using the truncated Fourier series in time (see Ghose and Adhikari (2014)):

$$U(t) = a_0 + a_1 \cos(\omega t) + a_2 \cos(2\omega t) + b_1 \sin(\omega t) + b_2 \sin(2\omega t) \quad (3.25)$$

where ω is the frequency of the swimming gait. The mean swimming speed over one beat period, $T = 2\pi/\omega$, is given by $a_0 = 49.54a \cdot s^{-1}$, where $a = 2.5\mu m$ is the radius

of the micro-organism. The values for the remaining coefficients are provided in the supplementary information of [Ghose and Adhikari \(2014\)](#). From Eq. (3.11), we can immediately determine the time-dependent degenerate quadrupole strength

$$B_1(t) = \frac{3}{2}U(t) \quad (3.26)$$

in order to preserve the instantaneous force-free condition. Unlike this term, there is more than one way to calibrate the stresslet strength, $B_2(t)$. For example, one could determine $B_2(t)$ using the power dissipation measurements from [Guasto et al. \(2010\)](#) and Eq. (3.11) from [Blake \(1972\)](#)

$$\Pi_d(t) = \frac{2}{3}\pi\eta a (8B_1(t)^2 + 4B_2(t)^2). \quad (3.27)$$

for the power dissipated by a squirmer. Using this approach, we found that our resulting flow field did not match the experimental results of [Guasto et al. \(2010\)](#). We instead determine $B_2(t)$ directly from the experimental flow field by fitting to the location of the moving stagnation point. [Ghose and Adhikari \(2014\)](#) adopted the same approach. We utilize three Fourier modes to describe the time evolution of B_2

$$B_2(t) = c_0 + c_1 \cos(\omega t + \varphi_{c1}) + c_2 \cos(2\omega t + \varphi_{c2}) + c_3 \cos(3\omega t + \varphi_{c3}) \\ + s_1 \sin(\omega t + \varphi_{s1}) + s_2 \sin(2\omega t + \varphi_{s2}) + s_3 \sin(3\omega t + \varphi_{s3}), \quad (3.28)$$

where the amplitudes c_0, c_1, s_1, \dots and phases $\varphi_{c1}, \varphi_{s1}, \dots$ are manually fitted. Tables 3.1 and 3.2 give the resulting values of these parameters.

c_0	c_1	c_2	c_3	s_1	s_2	s_3
4.5347	64.053	-84.7192	-10.4545	91.4529	-92.6420	-5.9849

Table 3.1: Magnitudes of the Fourier modes used to describe $B_2(t)$ in $\text{radii}\cdot s^{-1}$.

φ_{c1}	φ_{c2}	φ_{c3}	φ_{s1}	φ_{s2}	φ_{s3}
1.7373	3.5761	-0.9154	0.1666	2.0054	-1.7125

Table 3.2: Phases of the Fourier modes used to describe $B_2(t)$ in rad .

The phase diagram in Fig. 3.4a shows the value of B_1 versus B_2 and it is similar to that found by [Ghose and Adhikari \(2014\)](#). We extract the average value of $\bar{\beta}(t) = B_2(t)/B_1(t)$ over one beat cycle

$$\bar{\beta} = \frac{1}{T} \int_0^T B_2(t)/B_1(t) dt = 0.1 \quad (3.29)$$

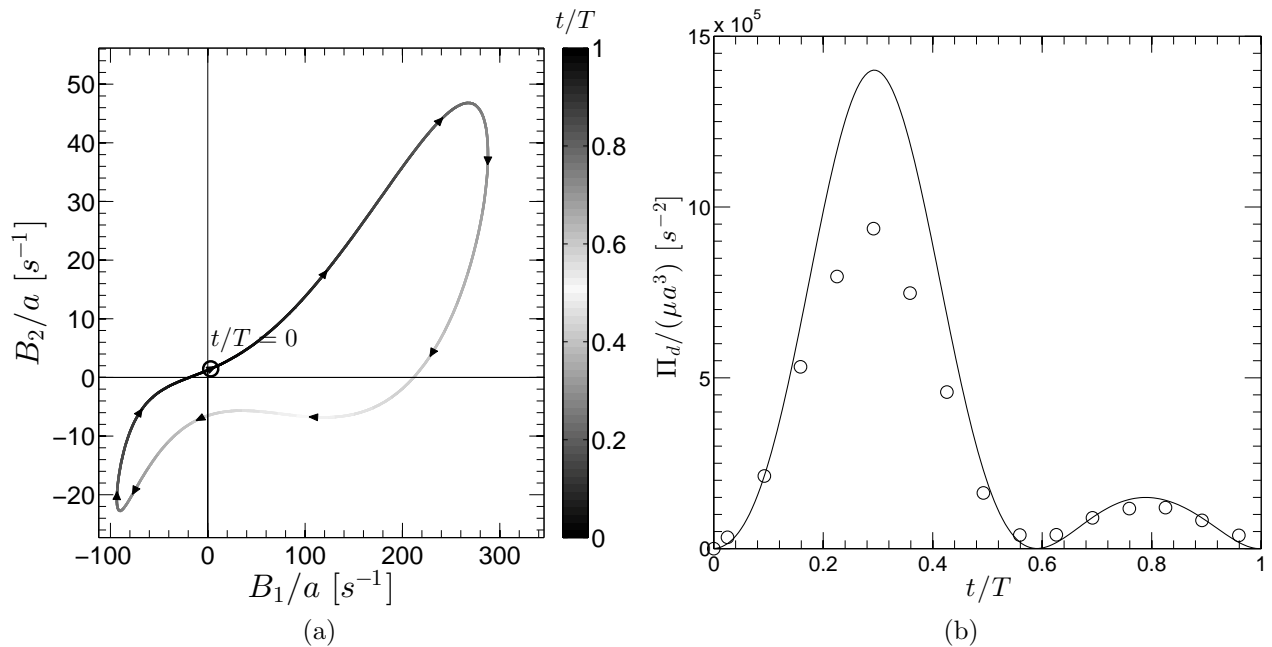


Figure 3.4: a) $(B_1(t), B_2(t))$ phase diagram for one beat cycle. b) Power dissipation $\Pi_d(t)$ over one beat cycle. — : FCM, \circ : results from [Guasto et al. \(2010\)](#).

which corresponds to a puller squirmer with a relatively small stresslet magnitude. Fig. 3.4b shows the resulting power dissipation as determined from Eq. (3.27). It reaches a peak value at $t/T \approx 0.3$, which coincides with the time at which the swimming speed reaches its maximum value. We note that unlike [Guasto et al. \(2010\)](#) our swimmers generate axisymmetric flow fields and we are considering a 3D periodic domain. Despite this, we achieve a qualitatively similar power dissipation profile with slightly greater values during the first half of the beat cycle.

Fig. 3.5 shows the flow field around our model of *C. reinhardtii* at six different times during its beat cycle. These time points are chosen to correspond to those in Fig. 3 of [Guasto et al. \(2010\)](#). We achieve very similar streamlines and, by construction, the position of the stagnation point matches very well the experimental data. We also note that our flow field is similar to that given by the multipole model found in [Ghose and Adhikari \(2014\)](#) even though we do not include the rapidly decaying “septlet” term in our model. These results illustrate that our properly tuned, time-dependent squirmer model can yield flow fields very similar to those of real organisms.

3.2.2 Time-dependent model for the copepod *Arcatia tonsa*: preliminary investigations

The modeling approach used for the algae *C. reinhardtii* can be readily extended to other micro-organisms. To test this idea, Navish Wadhwa, from the Centre for Ocean Life at the Technical University of Denmark, and I, started a preliminary study in February 2015.

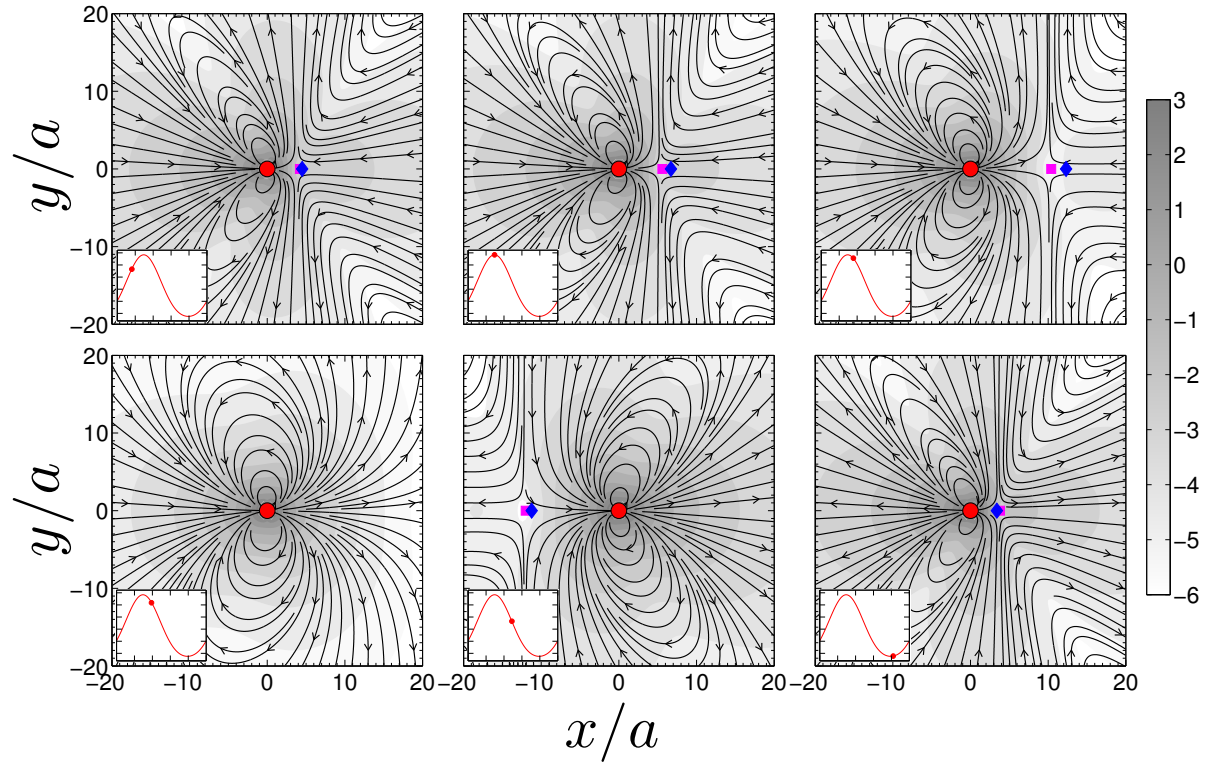


Figure 3.5: Snapshots of the time-dependent flow field around a model *Chlamydomonas*. Background grey levels represent the natural logarithm of the norm of the velocity field in $\text{rad} \cdot \text{s}^{-1}$. \blacksquare : position of the stagnation point given by the FCM model. \blacklozenge : position of the stagnation point measured by [Guasto et al. \(2010\)](#). (Insets) Swimming speed along the beat cycle.

His joint work with Pr. Thomas Kiørboe and Pr. Anders Peter Andersen focuses on the disturbances generated by the swimming and feeding of plankton (Wadhwa et al. (2014); Kiørboe et al. (2014)). Together with Jeff Guasto’s coworkers, they belong to the very few teams who performed micro-PIV measurements of the flow field around swimming micro-organisms along their beat cycle. In this section, we focus on the swimming of the copepod *Arcatia tonsa* at its naupliar stage, i.e. at its early development.

The copepod *Arcatia tonsa*

Copepods are millimeter-sized crustaceans that are omnipresent in both marine and fresh-water aquatic systems. Being prey and predator at the same time, they form a vital part of the oceanic food web. During their naupliar stage, copepods move with a breast-stroke swimming gait. Contrarily to *C. reinhardtii*, its beating cycle is not permanent and periodic. Instead, the nauplius alternates successive “jumps”, composed of a quick power stroke, a slow recovery stroke, and motionless stages. Figure 3.6 shows the time series of the flow around a swimming nauplius.

Their typical body length is $L = 0.22mm$ and their mean swimming speed is $U = 37.4mm.s^{-1}$ (Wadhwa et al. (2014)). *Arcatia tonsa* are slightly heavier than the surrounding water $\rho/\rho_f \approx 1070/1000$. They evolve in the realm of intermediate Reynolds number, with an average value of $Re = 7.9$. In this regime the multipole expansion derived above for low Reynolds number flows, may not be appropriate to reproduce the swimming hydrodynamic disturbances. However, Wadhwa et al. (2014) and Kiørboe et al. (2014) showed that the averaged flow decays as r^{-2} , in a stresslet-like fashion. This preliminary study thus aims at identifying the range of validity of our generic approach.

Procedure

To reproduce the flow field around *Arcatia tonsa* we designed an optimization routine whose criterion for the calibration of the stresslet coefficient $B_2(t)$ is the L_2 -norm between the measured and the modeled velocity field. The body of the copepod is approximated with a sphere of radius equal to its body half-length $a = L = 0.22mm$. The monopole corresponding to the buoyancy force is

$$\mathbf{F} = -\frac{4}{3}\pi a^3(\rho - \rho_f)g\hat{\mathbf{z}}, \quad (3.30)$$

where $g = 9.81m.s^{-2}$ is the gravitational acceleration and $\hat{\mathbf{z}}$ is the direction of gravity. We compute the velocity disturbances generated by the model *Arcatia tonsa* with the FCM framework for isolated particles (Eq. 3.22).

PIV data was post-processed using a routine from Navish Wadhwa that I adapted for the purpose of parameter calibration. The automated program to find the optimal $B_2(t)$ has been implemented in MatlabTM.

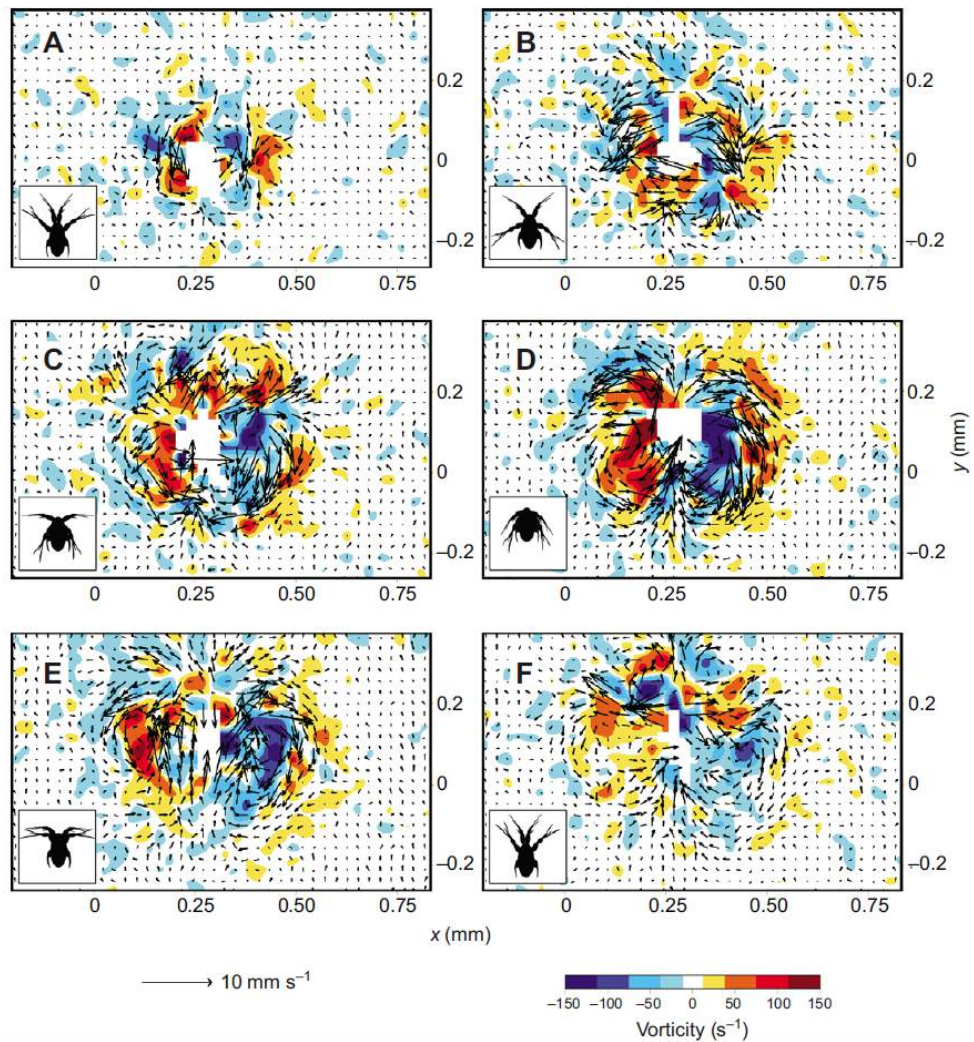


Figure 3.6: Snapshots of the time-dependent (A-F) flow field around a copepod *Arcatia tonsa* at its naupliar stage. This figure is taken from [Wadhwa et al. \(2014\)](#).

Conclusions: Model vs. reality

Figure 3.7 compares the model to the PIV data at different stages in the beat of the nauplius. The model is able to reproduce qualitatively, sometimes quantitatively, the flow field around *Arcatia tonsa*. However, the fluid inertia is such that the flow field around the copepod always depends on the previous states. As an illustration, the flow dragged behind the swimmer during the power stroke never really disappears during the recovery stroke. As illustrated on Figure 3.7b, the squirmer model for Stokes flow is not appropriate to take into account the fluid memory. Many different tricks could be used to overcome this problem. For instance, one could apply a delay operator or a convolution product integrated over a time interval of the order of the viscous dissipation time. But such artifices are not rigorous and their choice is somehow arbitrary.

The best way to reproduce correctly the disturbances around such micro-organisms would be to include fluid inertia. Indeed it would be interesting, and feasible, to use our time dependent model in a Navier-Stokes solver.

3.2 A time-dependent squirmer model based on experimental data

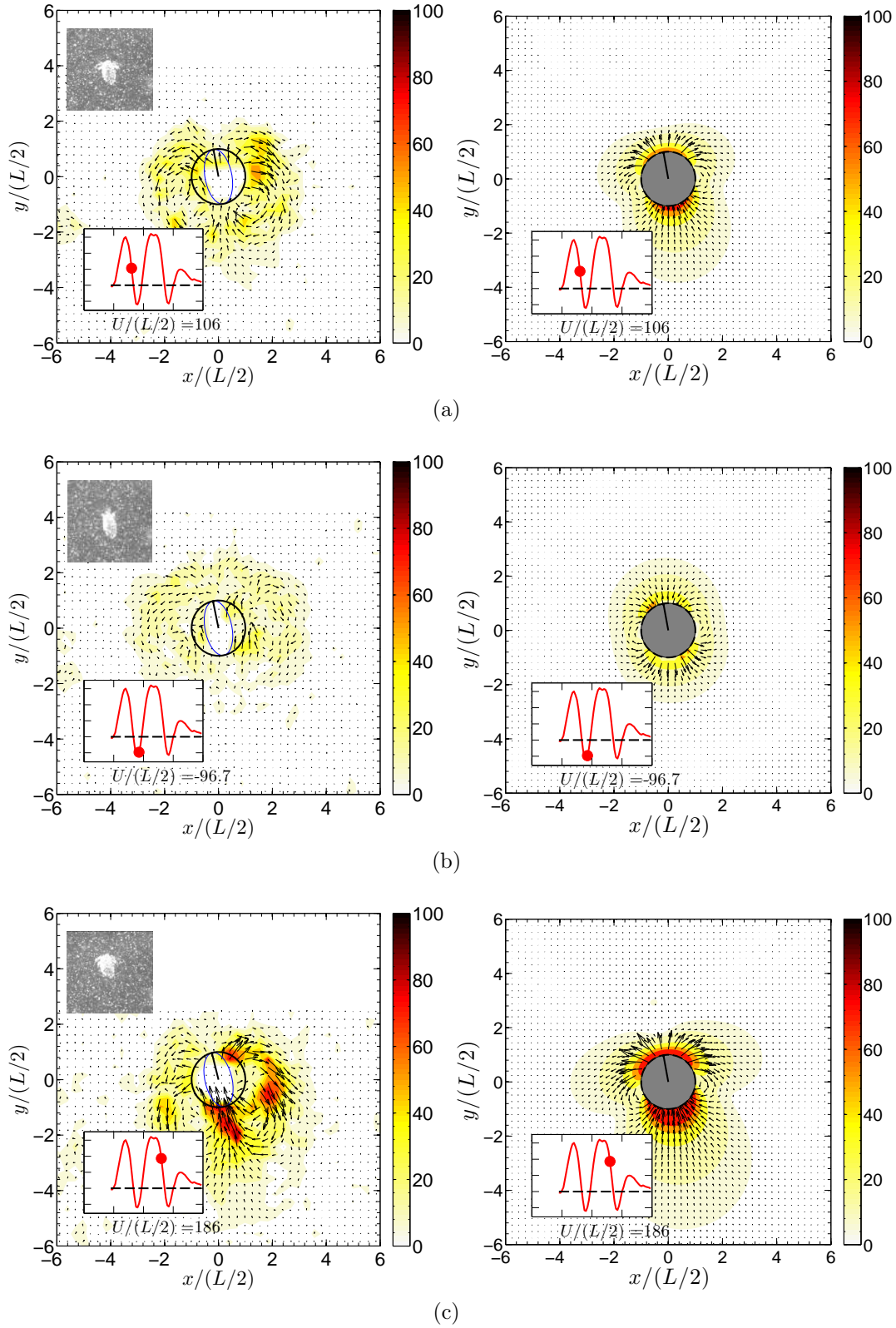


Figure 3.7: Flow field around *Arcatia tonsa* at different times along the breaststroke. Vector scale is 1/100. The contours represent the norm of the velocity field $\|\mathbf{u}\|/(L/2)$. Left: experimental data. Right: model.

Chapter 4

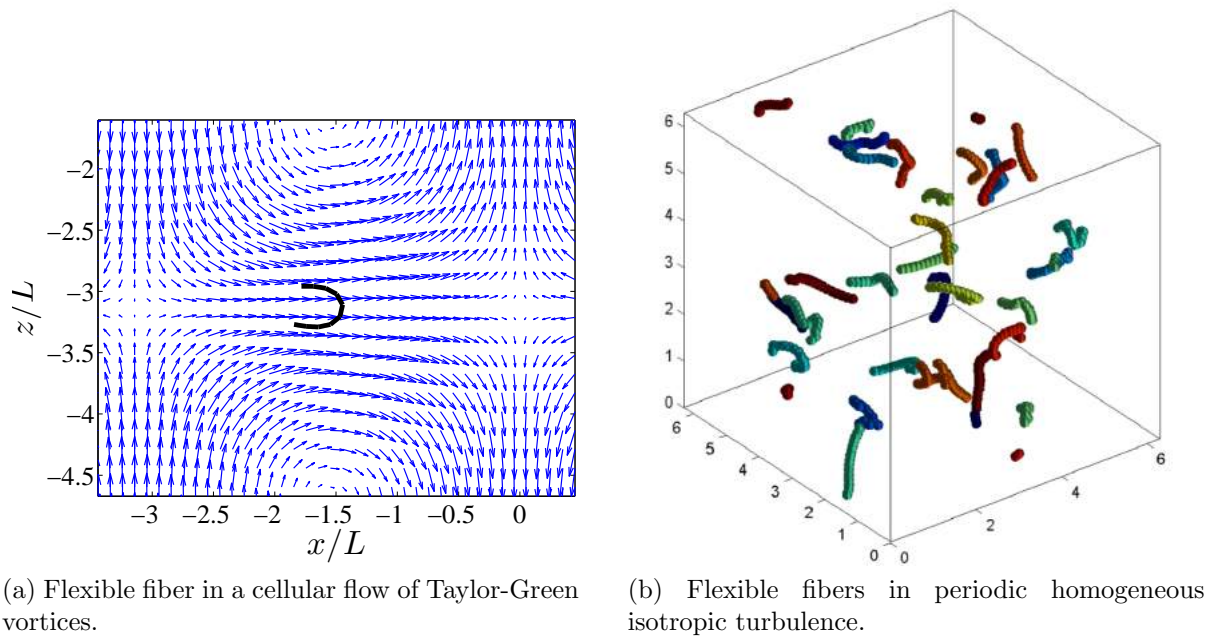
Conclusions: towards large multiscale simulations of active suspensions.

In the first part of this thesis we addressed the modeling of swimming mechanisms and the hydrodynamic disturbances they generate at the scale of the micro-swimmers.

In Chapter 2 we proposed an improvement of the bead model to solve the complex underlying fluid-structure interactions problem and proved its ability to satisfactorily reproduce experimental and numerical results on passive and active objects. We have provided a simple general theoretical framework for kinematic constraints to be used in three-dimensional bead models. This framework permits to handle versatile and complex kinematic constraints between flexible assembly of spheres at low Reynolds numbers. Planar and helical beating of flexible fibers have been successfully addressed, and more complex assembly can be easily treated within a similar framework. We have also introduced a contact model, the gears model (GM), which presents several numerical advantages over previous contact models: stability, generic nature and simplicity. In a recent work (Thiam (2014)) we have shown how the linearity of the proposed formulation can be exploited to calibrate constitutive parameters of flexible objects with experimental data.

Extensions of the model to passive and active flexible objects in cellular and turbulent flows have been implemented (Figure 4.1) and comparisons with experimental and numerical studies (Brouzet et al. (2014); Young and Shelley (2007); Quennouz et al. (2015)) are in progress.

The approach presented in Chapter 3 builds from the spherical squirmer model developed by Blake (1971), by including the regularized singularities which correspond to the surface squirming modes in the force-coupling method (FCM). We demonstrated the accuracy of our model by comparing velocity fields with Blake's analytic solution. We have shown that the time-dependency of the swimming gaits can be readily included in our model by tuning it to available experimental data (Guasto et al. (2010); Wadhwa et al. (2014)). Even though the squirmer model was originally derived for ciliated



(a) Flexible fiber in a cellular flow of Taylor-Green vortices.

(b) Flexible fibers in periodic homogeneous isotropic turbulence.

Figure 4.1: Current extensions of the Gears Model (in progress).

micro-organisms, such as *Volvox*, the agreement obtained with experimental measurement around the breast-stroke swimmer *C. reinhardtii* is strikingly good and thus promising. However, the steady Stokes flow assumption is not valid for the zooplankton studied in Section 3.2.2. In future work, we will solve the unsteady Stokes equation forced with the same time-dependent singularities to improve the agreement with experimental measurements. Having a good model for plankton swimming and hydrodynamic disturbances would provide an interesting tool to study and comprehend prey-predator systems (Kjørboe et al. (2014)).

Letting our imagination drift a bit from reality, having the design and optimization of artificial micro-robots in mind, we could also invent new swimming gaits and evaluate their efficiency (Felderhof (2015)). Figure 4.2 shows examples of “exotic” swimming gaits in the phase space $(B_1(t), B_2(t))$ that could be analyzed in future work, and may correspond to real micro-organisms. It would also be interesting to tune our model to similar experimental data, but for a wider zoology of micro-organisms (Kjørboe et al. (2014)). We could therefore assess the possible differences in collective dynamics exhibited by different species, or even look into how one species might interact with another.

Finally, it is worth mentioning the very recent work of Brotto et al. (2015) on continuum and particle-based models for active cyclic swimmers. Even though their model is more phenomenological than our approach based on experimental data, they provide an interesting framework to include time-dependent singularities in continuum models.

The squirmer model and its time-dependent variants were developed in Chapter 3 with the extension to large multiscale simulations in mind. However, including hydrodynamic

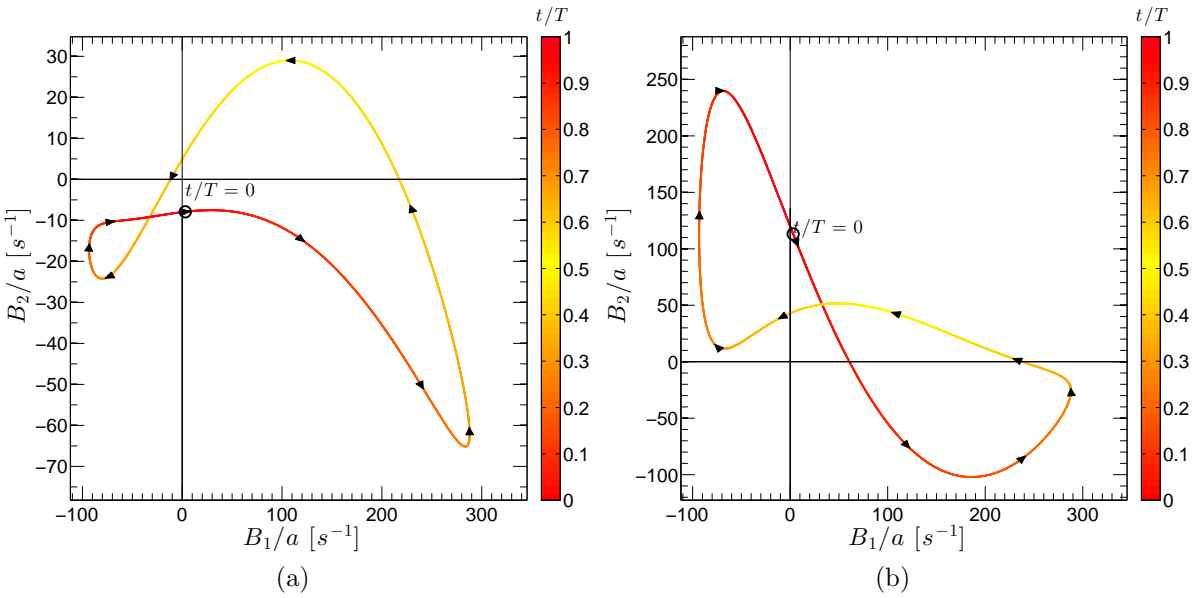


Figure 4.2: “Exotic” swimming gaits in the phase space $(B_1(t), B_2(t))$.

interactions and Brownian motion for large collections of micro-swimmers and Brownian particles in suspensions, while preserving a good and quantifiable level of accuracy, is a modeling and numerical challenge that few methods can take. In the next part (Part II), we provide a numerical framework based on the force-coupling method and fluctuating hydrodynamics to further address these questions in the context of High Performance Computing (HPC).

Part II

From Small to Large Scales: A Modeling Challenge

Chapter 5

Introduction: models for the multiscale physics of active suspensions.

Contents

5.1 How to model active suspension ?	79
5.2 Brownian motion in particulate suspensions.	81

The length scales involved in active suspensions span several orders of magnitudes: the smallest micro-swimmers, appendages and tracer particles used in experiments are typically micron-sized ($10^{-6}m$), collective motion and/or mixing occur at much larger scales ($10^{-5} - 10^{-4}m$), while typical sample sizes or interrogation windows at the lab/in situ scale can reach several millimeters ($10^{-3}m$). Modeling such systems thus requires addressing both the physics at the small scales, where thermal fluctuations play an important role, and at the large scales, where several thousands ($10^3 - 10^5$ and more) individuals are involved. In the first section of this chapter, we briefly review the literature on the modeling of “deterministic” active suspensions. In the second section we summarize the situations in which thermal agitation plays a significant role and expose the issues that motivate the derivation of new integration schemes for particle Brownian motion.

5.1 How to model active suspension ?

The mathematical modeling of active suspensions entails describing how individual swimmers move and interact in response to the flow fields that they generate (O’Malley and Bees (2012); Wadhwa et al. (2014)). It is particularly important for these models to be able to handle a large collection of swimmers in order to obtain suspension properties at the lab/*in situ* scale. The modeling of the collective behavior of active matter has been a vibrant area of research during the last decade (Ramaswamy (2010); Koch and Subramanian (2011); Saintillan and Shelley (2013); Marchetti et al. (2013); Saintillan and Shelley

(2015)), to cite only a few recent reviews. Generally speaking, the modelling approaches can be sorted into two categories: continuum theories and particle-based simulations. Most of the continuum models are generally valid for dilute suspensions where the hydrodynamic disturbances are given by a mean-field description of far-field hydrodynamic interactions (Saintillan and Shelley (2008); Baskaran and Marchetti (2009); Koch and Subramanian (2011)). Recent advances towards more concentrated suspensions include steric interactions (Ezhilan et al. (2013)), but the inclusion of high-order singularities due to particle size remains outstanding. Despite this, these models are very attractive as they naturally provide a description of the dynamics at the population level and the resulting equations can be analyzed using a wide range of analytical and numerical techniques.

Particle-based simulations resolve the dynamics of each individual swimmer and from their positions and orientations, construct a picture of the dynamics of the suspension as a whole. As discussed in Koch and Subramanian (2011), particle-based models provide opportunities to (i) test continuum theories, (ii) analyze finite-size effects resulting from a discrete number of swimmers, (iii) explore more complex interactions between swimmers and/or boundaries, and in some cases, (iv) reveal the effects of short-range hydrodynamic interactions and/or steric repulsion. Various models have been proposed in this context, each using different approximations to address the difficult problems of resolving the hydrodynamic interactions and incorporating the geometry of the swimmers. Some of the first such models used point force distributions to create dumbbell-shaped swimmers (Hernandez-Ortiz et al. (2005, 2007)), slender-body theory to model a slip velocity along the surfaces of rod-like swimmers (Saintillan and Shelley (2007, 2012)), or the squirmer model (Lighthill (1952); Blake (1971)) to examine the interactions between spherical swimmers (Ishikawa et al. (2006)). These initial studies provided important fundamental results connecting the properties of the individual swimmers to the emergence of collective dynamics. Based on their success, these models have been more recently incorporated into a number of numerical approaches for suspension and fluid-structure interaction simulations including Stokesian dynamics (Ishikawa and Pedley (2007); Ishikawa et al. (2008); Mehandia and Nott (2008)), the immersed boundary method (Lushi and Peskin (2013); Lambert et al. (2013)), Lattice Boltzmann methods (Alarcón and Pagonabarraga (2013); Pagonabarraga and Llopis (2013)), distributed Lagrange-multiplier-based finite-volume methods (Li and Ardekani (2014)) and hybrid finite element/penalization schemes (Decoene et al. (2011)). This has allowed for both increased swimmer numbers as well as the incorporation of other effects such as steric interactions, external boundaries, and aligning torques.

In Chapter 6, we propose a methodology built on the FCM framework, and the squirmer model derived in Chapter 3, to simulate large active suspensions. We compare squirmer dynamics and kinematics with Boundary Element results. The very good agreement with the literature and the linear scaling of the code highlight the robustness of the method to accurately handle large collections of swimmers.

5.2 Brownian motion in particulate suspensions.

Brownian motion is the random motion exhibited by micron and sub-micron particles immersed in liquid. It is a fundamental mechanism for material and chemical transport in micron-scale physical and biological systems (Grima et al. (2010)), and can play a key role in determining the mechanical response of colloidal suspensions to applied stresses (Batchelor (1977); Bossis and Brady (1989); Foss and Brady (2000); Banchio and Brady (2003)). Brownian motion is also known to affect the aggregation and self-assembly of interacting particles (Anderson and Lekkerkerker (2002); Zaccarelli (2007); Lu et al. (2008)), a fundamental process important in many engineering applications that utilize colloidal particles to tune rheological properties of fluids (Mabille et al. (2000); ten Brinke et al. (2007)) and construct new materials and devices (Whitesides and Boncheva (2002); Glotzer et al. (2004); Promislow et al. (1995)). The rotational diffusivity, and therefore the motility, of micron-sized bacteria is strongly influenced by thermal agitation (Drescher et al. (2011)). Brownian motion also plays an important role in the transport and mixing properties of active systems (Leptos et al. (2009); Kurtuldu et al. (2011); Miño et al. (2013)). The diffusion of a colloid or a molecule in an active suspension depends on the intricate coupling between its Brownian diffusivity and the suspension dynamics (Kasyap et al. (2014)). To address the issue of enhanced Brownian particle diffusion in active suspensions one needs to include Brownian motion. More importantly, in the semi-dilute and concentrated regimes, the effect of hydrodynamic interactions is significant and particle rigidity constraints (i.e. stresslets) must be enforced. Therefore we need a tool which efficiently couples thermal fluctuations with an accurate description of hydrodynamic interactions within the same framework.

In Chapter 7 we detail all the technical difficulties arising when incorporating Brownian motion in particulate suspension and develop a new scheme, the Drifter-Corrector, which efficiently address these issues in the framework of the fluctuating force-coupling method (Keaveny (2014)).

Chapter 6

Modeling active suspensions with the force-coupling method.

Contents

6.1 Solving hydrodynamic interactions with the force-coupling method	84
6.1.1 FCM for passive suspensions	84
6.1.2 Squirmer interactions and motion	85
6.1.3 Notations	86
6.2 Numerical tools for High Performance Computing	86
6.2.1 Fluid solver	86
6.2.2 Computational work	86
6.2.3 Steric interactions	87
6.2.4 Algorithm	89
6.2.5 Including additional features	90
6.3 Validations	90
6.3.1 Interactions between a squirmer and an inert sphere	90
6.3.2 Trajectories of two interacting squirmers	90

This chapter presents a development of the force-coupling method (FCM) to address the accurate simulation of a large number of interacting micro-swimmers. Our approach is based on the squirmer model described in Chapter 3, which we adapt to the FCM framework in the context of High Performance Computing. First, we detail the parallel implementation of the method. Then the scalability of the code is evaluated and results for pairwise interactions are compared with the literature.

6.1 Solving hydrodynamic interactions with the force-coupling method

The FCM framework for particle suspensions is a straightforward extension of the isolated case presented in Section 3.1.1.

6.1.1 FCM for passive suspensions

Consider a suspension of N_p rigid spherical particles, each having radius a . Each particle n , ($n = 1, \dots, N_p$), is centered at \mathbf{Y}_n and subject to force \mathbf{F}^n and torque $\boldsymbol{\tau}^n$. To determine their motion through the surrounding fluid, we first represent each particle by a low order, finite-force multipole expansion in the Stokes equations

$$\begin{aligned}\nabla p - \eta \nabla^2 \mathbf{u} &= \sum_n \mathbf{F}^n \Delta_n(\mathbf{x}) + \frac{1}{2} \boldsymbol{\tau}^n \times \nabla \Theta_n(\mathbf{x}) + \mathbf{S}^n \cdot \nabla \Theta_n(\mathbf{x}) \\ \nabla \cdot \mathbf{u} &= 0.\end{aligned}\tag{6.1}$$

In Eq. (6.1), \mathbf{S}^n are the particle stresslets determined through a constraint on the local rate-of-strain as described below. Also in Eq. (6.1) are the two Gaussian envelopes,

$$\begin{aligned}\Delta_n(\mathbf{x}) &= (2\pi\sigma_\Delta^2)^{-3/2} e^{-|\mathbf{x}-\mathbf{Y}^n|^2/2\sigma_\Delta^2} \\ \Theta_n(\mathbf{x}) &= (2\pi\sigma_\Theta^2)^{-3/2} e^{-|\mathbf{x}-\mathbf{Y}^n|^2/2\sigma_\Theta^2},\end{aligned}\tag{6.2}$$

used to project the particle forces onto the fluid.

Contrary to the isolated case, no analytical solution can be derived for the fluid flow \mathbf{u} . A numerical solver is thus necessary. It could be of any type. In Section 6.2.1 we provide more details about the fluid solver we use throughout the thesis.

After solving Eq. (6.1), the velocity, \mathbf{V}_n , angular velocity, $\boldsymbol{\Omega}_n$, and local rate-of-strain, \mathbf{E}_n , of each particle n are found by volume averaging of the resulting fluid flow,

$$\mathbf{V}^n = \int \mathbf{u} \Delta_n(\mathbf{x}) d^3 \mathbf{x}\tag{6.3}$$

$$\boldsymbol{\Omega}^n = \frac{1}{2} \int [\nabla \times \mathbf{u}] \Theta_n(\mathbf{x}) d^3 \mathbf{x},\tag{6.4}$$

$$\mathbf{E}^n = \frac{1}{2} \int [\nabla \mathbf{u} + (\nabla \mathbf{u})^T] \Theta_n(\mathbf{x}) d^3 \mathbf{x},\tag{6.5}$$

where the integration is performed over \mathbb{R}^3 . In order for Eqs. (6.3) – (6.5) to recover the correct mobility relations for a single, isolated sphere, namely that $\mathbf{V} = \mathbf{F}/(6\pi a\eta)$ and $\boldsymbol{\Omega} = \boldsymbol{\tau}/(8\pi a^3\eta)$, the envelope length scales need to be $\sigma_\Delta = a/\sqrt{\pi}$ and $\sigma_\Theta = a/(6\sqrt{\pi})^{1/3}$. As the particles are rigid, the stresslets are found by enforcing the constraint that $\mathbf{E}^n = \mathbf{0}$ for each particle n (Lomholt and Maxey (2003)).

6.1.2 Squirmer interactions and motion

Using FCM, the task of computing the interactions between squirmers is relatively straightforward. We now consider N_p independent squirmers with positions \mathbf{Y}^n and orientations \mathbf{p}^n . Each squirmer has swimming dipole

$$\mathbf{G}^n = \frac{4}{3}\pi\eta a^2 (3\mathbf{p}^n\mathbf{p}^n - \mathbf{I}) B_2, \quad (6.6)$$

and degenerate quadrupole

$$\mathbf{H}^n = -\frac{4}{3}\pi\eta a^3 B_1 \mathbf{p}^n. \quad (6.7)$$

The squirmers may also be subject to external forces \mathbf{F}^n and torques $\boldsymbol{\tau}^n$. Using the linearity of the Stokes equations we obtain

$$\begin{aligned} \nabla p - \eta \nabla^2 \mathbf{u} &= \sum_n \mathbf{F}^n \Delta_n(\mathbf{x}) + \frac{1}{2} \boldsymbol{\tau}^n \times \nabla \Theta_n(\mathbf{x}) + \mathbf{S}^n \cdot \nabla \Theta_n(\mathbf{x}) \\ &\quad + \mathbf{G}^n \cdot \nabla \Delta_n(\mathbf{x}) + \mathbf{H}^n \nabla^2 \Theta_n(\mathbf{x}) \end{aligned} \quad (6.8)$$

$$\nabla \cdot \mathbf{u} = 0 \quad (6.9)$$

for the flow field generated by the suspension.

After finding the flow field, we determine the motion of the squirmers using Eqs. (6.3) – (6.5) with two modifications. First, we need to add the swimming velocity, $U\mathbf{p}^n$, to Eq. (6.3). Second, we must subtract the artificial, self-induced velocity and the local rate-of-strain due to the squirming modes. The self-induced velocity is given by

$$\mathbf{W}^n = \int \mathbf{A} \cdot \mathbf{H}^n \Delta(\mathbf{x}) d^3 \mathbf{x} \quad (6.10)$$

where the tensor \mathbf{A} is given in Eq. (3.23).

The self-induced rate-of-strain is given by

$$\mathbf{K}^n = \int \frac{1}{2} (\nabla \mathbf{R} \cdot \mathbf{G}^n + (\nabla \mathbf{R} \cdot \mathbf{G}^n)^T) \Theta(\mathbf{x}) d^3 \mathbf{x} \quad (6.11)$$

where the expression for the third rank tensor \mathbf{R} can be found in Eq. (3.24).

Taking these self-induced effects into account, the motion of a squirmer n is given by

$$\mathbf{V}^n = U\mathbf{p}^n - \mathbf{W}^n + \int \mathbf{u} \Delta_n(\mathbf{x}) d^3 \mathbf{x} \quad (6.12)$$

$$\boldsymbol{\Omega}^n = \frac{1}{2} \int [\nabla \times \mathbf{u}] \Theta_n(\mathbf{x}) d^3 \mathbf{x} \quad (6.13)$$

$$\mathbf{E}^n = -\mathbf{K}^n + \frac{1}{2} \int [\nabla \mathbf{u} + (\nabla \mathbf{u})^T] \Theta_n(\mathbf{x}) d^3 \mathbf{x}. \quad (6.14)$$

As for passive particles, the stresslets \mathbf{S}^n due to squirmer rigidity are obtained from the usual constraint on the local rate-of-strain, namely $\mathbf{E}^n = \mathbf{0}$ for all n . Squirmer positions \mathbf{Y}^n and orientations \mathbf{p}^n are then updated with the Lagrangian equations

$$\frac{d\mathbf{Y}^n}{dt} = \mathbf{V}^n, \quad (6.15)$$

$$\frac{d\mathbf{p}^n}{dt} = \boldsymbol{\Omega}^n \times \mathbf{p}^n. \quad (6.16)$$

In Section 6.3, we show through a comparison with the boundary element simulations from [Ishikawa et al. \(2006\)](#) that our FCM squirmer model recovers the velocities, angular velocities, stresslets (\mathbf{S}^n) and trajectories for two interacting squirmers for a wide range of separations.

6.1.3 Notations

In the following, we denote \mathcal{Y} , \mathcal{P} , \mathcal{V} and \mathcal{W} the $3N_p$ vectors containing the particle positions, orientations, translational and rotational velocities. \mathcal{E} and \mathcal{S} are $6N_p$ and contain the particle rate-of-strains and stresslets respectively. \mathcal{F} , \mathcal{T} are the $3N_p$ forces and torques. \mathcal{H} is a $3N_p$ vector containing the degenerate quadrupoles and \mathcal{G} is $6N_p$ vector containing the swimming stresslets.

6.2 Numerical tools for High Performance Computing

6.2.1 Fluid solver

The smoothness of the Gaussian force distributions allows FCM to be used with a variety of numerical methods to discretize the Stokes equations. It has been implemented with spectral and spectral element methods ([Pivkin et al. \(2006\)](#); [Liu et al. \(2009\)](#); [Yeo and Maxey \(2010b\)](#)) and finite volume methods ([Loisel et al. \(2013\)](#); [Agbangla et al. \(2014\)](#)) in both simple and complex domain geometries.

Here, we use a Fourier spectral method with Fast Fourier Transforms (FFTs) to solve the Stokes equations, Eqs. (6.8) – (6.9), for the fluid flow in a three-dimensional periodic domain. The FFTs are parallelized with the MPI library P3DFFT. This library uses 2D decomposition of the 3D domain, introducing a better scalability than FFT libraries that implement a 1D decomposition. This decomposition has shown good scalability up to $N_c = 32,768$ cores in Direct Numerical Simulation (DNS) of turbulence ([Pekurovsky \(2012\)](#)).

6.2.2 Computational work

As explained in [Yeo and Maxey \(2010b\)](#), the number of floating point operations for FCM scales linearly with the number of particles, N_p . We find the same scaling for our implementation of FCM. Figure 6.1 shows the computational time per time-step for N_p up to 75,000 particles with $384^3 \sim 6 \cdot 10^7$ grid points and $N_c = 256$ cores.

Note that the slope is less than one even in the concentrated regime ($\phi_v > 0.1$). Figure 6.2 provide a visualization of a concentrated suspension ($\phi_v = 0.2$) containing 75,000 swimmers.

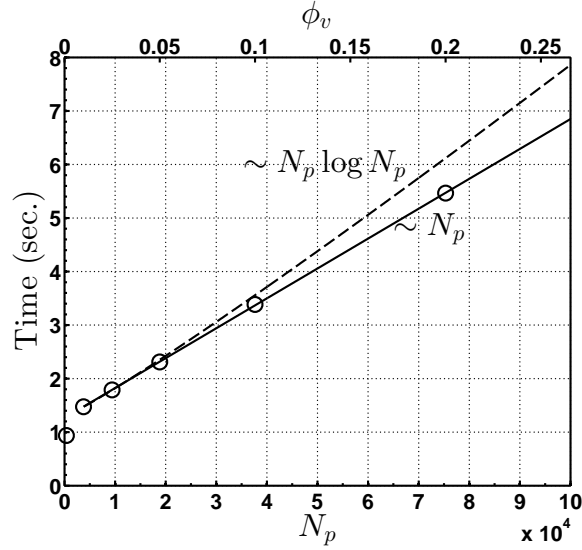


Figure 6.1: Scaling of the FCM with the number of squirmers N_p . Computational time per time-step versus N_p , or equivalently, versus volumetric fraction ϕ_v . $N_c = 256$ cores work in parallel for a cubic domain with 384^3 grid points.

6.2.3 Steric interactions

Including steric repulsion is straightforward with FCM. These forces are introduced to both prevent particles from overlapping during the finite time-step and to account for contact forces. For spherical particles, we use the steric barrier described in [Dance et al. \(2004\)](#). For particles n and m , let $\mathbf{r}_{nm} = \mathbf{Y}^m - \mathbf{Y}^n$ and $r_{nm} = \|\mathbf{r}_{nm}\|$. The repulsive force experienced by n due to steric interactions is

$$\mathbf{F}_b^n = \begin{cases} -\frac{F_{\text{ref}}}{2a} \left[\frac{R_{\text{ref}}^2 - r_{nm}^2}{R_{\text{ref}}^2 - 4a^2} \right]^{2\gamma} \mathbf{r}_{nm}, & \text{for } r_{nm} < R_{\text{ref}}, \\ 0, & \text{otherwise.} \end{cases} \quad (6.17)$$

where F_{ref} is the magnitude of the force, the cut-off distance R_{ref} sets the distance over which the force acts, and the exponent γ can be adjusted to control the stiffness of the force. Unless specified, all the simulations are run with $F_{\text{ref}}/6\pi\eta aU = 4$, $R_{\text{ref}} = 2.2a$ and $\gamma = 2$. From Newton's third law, we obtain $\mathbf{F}_b^m = -\mathbf{F}_b^n$. For spheroidal particles, steric forces and torques can be introduced by using a similar soft repulsive potential with the surface-to-surface distance approximated by the Berne-Pechukas range parameter ([Allen and Germano \(2006\)](#)).

Using a direct pairwise calculation, the evaluation of steric interactions between all particle pairs at each time step would require $O(N_p^2/(2N_c))$ computations per core. This cost is much greater than the $O(N_p)$ cost of the hydrodynamic aspects of FCM. Therefore, instead of a direct calculation, we use the linked-list algorithm described in [Allen et al. \(1987\)](#). This method divides the computational domain into smaller sub-domains into

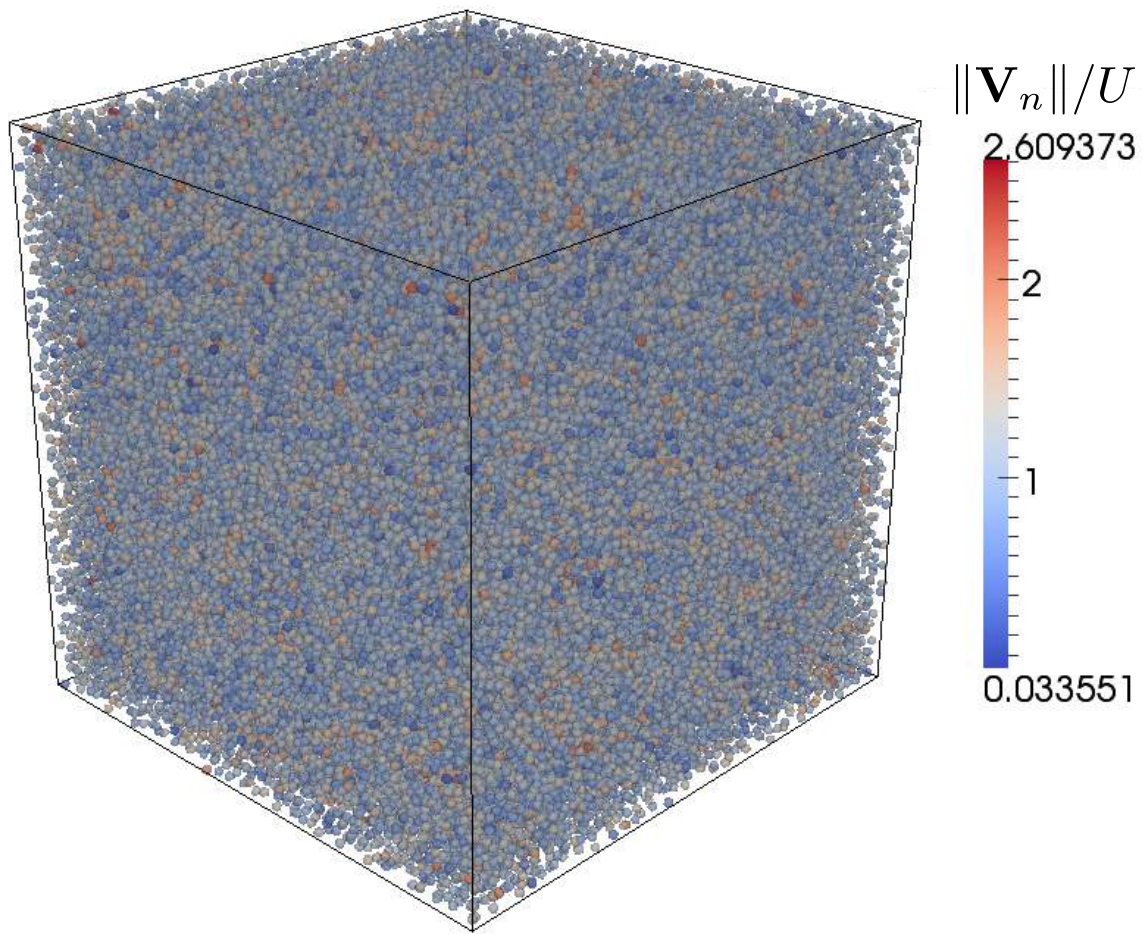


Figure 6.2: Snapshot of a concentrated suspension ($\phi_v = 0.2$) containing $N_p = 75,000$ squirmers. Micro-swimmers are colored with the norm of their velocity \mathbf{V}^n , $n = 1, N_p$, normalized by the intrinsic swimming speed U .

which the particles are sorted. The edge-length of each sub-domain is slightly larger than R_{ref} . These sub-domains are distributed over the cores where the steric interactions are evaluated. For a homogeneous suspension, this results in a per core cost for steric interactions that is $O(14N_p^2/(2N_cN_s))$, where N_s is the total number of sub-domains. Since for large system sizes, we have $N_s \approx L^3/R_{\text{ref}}^3 \gg 14$ and $N_c \gg 1$, the linked-list algorithm for steric interactions is much more efficient than the direct computation.

Alternatively, collisions can be handled kinematically. [Maury \(2006\)](#) developed an efficient method to prevent particle overlapping without having to resort to contact forces. This method has been used for the modeling of crowd motion ([Maury and Venel \(2011\)](#); [Maury \(2014\)](#)), granular media ([Faure et al. \(2009\)](#)), passive and active suspensions ([Lefebvre \(2009\)](#); [Decoene et al. \(2011\)](#)). Its parallel implementation in the code SCoPI¹, provides a good framework for the simulation of large collections of objects. I performed a numerical study to evaluate the pros and cons in using this method in our simulations. Appendix B contains the details and suggests further improvements.

6.2.4 Algorithm

We summarize the overall procedure to simulate large populations of microswimmers in Stokes flow with the FCM:

- Initialize particle positions \mathcal{Y}^0 and orientations \mathcal{P}^0 ,
- Time loop on index k
 1. Compute Gaussians $\Delta_n^k(\mathbf{x})$ and $\Theta_n^k(\mathbf{x})$, Eq. (6.2),
 2. Update swimming multipoles \mathcal{G}^k , Eq. (3.15), and \mathcal{H}^k , Eq. (3.18), which both depend on \mathcal{P}^k ,
 3. Compute steric interactions, Eq. (6.17), with the linked-list algorithm,
 4. Add additional forcing if any (gyrotactic torques, magnetic dipoles,...),
 5. Project the Gaussian distributions onto the grid (RHS of Eq. (6.9)),
 6. Solve Stokes equations, Eqs. (6.8) – (6.9), to obtain the fluid velocity field $\mathbf{u}^k(\mathbf{x})$,
 7. Compute particle rate of strains \mathcal{E}^k , Eq. (6.14),
 8. If $\|\mathcal{E}^k\| > \varepsilon$, compute stresslets \mathcal{S}^k following [Yeo and Maxey \(2010b\)](#),
 - (a) Project all the multipoles onto the grid (RHS of Eq. (6.9)),
 - (b) Solve for Stokes equations, Eqs. (6.8) – (6.9), to obtain the fluid velocity field $\mathbf{u}^k(\mathbf{x})$,
 9. Compute particle velocities \mathcal{V}^k , Eq. (6.12), and rotations \mathcal{W}^k , Eq. (6.13),
 10. Integrate Eqs. (6.15) and (6.16) using the fourth-order Adams-Bashforth scheme to obtain \mathcal{Y}^{k+1} and \mathcal{P}^{k+1} .

¹<http://www.cmap.polytechnique.fr/~lefebvre/SCoPI.htm>

6.2.5 Including additional features

With FCM, additional effects can readily be incorporated into the squirmer model and in our subsequent simulations, we consider several of them to demonstrate the versatility of our approach. We can extend the FCM squirmer model to ellipsoidal shapes by using the ellipsoidal FCM Gaussian distributions. Such a model can be carefully tuned by comparing with results from Kanevsky et al. (2010) and Leshansky et al. (2007). The effects of particle aspect ratio on suspension properties can then be explored systematically while still accounting for particle size effects such as Jeffery orbits.

As shown in Chapter 3, we are not limited to constant values for B_1 and B_2 . By allowing these parameters to be functions of time, the FCM squirmer model can be used to explore how the swimmers' strokes affect overall suspension dynamics. These extensions to active suspensions are addressed in Section 10.2.

6.3 Validations

In Ishikawa et al. (2006), the authors performed a variety of simulations using the Boundary Element Method (BEM) to compute to high accuracy the pairwise interactions between a squirmer and an inert sphere, and between two squirmers. Here, we consider the same scenarios as those authors and compare results from our FCM simulations with their BEM results.

6.3.1 Interactions between a squirmer and an inert sphere

We first consider the interactions between an inert sphere (labelled “2”) located at a point \mathbf{r} from the center of a puller squirmer (labelled “1”) with $\beta = 5$. The direction \mathbf{r}/r forms the angle θ with the swimming direction \mathbf{p} of the squirmer. The problem setup is depicted in Figure 6.3.

Figure 6.4 compares the velocity of the sphere obtained using FCM simulations with the BEM results and far-field analytical solutions from Ishikawa et al. (2006). As FCM also resolves the mutually induced particle stresslets, it provides a more accurate estimation than far-field approximation of Ishikawa et al. (2006). As a result, we see that the FCM results very closely match BEM, even in the range where $r/a < 3$. Similar trends are observed for the angular velocity of the inert sphere (Figure 6.4b) and the stresslet components (Figure 6.4c, 6.4d). These comparisons illustrate the accuracy of the results that can be obtained using FCM, which closely matches BEM but incurs a fraction of the computational cost.

6.3.2 Trajectories of two interacting squirmers

We compute the trajectories of two puller squirmers ($\beta = 5$) and compare the results with the BEM simulations of Ishikawa et al. (2006). One squirmer initially swims in the x -direction, $\mathbf{p}^1 = \mathbf{e}_x$, and the other one in the opposite direction, $\mathbf{p}^2 = -\mathbf{e}_x$. They are placed with initial separation distance $\delta y = 1a, \dots, 10a$ in the transverse direction and

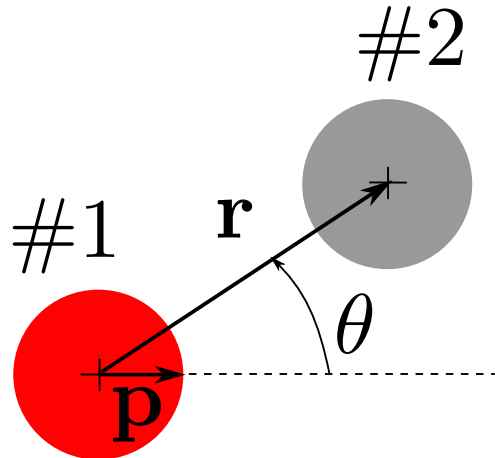


Figure 6.3: Sketch showing the set-up of our computations of the interactions between squirmer “1” and inert sphere “2”.

	R_{ref}/a	$F_{\text{ref}}/6\pi\eta aU$	Exponent γ
----	2.2	4	2
.....	2.4	6	1
—	3	3	5
-.-.-	2.04	5	5

Table 6.1: Parameters for the contact forces on Figure 6.7b

$\delta x = 10a$ in the x -direction. The problem set-up is depicted in Figure 6.5. Since the squirmers may collide, we also include steric interactions provided by the force barrier (6.17).

As shown in Figure 6.6, the trajectories match very well with the BEM results for $\delta y \geq 2a$. When $\delta y = 1a$, the collision barrier and near-field hydrodynamic interactions play an important role in determining the overall squirmer trajectories. Figure 6.7 shows the effect of the steric repulsion parameters F_{ref} and R_{ref} on the squirmer trajectories. The specific values of these parameters are provided in Table 6.1. We see that by varying the barrier parameters one can obtain trajectories that closely match the results of Ishikawa et al. (2006).

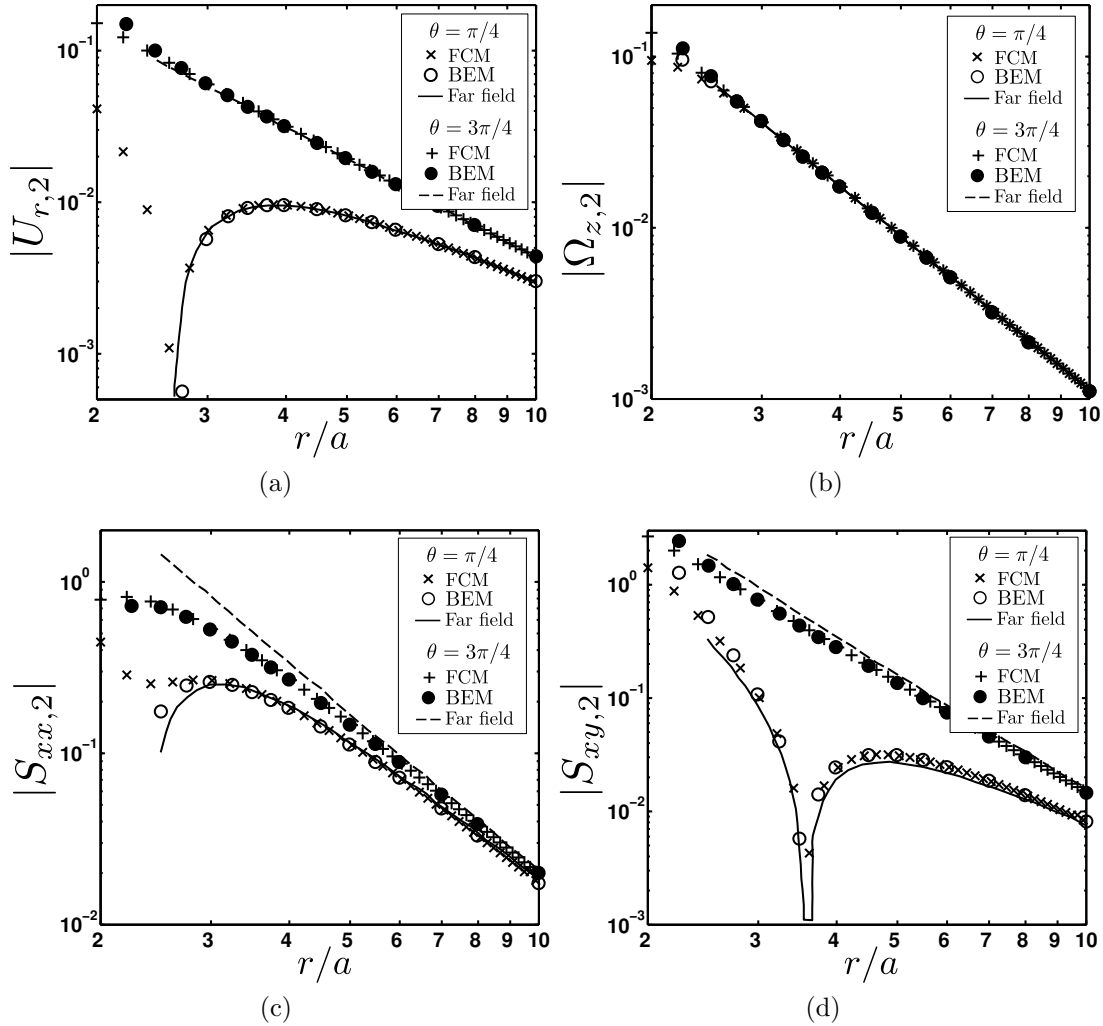


Figure 6.4: The (a) Radial velocity $|U_{r,2}|$, (b) Angular velocity $|\Omega_{z,2}|$, (c) Stresslet component $|S_{xx,2}|$, and (d) Stresslet component $|S_{xy,2}|$ for the inert sphere “2” at a distance r from a puller squirmer ($\beta = 5$).

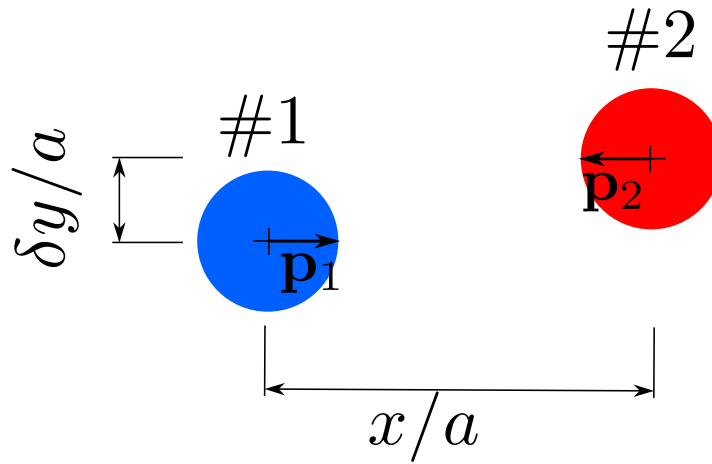


Figure 6.5: Initial configuration of the squirmers in the trajectory simulations.

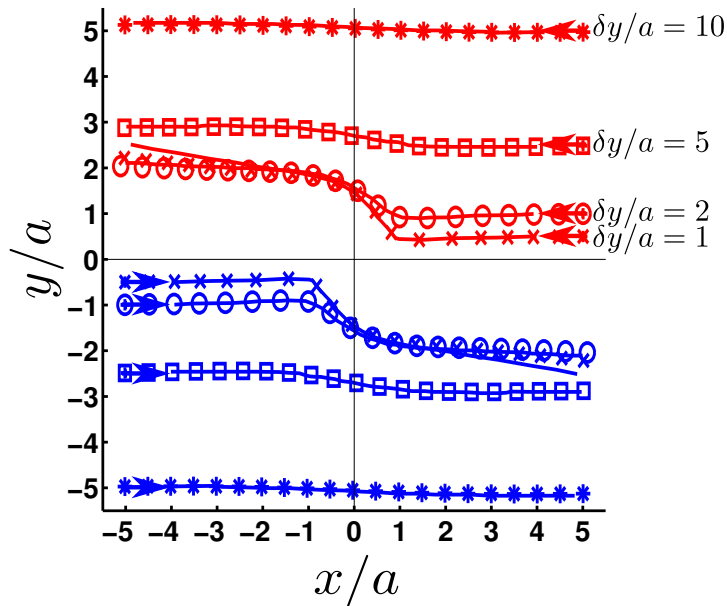


Figure 6.6: Trajectories of two squirmers swimming in opposite directions with transverse initial distance $\delta y = 1a, \dots, 10a$. Lines: data from Ishikawa et al. (2006). Symbols: FCM results.

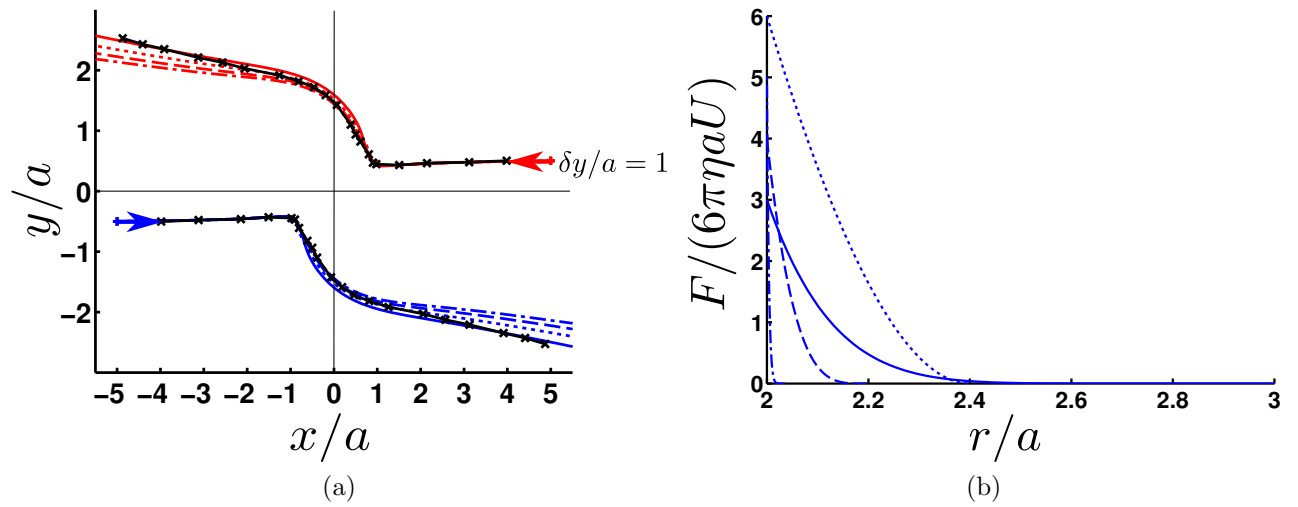


Figure 6.7: Influence of the collision barrier parameters on the squirmer trajectories for the case where initially $\delta y = 1a$. (a) Trajectories. Crosses: data from [Ishikawa et al. \(2006\)](#). (b) Force barrier profiles. The line styles correspond those showing the trajectories in a).
 - - - : barrier used in [Figure 6.6](#).

Chapter 7

Time integration for particle Brownian motion determined through fluctuating hydrodynamics

Contents

7.1	Introduction	96
7.2	Equations of motion	98
7.3	Fluctuating FCM	99
7.3.1	Mobility matrices and the fluctuation dissipation theorem	101
7.4	Time integration	103
7.4.1	Fixman's method	104
7.4.2	Random Finite Differencing	105
7.4.3	Drifter-Corrector	106
7.5	Numerical studies	108
7.5.1	Spatial discretization	108
7.5.2	Brownian dynamics between two slip surfaces	109
7.5.3	Colloidal gelation and percolation	117
7.6	Conclusions	123

Remark: *The content of this chapter is directly extracted from an eponymous paper written with Pr. Eric Keaveny.*

Fluctuating hydrodynamics has been successfully combined with several computational methods to rapidly compute the correlated random velocities of Brownian particles. In the overdamped limit where both particle and fluid inertia are ignored, one must also account for a Brownian drift term in order to successfully update the particle positions. In this paper, we introduce and study a midpoint time integration scheme we refer to as the drifter-corrector (DC) that resolves the drift term for fluctuating hydrodynamics-based

methods even when constraints are imposed on the fluid flow to obtain higher-order corrections to the particle hydrodynamic interactions. We explore this scheme in the context of the fluctuating force-coupling method (FCM) where the constraint is imposed on the rate-of-strain averaged over the volume occupied by the particle. For the DC, the constraint need only be imposed once per time step, leading to a significant reduction in computational cost with respect to other schemes. In fact, for fluctuating FCM, the DC reduces the total additional cost of including Brownian motion to just a single flow solve per time-step. By performing a series of simulations, we show that the DC is effective in both reproducing the equilibrium distribution and the evolution of particulate suspensions. In addition, we demonstrate that fluctuating FCM coupled with the DC provides an efficient and accurate method for large-scale dynamic simulation of colloidal dispersions and the study of processes such as colloidal gelation.

7.1 Introduction

While Brownian motion is clearly important in many situations, the careful study and quantification of its role using simulation remains a computational challenge due to the intimate link between the random motion of the particles and their many-body hydrodynamic interactions.

In order to achieve the correct equilibrium distribution, the statistics of the random particle motion must satisfy the fluctuation-dissipation theorem (Kubo (1966)) which states that the random particle velocity correlations must be proportional to the hydrodynamic mobility matrix. In simulation, this would require the square root of the mobility matrix to be found at each time step to compute the correct particle velocities. As a result, the inclusion of Brownian motion has often limited simulations to having very small particle numbers, or ignoring completely hydrodynamic interactions between the particles. Though several methods have been introduced to accelerate the matrix square root computation (Fixman (1986); Ando et al. (2012, 2013)), recent studies have shown this computation can be avoided altogether using fluctuating hydrodynamics.

Fluctuating hydrodynamics involves generating random fluid flows by including a white-noise fluctuating stress in the equations of fluid motion. Introduced in the first edition of Landau and Lifshitz (Landau and Lifshitz (1959)), its effectiveness for yielding the correct random motion of particles was demonstrated in a number of theoretical studies in the 1960s and 1970s (Fox and Uhlenbeck (1970); ?). As a result of this fundamental work, fluctuating hydrodynamics has found success in numerical simulations of micron-scale fluid-structure interactions in methods such as Lattice-Boltzmann (Ladd (1993, 1994b,a)), hybrid Eulerian-Lagrangian approaches for point particles (Usabiaga et al. (2013); Usabiaga and Delgado-Buscalioni (2013)), distributed Lagrange-multiplier method (Sharma and Patankar (2004)), finite-element simulation (Plunkett et al. (2014)), the stochastic and fluctuating immersed-boundary methods (IBM) (Atzberger et al. (2007); Atzberger (2011); Usabiaga et al. (2014); DeLong et al. (2014)), and the fluctuating force-coupling method (FCM) (Keaveny (2014)). IBM and FCM are similar in that they both use projection and volume averaging operations to first transfer the forces experienced by the

particles to the fluid, and subsequently, extract the motion of the particle phase from the motion of the fluid. To resolve Brownian motion, the volume averaging operators can be used to obtain the random motion of the particles from the fluctuating flow field. As the fluctuating stress is based on spatially uncorrelated white-noise, the matrix square root computation does not have to be performed. For the stochastic and fluctuating IBMs and fluctuating FCM, it has been shown (Atzberger et al. (2007); Atzberger (2011); Keaveny (2014); DeLong et al. (2014)) explicitly that the resulting particle velocity correlations satisfy the fluctuation-dissipation theorem.

While the usage of fluctuating hydrodynamics has accelerated the computation of the random particle velocities, in the overdamped, or Brownian dynamics limit where one can ignore both fluid and particle inertia, a seemingly-problematic Brownian drift term proportional to the divergence of the particle mobility matrix also needs to be accounted for. Fixman (Fixman (1978); Grassia et al. (1995)) showed that the effects of the drift term can be recovered without a direct computation by using a specific mid-point time integration scheme. This approach, however, relies on the usage of random forces and torques, rather than random velocities and angular velocities, making its implementation with the stochastic and fluctuating IBMs and fluctuating FCM rather cumbersome and computationally expensive (Keaveny (2014)). To overcome this difficulty, DeLong et al. (2014) proposed an integration scheme using what they termed as random finite differencing (RFD). By randomly displacing and forcing the particles in a particular way, the divergence of the mobility matrix is recovered without ever needing to perform the onerous computations involved with Fixman’s method.

The purpose of our study is to further accelerate time integration for fluctuating hydrodynamics-based simulations of Brownian particles. We give particular interest to the case where these computations involve constraining the flow to generate higher-order corrections to the particle hydrodynamic interactions, for which RFD still incurs a significant computational cost. To this end, we develop a midpoint time integration scheme that we refer to as the drifter-corrector (DC) that requires the constraints be applied only once per timestep, leading to the desired reduction in computational cost. In fact, we show that when the DC is used in conjunction with fluctuating FCM, a Brownian simulation requires just a single additional Stokes solve per timestep as compared to a deterministic FCM simulation of the same system. We provide an extensive validation of the DC by performing fluctuating FCM simulations of a single particle between two slip surfaces. We show how to impose these boundary conditions with fluctuating hydrodynamics by modifying the spatial correlations of the fluctuating stress, rather than imposing it directly through the Stokes solver. This validation confirms our theoretical analysis of the scheme and shows that the DC is able to yield both the correct equilibrium distribution and the correct distribution dynamics described by the Smoluchowski equation. We consider the canonical problem of a collapsing cluster of interacting colloidal particles, allowing for comparison with results given by other methodologies and the demonstration that the higher-order stresslet corrections resolved in fluctuating FCM yield quantitative differences in the results. We show that, by avoiding two additional stresslet iteration, the DC yields a computational cost three times smaller than central RFD. Finally, using the DC with fluctuation FCM, we also perform simulations of suspensions of interacting

Brownian particles to explore colloidal gelation and percolated network formation. We show that in addition to reproducing the results of other simulation techniques such as Stokesian dynamics, fluctuating FCM with the DC allows for larger scale simulation of hydrodynamically interacting Brownian particles at a lower computational cost.

7.2 Equations of motion

In this study, we will be considering a suspension of N_p spherical Brownian particles, each having radius a . The position of particle n is denoted by \mathbf{Y}^n . Each particle may also be subject to non-hydrodynamic forces, \mathbf{F}^n , and torques, $\boldsymbol{\tau}^n$. In the overdamped or Brownian dynamics limit, where both fluid and particle inertia are negligible (Ermak and McCammon (1978); Brady (1988)), the dynamics of the particles is described by the system of stochastic differential equations

$$d\mathcal{Y} = (\mathcal{M}^{\nu\mathcal{F}}\mathcal{F} + \mathcal{M}^{\nu\mathcal{T}}\mathcal{T}) dt + k_B T \nabla_{\mathcal{Y}} \cdot \mathcal{M}^{\nu\mathcal{F}} dt + d\tilde{\mathcal{V}} \quad (7.1)$$

where \mathcal{Y} is the $3N_p \times 1$ vector that contains the position information for all particles, \mathcal{F} is the $3N_p \times 1$ vector of forces on all of the particles, and \mathcal{T} is the similar vector for the torques. The vector $d\tilde{\mathcal{V}}$ is the incremental random velocity which, along with the incremental angular velocity, $d\tilde{\mathcal{W}}$, is related to the incremental $6N_p \times 1$ Wiener process, $d\mathcal{B}$, through

$$\begin{bmatrix} d\tilde{\mathcal{V}} \\ d\tilde{\mathcal{W}} \end{bmatrix} = \sqrt{2k_B T} \mathcal{M}^{1/2} d\mathcal{B} \quad (7.2)$$

where k_B is Boltzmann's constant and T is the temperature. Appearing also in Eqs. (7.1) and (7.2) is the $6N_p \times 6N_p$ hydrodynamic mobility matrix

$$\mathcal{M} = \begin{bmatrix} \mathcal{M}^{\nu\mathcal{F}} & \mathcal{M}^{\nu\mathcal{T}} \\ \mathcal{M}^{\omega\mathcal{F}} & \mathcal{M}^{\omega\mathcal{T}} \end{bmatrix}, \quad (7.3)$$

as well as its submatrices $\mathcal{M}^{\nu\mathcal{F}}$ and $\mathcal{M}^{\nu\mathcal{T}}$. The mobility matrix, which in general depends on the particle positions, provides the linear relationship between the forces and torques on the particles and their resulting velocities and angular velocities. All the information about how the particles interact through the fluid is contained in the mobility matrix. The mobility matrix is determined by solving the Stokes equations,

$$\begin{aligned} \nabla p - \eta \nabla^2 \mathbf{u} &= \mathbf{0} \\ \nabla \cdot \mathbf{u} &= 0 \end{aligned} \quad (7.4)$$

that govern the flow induced in the surrounding fluid as the particles move through it. For methods such as Brownian or Stokesian dynamics, the mobility matrix is constructed using the flow generated by a force multipole expansion in the Stokes equations and Faxén laws (Happel and Brenner (2012); Kim and Karrila (1991b)) to extract the particle motion from

the fluid velocity. In this paper, we adopt an alternative, but parallel approach known as the force-coupling method (Maxey and Patel (2001); Lomholt and Maxey (2003)) (FCM) that utilizes regularized, rather than singular, force distributions in the Stokes equations and replaces the Faxén laws by volume averaging operators. As noted by Delong et al. (2014), this approach and the immersed boundary method share similar features and have distinct advantages over methods based on singular force distributions, particularly when Brownian motion is included in the simulation.

In the absence of Brownian motion, only the first term in Eq. (7.1), the mobility matrix multiplied by the forces and torques, will be non-zero. The inclusion of Brownian motion gives rise to the two additional terms – the incremental random velocity, $d\tilde{\mathcal{V}}$, as well as an additional drift known as Brownian drift. To satisfy the fluctuation-dissipation theorem, $d\tilde{\mathcal{V}}$ depends on the square root of the mobility matrix through Eq. (7.2). This links the random motion of the particles with how they interact through the fluid. As we discuss in the next section, we can compute this term rather efficiently by volume averaging and constraining the fluid flow generated by a white-noise fluctuating stress. The Brownian drift term has a more subtle origin. It arises as a result of taking the overdamped limit of the Langevin dynamics where particle inertia is present (Ermak and McCammon (1978); Atzberger (2011)). In order to successfully ignore the suspension dynamics during the short inertial relaxation timescale, one must include the Brownian drift term to obtain an SDE that is consistent with Smoluchowski’s equation (Ermak and McCammon (1978)). The purpose of this work is to introduce new and study existing (Fixman (1978); Grassia et al. (1995); Delong et al. (2014)) time integration schemes that automatically account for Brownian drift. We pay particular attention to the case where the higher-order correction to the particle mobility matrix is obtained by imposing a local rate-of-strain constraint on the flow. We show that for methods employing fluctuating hydrodynamics, the Brownian drift can be accounted for at the cost of a single additional Stokes solve per timestep by using an appropriately designed time integration scheme.

7.3 Fluctuating FCM

To compute the terms in Eq. (7.1) that depend on the mobility matrix, we utilize fluctuating FCM that is described and analyzed in detail in our previous work (Keaveny (2014)). Fluctuating FCM combines FCM (Maxey and Patel (2001); Lomholt and Maxey (2003)) with fluctuating hydrodynamics resulting in an efficient methodology to determine particle hydrodynamic interactions while simultaneously yielding the correct random particle velocities that satisfy the fluctuation-dissipation theorem. In fluctuating FCM, the fluid velocity is given by the Stokes equations driven by a white-noise fluctuating stress, and a low-order, regularized multipole expansion representing the force the particles exert on the fluid. The motion of the particles is then found by taking volume averages of the fluid velocity. This process is similar to that of the stochastic and fluctuating IBMs, and as we demonstrate below, fluctuating FCM can be expressed in terms of projection, or spreading, operators and volume averaging, or interpolation, operators commonly used to describe IBM. We present fluctuating FCM using this framework to emphasize the

connection between the methodologies, indicating that the time integration schemes that we explore using fluctuating FCM in subsequent sections could also be used more widely.

For fluctuating FCM, the fluid velocity is given by the following Stokes flow

$$\begin{aligned}\nabla p - \eta \nabla^2 \mathbf{u} &= \nabla \cdot \mathbf{P} + \mathcal{J}^\dagger[\mathcal{F}] + \mathcal{N}^\dagger[\mathcal{T}] + \mathcal{K}^\dagger[\mathcal{S}] \\ \nabla \cdot \mathbf{u} &= 0,\end{aligned}\tag{7.5}$$

$$\mathcal{K}[\mathbf{u}] = \mathbf{0},\tag{7.6}$$

where the fluctuating stress, \mathbf{P} , has the following statistics

$$\langle P_{ij}(\mathbf{x}) \rangle = 0\tag{7.7}$$

$$\langle P_{ij}(\mathbf{x}) P_{kl}(\mathbf{y}) \rangle = 2k_B T (\delta_{ik} \delta_{jl} + \delta_{il} \delta_{jk}) \delta(\mathbf{x} - \mathbf{y})\tag{7.8}$$

with $\langle \cdot \rangle$ denoting the ensemble average of a quantity.

The non-hydrodynamic forces, \mathcal{F} , and torques, \mathcal{T} , on the particles, as well as the particle stresslets, \mathcal{S} , the symmetric force-moment on each particle, are projected onto the fluid using the linear operators \mathcal{J}^\dagger , \mathcal{N}^\dagger , and \mathcal{K}^\dagger which are given by

$$\mathcal{J}^\dagger[\mathcal{F}] = \sum_n \mathbf{F}^n \Delta_n(\mathbf{x})\tag{7.9}$$

$$\mathcal{N}^\dagger[\mathcal{T}] = -\frac{1}{2} \sum_n \boldsymbol{\tau}^n \times \nabla \Theta_n(\mathbf{x})\tag{7.10}$$

$$\mathcal{K}^\dagger[\mathcal{S}] = \frac{1}{2} \sum_n \mathbf{S}^n \cdot \left(\nabla \Theta_n(\mathbf{x}) + (\nabla \Theta_n(\mathbf{x}))^T \right).\tag{7.11}$$

Appearing in these expressions are the two Gaussian envelopes, or spreading functions,

$$\Delta_n(\mathbf{x}) = (2\pi\sigma_\Delta^2)^{-3/2} e^{-|\mathbf{x} - \mathbf{Y}^n|^2 / 2\sigma_\Delta^2}\tag{7.12}$$

$$\Theta_n(\mathbf{x}) = (2\pi\sigma_\Theta^2)^{-3/2} e^{-|\mathbf{x} - \mathbf{Y}^n|^2 / 2\sigma_\Theta^2}\tag{7.13}$$

where σ_Δ and σ_Θ are related to the radius of the particles through $\sigma_\Delta = a/\sqrt{\pi}$ and $\sigma_\Theta = a/(6\sqrt{\pi})^{1/3}$. Unlike the forces and torques which are typically set by external or inter-particle potentials, the stresslets arise as a result of the constraint on the flow given by Eq. (7.6) and, consequently, need to be solved for as part of the general flow problem. The projection operators are the adjoints of the volume averaging operators \mathcal{J} , \mathcal{N} , and \mathcal{K} that are used to extract the particle velocities, \mathcal{V} , angular velocities, \mathcal{W} , and local rates-of-strain, \mathcal{E} , from the fluid velocity and its derivatives,

$$\mathcal{V} = \mathcal{J}[\mathbf{u}]\tag{7.14}$$

$$\mathcal{W} = \mathcal{N}[\mathbf{u}]\tag{7.15}$$

$$\mathcal{E} = -\mathcal{K}[\mathbf{u}].\tag{7.16}$$

The expressions for these operators are most clearly expressed when they are restricted to particle n ,

$$\mathbf{V}^n = (\mathcal{J}[\mathbf{u}])_n = \int \mathbf{u} \Delta_n(\mathbf{x}) d^3 \mathbf{x} \quad (7.17)$$

$$\boldsymbol{\Omega}^n = (\mathcal{N}[\mathbf{u}])_n = \frac{1}{2} \int \mathbf{u} \times \nabla \Theta_n(\mathbf{x}) d^3 \mathbf{x} \quad (7.18)$$

$$\begin{aligned} \mathbf{E}^n &= -(\mathcal{K}[\mathbf{u}])_n \\ &= -\frac{1}{2} \int \left[\mathbf{u} (\nabla \Theta_n(\mathbf{x}))^T + \nabla \Theta_n(\mathbf{x}) \mathbf{u}^T \right] d^3 \mathbf{x} \end{aligned} \quad (7.19)$$

If periodic or no-slip conditions are imposed on the bounding surfaces, integration by parts of Eqs. (7.18) and (7.19) reveals that the particle angular velocities and local rates-of-strain are the local volume averages of the fluid vorticity and rate-of-strain, respectively. With this in mind, the constraint Eq. (7.6) insists the local rate-of-strain must be zero as is the case for a rigid particle, and the stresslets can be viewed as the Lagrange multipliers included to enforce this constraint.

At this stage, it is useful to again note that the fluctuating and stochastic IBM share this framework with fluctuating FCM. The main differences between IBM and FCM are the choice of spreading function, and the only operators typically used with IBM are \mathcal{J} and its adjoint. The higher-order correction to the hydrodynamic interactions due to torques or stresslets resolved in FCM are not typically included with IBM. For FCM, the stresslets can be obtained using the conjugate gradient procedure describe by Yeo and Maxey [Yeo and Maxey \(2010b\)](#), and once found, the solution to Eq. (G.4) that satisfies Eq. (7.6) is determined. For the simulations performed in the proceeding sections, approximately 10 conjugate gradient iterations, each of which requires one Stokes solve, are required to reach a residual of $\|\mathcal{E}\| = 10^{-4}$, where

$$\|\mathcal{E}\| = \max_{n \in [1, N_p]} \|\mathbf{E}^n\|_2. \quad (7.20)$$

In designing, exploring, and constructing the time integration scheme that provides the Brownian drift term, we are particularly mindful of the computational cost associated with the stresslet computation, and in fact, seek to limit this computation to once per timestep.

7.3.1 Mobility matrices and the fluctuation dissipation theorem

Fluctuating FCM yields the deterministic and random velocities, corresponding to the first and third terms in Eqs (7.1) without ever directly computing the mobility matrix. Although they are never computed explicitly, expressions for the mobility matrices can be determined ([Keaveny \(2014\)](#)). For FCM, the mobility matrices provide the linear relationship between the deterministic particle velocities, angular velocities, and local

rates-of-strain and the forces, torques, and stresslets associated with the particles,

$$\begin{bmatrix} \mathcal{V} \\ \mathcal{W} \\ \mathcal{E} \end{bmatrix} = \begin{bmatrix} \mathcal{M}_{FCM}^{\mathcal{V}\mathcal{F}} & \mathcal{M}_{FCM}^{\mathcal{V}\mathcal{T}} & \mathcal{M}_{FCM}^{\mathcal{V}\mathcal{S}} \\ \mathcal{M}_{FCM}^{\mathcal{W}\mathcal{F}} & \mathcal{M}_{FCM}^{\mathcal{W}\mathcal{T}} & \mathcal{M}_{FCM}^{\mathcal{W}\mathcal{S}} \\ \mathcal{M}_{FCM}^{\mathcal{E}\mathcal{F}} & \mathcal{M}_{FCM}^{\mathcal{E}\mathcal{T}} & \mathcal{M}_{FCM}^{\mathcal{E}\mathcal{S}} \end{bmatrix} \begin{bmatrix} \mathcal{F} \\ \mathcal{T} \\ \mathcal{S} \end{bmatrix}. \quad (7.21)$$

As shown in our previous work (Keaveny (2014)), the submatrices can be expressed using the Gaussian spreading functions, Eqs. (7.12) and (7.13) and the Green's function $\mathbf{G}(\mathbf{x}, \mathbf{y})$ for the Stokes equations. For example, the entries of the matrix $\mathcal{M}_{FCM}^{\mathcal{V}\mathcal{F}}$ linking particles n and m are given by

$$\mathcal{M}_{FCM}^{\mathcal{V}\mathcal{F};nm} = \int \int \Delta_n(\mathbf{x}) \mathbf{G}(\mathbf{x}, \mathbf{y}) \Delta_m(\mathbf{y}) d^3\mathbf{x} d^3\mathbf{y}. \quad (7.22)$$

Similar expressions can be found for the other matrices in the appendix of our previous work (Keaveny (2014)). As described by Delong et al. (2014), these matrices can also be expressed using the projection, volume averaging, and Stokes operators. For $\mathcal{M}_{FCM}^{\mathcal{V}\mathcal{F}}$, the expression is

$$\mathcal{M}_{FCM}^{\mathcal{V}\mathcal{F}} = \mathcal{J}[\mathcal{L}^{-1}[\mathcal{J}^\dagger[\cdot]]] \quad (7.23)$$

where \mathcal{L}^{-1} represents the inverse Stokes operator.

In the absence of the stresslets, the mobility matrix for FCM reduces to

$$\mathcal{M}_{FCM} = \begin{bmatrix} \mathcal{M}_{FCM}^{\mathcal{V}\mathcal{F}} & \mathcal{M}_{FCM}^{\mathcal{V}\mathcal{T}} \\ \mathcal{M}_{FCM}^{\mathcal{W}\mathcal{F}} & \mathcal{M}_{FCM}^{\mathcal{W}\mathcal{T}} \end{bmatrix} \begin{bmatrix} \mathcal{F} \\ \mathcal{T} \end{bmatrix}. \quad (7.24)$$

If the stresslets are included, they can be found using Eq. (7.21). Since for rigid particles the local rates-of-strain are zero, we have $\mathcal{E} = 0$ and, in terms of the forces and torques, the stresslets will be given by

$$\mathcal{S} = -\mathcal{R}_{FCM}^{\mathcal{E}\mathcal{S}} (\mathcal{M}_{FCM}^{\mathcal{E}\mathcal{F}} \mathcal{F} + \mathcal{M}_{FCM}^{\mathcal{E}\mathcal{T}} \mathcal{T}). \quad (7.25)$$

where we have written $\mathcal{R}_{FCM}^{\mathcal{E}\mathcal{S}} = (\mathcal{M}_{FCM}^{\mathcal{E}\mathcal{S}})^{-1}$. From this expression for \mathcal{S} , we find the stresslet-corrected mobility matrix is

$$\mathcal{M}_{FCM-S} = \begin{bmatrix} \mathcal{M}_{FCM-S}^{\mathcal{V}\mathcal{F}} & \mathcal{M}_{FCM-S}^{\mathcal{V}\mathcal{T}} \\ \mathcal{M}_{FCM-S}^{\mathcal{W}\mathcal{F}} & \mathcal{M}_{FCM-S}^{\mathcal{W}\mathcal{T}} \end{bmatrix} \quad (7.26)$$

where

$$\begin{aligned} \mathcal{M}_{FCM-S}^{\mathcal{V}\mathcal{F}} &= \mathcal{M}_{FCM}^{\mathcal{V}\mathcal{F}} - \mathcal{M}_{FCM}^{\mathcal{V}\mathcal{S}} \mathcal{R}_{FCM}^{\mathcal{E}\mathcal{S}} \mathcal{M}_{FCM}^{\mathcal{E}\mathcal{F}}, \\ \mathcal{M}_{FCM-S}^{\mathcal{V}\mathcal{T}} &= \mathcal{M}_{FCM}^{\mathcal{V}\mathcal{T}} - \mathcal{M}_{FCM}^{\mathcal{V}\mathcal{S}} \mathcal{R}_{FCM}^{\mathcal{E}\mathcal{S}} \mathcal{M}_{FCM}^{\mathcal{E}\mathcal{T}}, \\ \mathcal{M}_{FCM-S}^{\mathcal{W}\mathcal{F}} &= \mathcal{M}_{FCM}^{\mathcal{W}\mathcal{F}} - \mathcal{M}_{FCM}^{\mathcal{W}\mathcal{S}} \mathcal{R}_{FCM}^{\mathcal{E}\mathcal{S}} \mathcal{M}_{FCM}^{\mathcal{E}\mathcal{F}}, \\ \mathcal{M}_{FCM-S}^{\mathcal{W}\mathcal{T}} &= \mathcal{M}_{FCM}^{\mathcal{W}\mathcal{T}} - \mathcal{M}_{FCM}^{\mathcal{W}\mathcal{S}} \mathcal{R}_{FCM}^{\mathcal{E}\mathcal{S}} \mathcal{M}_{FCM}^{\mathcal{E}\mathcal{T}}. \end{aligned}$$

Again, while these matrices are never computed explicitly, we know that they exist. This allows us to draw a parallel between fluctuating FCM and traditional methods for

suspended particles such as Brownian dynamics (Ermak and McCammon (1978)) and Stokesian dynamics (Brady (1988)). In addition, the expressions for the mobility matrices will prove useful in the analysis that demonstrates the time-integration scheme we propose in this study yields the correct first and second moments of the incremental change in the particle positions to first order in time.

The expressions for the mobility matrices can also be used to demonstrate that the random motion of the particles obtained using fluctuating FCM complies with the fluctuation-dissipation theorem (Kubo (1966)). If we consider the flow,

$$\begin{aligned}\nabla p - \eta \nabla^2 \tilde{\mathbf{u}} &= \nabla \cdot \mathbf{P} \\ \nabla \cdot \tilde{\mathbf{u}} &= 0\end{aligned}\tag{7.27}$$

$$\mathcal{K}[\tilde{\mathbf{u}}] = \mathbf{0},\tag{7.28}$$

the resulting particle velocities are then

$$\tilde{\mathcal{V}} = \mathcal{J}[\tilde{\mathbf{u}}].\tag{7.29}$$

By examining the velocity corrections explicitly, one can show (Keaveny (2014)) that the particle velocities given by Eq. (7.29) satisfy the fluctuation-dissipation theorem (Kubo (1966)). For fluctuating FCM, we have that

$$\langle \tilde{\mathcal{V}} \tilde{\mathcal{V}}^T \rangle = 2k_B T \mathcal{M}_{FCM}^{\mathcal{V}T}\tag{7.30}$$

when Eq. (7.28) is not enforced (i.e. $\mathcal{S} = 0$) and

$$\langle \tilde{\mathcal{V}} \tilde{\mathcal{V}}^T \rangle = 2k_B T \mathcal{M}_{FCM-S}^{\mathcal{V}T}\tag{7.31}$$

when the constraint Eq. (7.28) is enforced. A similar result has been shown in the context of the stochastic and fluctuating IBMs (Atzberger et al. (2007); DeLong et al. (2014)). Thus, by simply applying the volume averaging operators to the fluid flow induced by the white-noise fluctuating stress, we can obtain random particle velocities consistent with the noise terms in the stochastic equations of motion. This is done without ever needing to explicitly form and decompose the mobility matrix, leading to a great reduction in the computational effort needed to compute these terms.

7.4 Time integration

While fluctuating FCM provides the deterministic and random particle velocities corresponding to the first and last terms in the equations of motion Eq. (7.1), the Brownian drift, $k_B T \nabla_{\mathcal{Y}} \cdot \mathcal{M}_{FCM-S}^{\mathcal{V}F}$, would also need to be accounted for to advance the particle positions in time. Therefore, simply applying the Euler-Maruyama scheme (Kloeden and Platen (1992))

$$\begin{aligned}\nabla p^k - \eta \nabla^2 \mathbf{u}^k &= (\Delta t)^{-\frac{1}{2}} \nabla \cdot \mathbf{P}^k + \mathcal{J}^{\dagger;k}[\mathcal{F}^k] + \mathcal{N}^{\dagger;k}[\mathcal{T}^k] + \mathcal{K}^{\dagger;k}[\mathcal{S}^k] \\ \nabla \cdot \mathbf{u}^k &= 0, \\ \mathcal{K}^k[\mathbf{u}^k] &= \mathbf{0},\end{aligned}\tag{7.32}$$

$$\mathcal{Y}^{k+1} = \mathcal{Y}^k + \Delta t \mathcal{J}^k[\mathbf{u}^k],\tag{7.33}$$

which does not account for $k_B T \nabla_{\mathbf{y}} \cdot \mathcal{M}_{FCM-S}^{\mathcal{V}\mathcal{F}}$, will not provide the correct suspension dynamics. Rather than resorting to computing the drift term explicitly, however, its effects can be successfully incorporated into a simulation by using an appropriately designed time integration scheme (Fixman (1978); Grassia et al. (1995); DeLong et al. (2014)). In this section, we discuss these schemes, and building from the ideas used in their construction, we introduce a new scheme called the drifter-corrector (DC). The DC has the particular advantage that when constraints are imposed on the flow to recover higher-order corrections for the particle interactions, they need only to be imposed once per time-step. This leads to a non-negligible reduction in computational cost with respect to other schemes. For the DC, the total additional computational cost per timestep for fluctuating FCM with respect to its deterministic counterpart is a single Stokes solve per timestep.

7.4.1 Fixman's method

In the late 1970's, Fixman (Fixman (1978); Grassia et al. (1995)) developed a midpoint integration scheme to account for the drift term. The key to recovering the drift is that the scheme employs the same random forces at time levels t_k and $t_{k+1/2}$ while using updated values for the particle positions at level $t_{k+1/2}$. Applying Fixman's method to fluctuating FCM yields the following scheme

$$\begin{aligned} \nabla p^k - \eta \nabla^2 \mathbf{u}^k &= \mathcal{J}^{\dagger;k} [\mathcal{F}^k + \tilde{\mathcal{F}}^k] + \mathcal{N}^{\dagger;k} [\mathcal{T}^k + \tilde{\mathcal{T}}^k] + \mathcal{K}^{\dagger;k} [\mathcal{S}^k] \\ \nabla \cdot \mathbf{u}^k &= 0, \\ \mathcal{K}^k [\mathbf{u}^k] &= \mathbf{0}, \end{aligned} \tag{7.34}$$

$$\mathcal{Y}^{k+1/2} = \mathcal{Y}^k + \frac{\Delta t}{2} \mathcal{J}^k [\mathbf{u}^k] \tag{7.35}$$

$$\begin{aligned} \nabla p^{k+1/2} - \eta \nabla^2 \mathbf{u}^{k+1/2} &= \mathcal{J}^{\dagger;k+1/2} [\mathcal{F}^k + \tilde{\mathcal{F}}^k] + \mathcal{N}^{\dagger;k+1/2} [\mathcal{T}^k + \tilde{\mathcal{T}}^k] + \mathcal{K}^{\dagger;k+1/2} [\mathcal{S}^{k+1/2}] \\ \nabla \cdot \mathbf{u}^{k+1/2} &= 0, \\ \mathcal{K}^{k+1/2} [\mathbf{u}^{k+1/2}] &= \mathbf{0}, \end{aligned} \tag{7.36}$$

$$\mathcal{Y}^{k+1} = \mathcal{Y}^k + \Delta t \mathcal{J}^{k+1/2} [\mathbf{u}^{k+1/2}]. \tag{7.37}$$

The subscripts k and $k+1/2$ indicate whether the operators are evaluated at the positions \mathcal{Y}^k , or $\mathcal{Y}^{k+1/2}$. This scheme provides the first and second moments of the increment up to first order in Δt . While this scheme does avoid a direct calculation of the Brownian drift term, it requires the usage of random forces $\tilde{\mathcal{F}}^k$ and torques $\tilde{\mathcal{T}}^k$. For fluctuating FCM and other fluctuating hydrodynamics-based approaches that naturally yield velocities and angular velocities, this can be quite inconvenient. For example, for fluctuating FCM, to find the random forces and torques one must solve the linear system

$$\begin{bmatrix} \tilde{\mathcal{V}}^k \\ \tilde{\mathcal{W}}^k \\ -\tilde{\mathcal{E}}^k \end{bmatrix} = \mathcal{M}_{FCM}^{SPD;k} \begin{bmatrix} \tilde{\mathcal{F}}^k \\ \tilde{\mathcal{T}}^k \\ \tilde{\mathcal{S}}^k \end{bmatrix}, \tag{7.38}$$

where $\tilde{\mathcal{V}}^k = \mathcal{J}^k[\tilde{\mathbf{u}}^k]$, $\tilde{\mathcal{W}}^k = \mathcal{N}^k[\tilde{\mathbf{u}}^k]$, $\tilde{\mathcal{E}}^k = \mathcal{K}^k[\tilde{\mathbf{u}}^k]$, and

$$\begin{aligned}\nabla p^k - \eta \nabla^2 \tilde{\mathbf{u}}^k &= (\Delta t)^{-\frac{1}{2}} \nabla \cdot \mathbf{P}^k \\ \nabla \cdot \tilde{\mathbf{u}}^k &= 0.\end{aligned}\tag{7.39}$$

The matrix $\mathcal{M}_{FCM}^{SPD;k}$ is the grand FCM mobility matrix at step k where the sign of the last row has been changed to make it symmetric positive definite (SPD) (Yeo and Maxey (2010b)),

$$\mathcal{M}_{FCM}^{SPD;k} = \begin{bmatrix} \mathcal{M}_{FCM}^{\mathcal{VF};k} & \mathcal{M}_{FCM}^{\mathcal{VT};k} & \mathcal{M}_{FCM}^{\mathcal{VS};k} \\ \mathcal{M}_{FCM}^{\mathcal{WF};k} & \mathcal{M}_{FCM}^{\mathcal{WT};k} & \mathcal{M}_{FCM}^{\mathcal{WS};k} \\ -\mathcal{M}_{FCM}^{\mathcal{EF};k} & -\mathcal{M}_{FCM}^{\mathcal{ET};k} & -\mathcal{M}_{FCM}^{\mathcal{ES};k} \end{bmatrix}.\tag{7.40}$$

While this system can be solved using conjugate gradient methods, each iteration requires solving the Stokes equations. Simulations with $N = 183$ particles corresponding to a volume fraction of $\phi_v = 0.1$ required approximately 25 iterations to find the random forces and torques (Keaveny (2014)). This computation, along with having to compute the stresslets twice per timestep, severely limit the scale at which Brownian simulations could be performed using the fluctuating FCM, as well as other fluctuating hydrodynamics-based methods.

7.4.2 Random Finite Differencing

To help overcome this challenge, Delong et al. (2014) introduced the random finite difference (RFD). RFD takes advantage of the fact that the random forces and torques and the resulting displacements used in Fixman's method are in fact one of many possible choices that could be used to account for Brownian drift. Specifically, they show that using random displacements $\delta\Delta\mathcal{Y}$, as well as randomly particle forcing $\Delta\mathcal{F}/\delta$, the divergence of a mobility matrix, \mathcal{M} , can be approximated from

$$\frac{1}{\delta} \langle \mathcal{M}(\mathcal{Y} + \delta\Delta\mathcal{Y}) \Delta\mathcal{F} - \mathcal{M}(\mathcal{Y}) \Delta\mathcal{F} \rangle = \nabla_{\mathcal{Y}} \cdot \mathcal{M} + O(\delta)\tag{7.41}$$

provided that $\langle \Delta\mathcal{Y} \Delta\mathcal{F} \rangle = \mathcal{I}$. Therefore, one can simply choose $\Delta\mathcal{Y} = \Delta\mathcal{F} = \boldsymbol{\xi}$, where $\boldsymbol{\xi}$ is a $3N_p \times 1$ vector of independent Gaussian random variables with zero mean and unit variance. This eliminates the need to solve any linear system. The concept of random finite differencing can also be extended to higher-order accuracy. For example, the central random finite difference

$$\frac{1}{\delta} \langle \mathcal{M}(\mathcal{Y} + \delta\boldsymbol{\xi}/2) \boldsymbol{\xi} - \mathcal{M}(\mathcal{Y} - \delta\boldsymbol{\xi}/2) \boldsymbol{\xi} \rangle = \nabla_{\mathcal{Y}} \cdot \mathcal{M} + O(\delta^2)\tag{7.42}$$

Thus, in general, a weakly first-order accurate scheme that accounts for the Brownian drift term can be constructed by adding an RFD to the Euler-Maruyama scheme. Applying

this to fluctuating FCM, we have

$$\begin{aligned}\nabla p^k - \eta \nabla^2 \mathbf{u}^k &= (\Delta t)^{-\frac{1}{2}} \nabla \cdot \mathbf{P}^k + \mathcal{J}^{\dagger;k}[\mathcal{F}^k - \boldsymbol{\xi}/\delta] + \mathcal{N}^{\dagger;k}[\mathcal{T}^k] + \mathcal{K}^{\dagger;k}[\mathcal{S}^k] \\ \nabla \cdot \mathbf{u}^k &= 0, \\ \mathcal{K}^k[\mathbf{u}^k] &= \mathbf{0},\end{aligned}\tag{7.43}$$

$$\begin{aligned}\nabla p^{k+\delta} - \eta \nabla^2 \mathbf{u}^{k+\delta} &= \mathcal{J}^{\dagger;k+\delta}[\boldsymbol{\xi}/\delta] + \mathcal{K}^{\dagger;k+\delta}[\mathcal{S}^{k+\delta}] \\ \nabla \cdot \mathbf{u}^{k+\delta} &= 0, \\ \mathcal{K}^{k+\delta}[\mathbf{u}^{k+\delta}] &= \mathbf{0},\end{aligned}\tag{7.44}$$

$$\mathcal{Y}^{k+1} = \mathcal{Y}^k + \Delta t \mathcal{J}^k[\mathbf{u}^k] + \Delta t \mathcal{J}^{k+\delta}[\mathbf{u}^{k+\delta}].\tag{7.45}$$

A similar scheme can be constructed using central RFD to account for the Brownian drift. Comparing the resulting scheme with Fixman's method, we immediately see that using RFD eliminates the need to compute any random forces or torques, making this approach much more suited for fluctuating FCM.

7.4.3 Drifter-Corrector

While the usage of RFD provides a clear advantage over Fixman's method for fluctuating hydrodynamics-based methods, we see that it does require that the stresslets be determined twice per timestep (three times per timestep if using central RFD). The cost of performing a Brownian simulation is then at least double that of a deterministic simulation of the same system. For fluctuating FCM where the conjugate gradient method is used to find the stresslets, the additional cost of including Brownian motion would then be approximately 10 Stokes solves per timestep.

In an effort to mitigate this computational cost as much as possible, we build on the ideas introduced by Fixman (Fixman (1978); Grassia et al. (1995)) and Delong et al. (2014) and construct a mid-point scheme that accounts for Brownian drift at the cost of one Stokes solve per time-step. We will refer to this scheme as the *drifter-corrector* (DC). Specifically, the DC is

$$\begin{aligned}\nabla p^k - \eta \nabla^2 \tilde{\mathbf{u}}^k &= (\Delta t)^{-\frac{1}{2}} \nabla \cdot \mathbf{P}^k \\ \nabla \cdot \tilde{\mathbf{u}}^k &= 0,\end{aligned}\tag{7.46}$$

$$\mathcal{Y}^{k+1/2} = \mathcal{Y}^k + \frac{\Delta t}{2} \mathcal{J}^k[\tilde{\mathbf{u}}^k]\tag{7.47}$$

$$\begin{aligned}\nabla p^{k+1/2} - \eta \nabla^2 \mathbf{u}^{k+1/2} &= (\Delta t)^{-\frac{1}{2}} \nabla \cdot \mathbf{P}^k + \mathcal{J}^{\dagger;k+1/2}[\mathcal{F}^{k+1/2}] \\ &\quad + \mathcal{N}^{\dagger;k+1/2}[\mathcal{T}^{k+1/2}] + \mathcal{K}^{\dagger;k+1/2}[\mathcal{S}^{k+1/2}] \\ \nabla \cdot \mathbf{u}^{k+1/2} &= 0, \\ \mathcal{K}^{k+1/2}[\mathbf{u}^{k+1/2}] &= \mathbf{0},\end{aligned}\tag{7.48}$$

$$\mathcal{Y}^{k+1} = \mathcal{Y}^k + \Delta t(1 + v^k) \mathcal{J}^{k+1/2}[\mathbf{u}^{k+1/2}].\tag{7.49}$$

The scalar factor, v^k , is computed from

$$v^k = \sum_n \sum_i \left[\tilde{\mathbf{U}}^k \left(\mathbf{Y}^{n;k} + \frac{\Delta t}{2} \hat{\mathbf{e}}^{(i)} \right) - \tilde{\mathbf{U}}^k(\mathbf{Y}^{n;k}) \right] \cdot \hat{\mathbf{e}}^{(i)} \quad (7.50)$$

where $\tilde{\mathbf{U}}^k(\mathbf{Y}^{n;k}) = (\mathcal{J}^k[\tilde{\mathbf{u}}^k])_n$. This factor is determined by displacing the individual particle positions in the basis directions $\hat{\mathbf{e}}^{(i)}$, obtaining the particle velocities at these positions from the unconstrained fluctuating flow field, and finally, performing a finite difference of the particle velocities. We show explicitly in Appendix D that the expansions of the DC for the first and second moments of the increment $\Delta \mathcal{Y}^k = \mathcal{Y}^{k+1} - \mathcal{Y}^k$ are

$$\langle \Delta \mathcal{Y}^k \rangle = \Delta t \mathcal{M}_{FCM-S}^{\mathcal{V}\mathcal{F};k} \mathcal{F}^k + \mathcal{M}_{FCM-S}^{\mathcal{V}\mathcal{T};k} \mathcal{T}^k + \Delta t k_B T \nabla_{\mathcal{Y}} \cdot \mathcal{M}_{FCM-S}^{\mathcal{V}\mathcal{F};k} + O(\Delta t^2), \quad (7.51)$$

and

$$\langle \Delta \mathcal{Y}^k (\Delta \mathcal{Y}^k)^T \rangle = 2k_B T \Delta t \mathcal{M}_{FCM-S}^{\mathcal{V}\mathcal{F};k} + O(\Delta t^2), \quad (7.52)$$

respectively.

If we have periodic boundary conditions, or if $\mathbf{u} \cdot \hat{\mathbf{n}} = 0$ pointwise on the boundary, where $\hat{\mathbf{n}}$ is the unit normal to the boundary, then the correct first and second moments can be achieved with $v^k = 0$. For this case, the DC simplifies to become

$$\begin{aligned} \nabla p^k - \eta \nabla^2 \tilde{\mathbf{u}}^k &= (\Delta t)^{-\frac{1}{2}} \nabla \cdot \mathbf{P}^k \\ \nabla \cdot \tilde{\mathbf{u}}^k &= 0, \end{aligned} \quad (7.53)$$

$$\mathcal{Y}^{k+1/2} = \mathcal{Y}^k + \frac{\Delta t}{2} \mathcal{J}^k[\tilde{\mathbf{u}}^k] \quad (7.54)$$

$$\begin{aligned} \nabla p^{k+1/2} - \eta \nabla^2 \mathbf{u}^{k+1/2} &= (\Delta t)^{-\frac{1}{2}} \nabla \cdot \mathbf{P}^k + \mathcal{J}^{\dagger;k+1/2}[\mathcal{F}^{k+1/2}] \\ &\quad + \mathcal{N}^{\dagger;k+1/2}[\mathcal{T}^{k+1/2}] + \mathcal{K}^{\dagger;k+1/2}[\mathcal{S}^{k+1/2}] \\ \nabla \cdot \mathbf{u}^{k+1/2} &= 0, \\ \mathcal{K}^{k+1/2}[\mathbf{u}^{k+1/2}] &= \mathbf{0}, \end{aligned} \quad (7.55)$$

$$\mathcal{Y}^{k+1} = \mathcal{Y}^k + \Delta t \mathcal{J}^{k+1/2}[\mathbf{u}^{k+1/2}]. \quad (7.56)$$

The DC, therefore, first moves the particles a half timestep using the particle velocities obtained from the unconstrained fluctuating flow field. Then, using the updated positions, but the same realization of the fluctuating stress, the particle forces and torques are projected onto the fluid, and the local rate-of-strain constraint is imposed. The particle positions are then updated using the resulting particle velocities. Thus, for the DC, the stresslets need to be computed only once per timestep, and the only additional cost is the single Stokes solve to determine the unconstrained fluctuating flow field. We note that a second-order approximation of the deterministic terms may be achieved by also including particle forcing (torques, forces, and stresslets) in Eq. (7.53), but this would come at the cost of an additional stresslet iteration per timestep. We note that similar ideas were employed by [Delong et al. \(2014\)](#) to construct a midpoint scheme using RFD. In their

construction, however, they relied on a specific decomposition of the mobility matrix that is not applicable in the case where the local rate-of-strain constraint is enforced. Nevertheless, our analysis reveals that this similar technique extends to the case where the stresslets are accounted for, and further, our analysis reveals the RFD of the spreading operator included in their midpoint scheme may be excluded if $\mathbf{u} \cdot \hat{\mathbf{n}} = 0$ on the boundary.

7.5 Numerical studies

To demonstrate the performance of the DC with fluctuating FCM, we perform simulations of particulate suspensions under both dynamic and equilibrium conditions. These simulations confirm the results of our theoretical analysis of the DC, and show, in practice, that it is able to produce the correct dynamics and final equilibrium states for distributions of particles. Our results also show that with the DC, fluctuating FCM can be used for large-scale simulation of Brownian suspensions even when higher order corrections to the hydrodynamic interactions are included.

7.5.1 Spatial discretization

In our simulations, we mainly consider periodic boundary conditions and use a Fourier spectral method with fast Fourier transforms to solve the Stokes equations, taking advantage of the highly scalable MPI library P3DFFT (Pekurovsky (2012)). We give here a summary of the main steps of the discretization scheme as a detailed description is provided in our previous work (Keaveny (2014)).

For the case where each side of the domain has length L , we use M grid points in each direction. The total number of grid points is then $N_g = M^3$ and the grid spacing is given by $\Delta x = L/M$. The position of a grid point in a given direction is then $x_\alpha = \alpha\Delta x$ for $\alpha = 0, \dots, M - 1$ and the corresponding wave numbers are

$$k_\alpha = \begin{cases} 2\pi\alpha/L, & 0 \leq \alpha \leq M/2 \\ 2\pi(\alpha - M)/L, & M/2 + 1 \leq \alpha \leq M - 1. \end{cases} \quad (7.57)$$

At each grid point, the entries of the fluctuating stress are independent Gaussian random variables that obey the following statistics

$$\langle P_{ij}(x_\alpha, x_\beta, x_\gamma) \rangle = 0 \quad (7.58)$$

and

$$\langle P_{ij}(x_\alpha, x_\beta, x_\gamma) P_{pq}(x_\alpha, x_\beta, x_\gamma) \rangle = \frac{2k_B T \eta}{(\Delta x)^3} (\delta_{ip} \delta_{jq} + \delta_{iq} \delta_{jp}). \quad (7.59)$$

To this, we add the FCM force distribution,

$$\mathbf{f}_{FCM}(\mathbf{x}) = \mathcal{J}^\dagger[\mathcal{F}](\mathbf{x}) + \mathcal{Q}^\dagger[\mathcal{T}](\mathbf{x}) + \mathcal{K}^\dagger[\mathcal{S}](\mathbf{x}) \quad (7.60)$$

evaluated at the grid points, $\mathbf{x} = [x_\alpha \ x_\beta \ x_\gamma]^T$, taking also $\Delta_n(\mathbf{x}) = 0$ and $\Theta_n(\mathbf{x}) = 0$ for $|\mathbf{x} - \mathbf{Y}^n| > 3a$. To ensure sufficient resolution of \mathbf{f}_{FCM} , we take $\sigma_\Theta/\Delta x = 1.5$ and

$\sigma_\Delta/\Delta x = 1.86$. After taking the discrete Fourier transform (DFT) of the total force distribution, we compute the fluid velocity in Fourier space

$$\hat{\mathbf{u}}(k_\alpha, k_\beta, k_\gamma) = \frac{1}{\eta|\mathbf{k}|^2} \left(\mathbf{I} - \frac{\mathbf{k}\mathbf{k}}{|\mathbf{k}|^2} \right) \left(i\mathbf{k} \cdot (\Delta t)^{-1/2} \hat{\mathbf{P}}(k_\alpha, k_\beta, k_\gamma) + \hat{\mathbf{f}}_{FCM}(k_\alpha, k_\beta, k_\gamma) \right), \quad (7.61)$$

where $\mathbf{k} = [k_\alpha \ k_\beta \ k_\gamma]^T$. We set $\hat{\mathbf{u}}(\mathbf{k}) = 0$ if $|\mathbf{k}| = 0$ or if $\mathbf{k} \cdot \hat{\mathbf{e}}^{(i)} = M\pi/L$ for $i = 1, 2, \text{ or } 3$. After taking the inverse DFT to obtain the fluid velocity at the grid points, the velocity, angular velocity, and local rate-of-strain for each particle is computed by applying the spectrally accurate trapezoidal rule to equations Eqs. (7.17 - 7.19), where we again set $\Delta_n(\mathbf{x}) = 0$ and $\Theta_n(\mathbf{x}) = 0$ for $|\mathbf{x} - \mathbf{Y}^n| > 3a$.

For the case where the stresslets are ignored, we have $\mathcal{S} = 0$ and the Stokes equations need only to be solved once per time-step to obtain the particle velocities. If the stresslets are included, however, they must be solved for, and to do this, we employ the iterative conjugate gradient approach described in [Yeo and Maxey \(2010b\)](#).

7.5.2 Brownian dynamics between two slip surfaces

As an initial test of the scheme, we examine the Brownian dynamics of a spherical particle between two slip surfaces at $z = 0$ and $z = L/2$. On these surfaces, the boundary conditions for the flow are given by $\mathbf{u} \cdot \hat{\mathbf{z}} = 0$ and $(\mathbf{I} - \hat{\mathbf{z}}\hat{\mathbf{z}}^T)\nabla\mathbf{u} = \mathbf{0}$. The inclusion of these conditions ensures that the drift term proportional to the divergence of the mobility matrix is non-zero.

Image system and fluctuating stress for slip surfaces

Rather than enforcing these boundary conditions directly through the numerical solver, we can create the slip surfaces by introducing the appropriate image system for both the FCM particle force distribution, \mathbf{f}^{FCM} , and the fluctuating stress, \mathbf{P} . The flow due to the force distribution and its image can then be found using the Fourier spectral method described in Section 7.5.1.

In our simulations, the fluid domain is given by $\Omega = [0, L]^2 \times [0, L_z]$. We impose the slip conditions at $z = 0$ and $z = L_z$ and periodic boundary conditions on the other boundaries such that $\mathbf{u}(0, y, z) = \mathbf{u}(L, y, z)$ and $\mathbf{u}(x, 0, z) = \mathbf{u}(x, L, z)$. The force distribution due to particle forces is given by Eq. (7.62). To enforce the slip conditions at $z = 0$ and $z = L_z$, we first extend the fluid domain to $\Omega^* = [0, L]^2 \times [0, 2L_z]$ and utilize the modified FCM force distribution and its image,

$$\mathbf{f}^{FCM}(\mathbf{x}) = \begin{cases} \mathcal{J}^\dagger[\mathcal{F}](\mathbf{x}) + \mathcal{Q}^\dagger[\mathcal{T}](\mathbf{x}) + \mathcal{K}^\dagger[\mathcal{S}](\mathbf{x}) & , \mathbf{x} \in [0, L]^2 \times [0, L_z] \\ \mathbf{0} & , \mathbf{x} \in [0, L]^2 \times [L_z, 2L_z] \end{cases} \quad (7.62)$$

$$\mathbf{f}^{FCM,im}(\mathbf{x}) = \begin{cases} \mathbf{0} & , \mathbf{x} \in [0, L]^2 \times]0, L_z[\\ (\mathbf{I} - 2\hat{\mathbf{z}}\hat{\mathbf{z}}^T) \mathbf{f}^{FCM}(\mathbf{X}) & , \mathbf{x} \in [0, L]^2 \times [L_z, 2L_z] \end{cases} \quad (7.63)$$

where $\mathbf{X} = \mathbf{x} - 2(\mathbf{x} \cdot \hat{\mathbf{z}} - L_z)\hat{\mathbf{z}}$. The total forcing term that will now appear in the right hand side of Eq. (7.61) is given by the summation $\mathbf{f}^{FCM} + \mathbf{f}^{FCM,im}$. The flow is then determined over the domain Ω^* with the periodic boundary conditions in all directions. The combined effects of the image system and periodicity in the z -direction yields the desired slip conditions at $z = 0$ and $z = L_z$. Once the fluid flow is determined, the particle velocities, angular velocities, and local rates-of-strain are computed using the resulting flow restricted to the domain Ω .

In introducing the slip surfaces, one must make a choice as how to modify the Gaussian functions when the particles get close to the boundaries. In this work, we simply truncate any part of the Gaussian functions that extends beyond the domain Ω . This is already reflected in our definition of the force distribution, Eq. (7.62) and its image, Eq. (7.63). We use the same truncated Gaussians to compute the particle velocities, angular velocities, and local rates-of-strain, thereby preserving the adjoint properties of the operators. For particles in contact with the boundary, the truncated volume in Eq. (7.17) is approximately 3.8% of the total and for Eq. (7.19) it is only 1.4%. We note, that more sophisticated ways to modify the Gaussian envelopes have been explored and are implemented in FCM elsewhere (Yeo and Maxey (2010a)).

Along with the FCM particle force distributions, the fluctuating stress must also have the appropriate symmetries to satisfy the fluctuation-dissipation theorem when the slip boundaries are present. In Appendix C, we show explicitly that this is achieved by having

$$\langle P_{ij}(\mathbf{x}) \rangle = 0 \quad (7.64)$$

$$\langle P_{ij}(\mathbf{x})P_{kl}(\mathbf{y}) \rangle = 2k_B T \Delta_{ijkl} \delta(\mathbf{x} - \mathbf{y}) + 2k_B T \Gamma_{ijkl} \delta(\mathbf{x} - \mathbf{Y}) \quad (7.65)$$

for $\mathbf{x}, \mathbf{y} \in \Omega^*$ where

$$\Delta_{ijkl} = \delta_{ik}\delta_{jl} + \delta_{il}\delta_{jk} \quad (7.66)$$

$$\Gamma_{ijkl} = \gamma_{ik}\gamma_{jl} + \gamma_{il}\gamma_{jk}, \quad (7.67)$$

with $\gamma_{jk} = \delta_{jk} - 2\delta_{3j}\delta_{3k}$, and

$$\mathbf{Y} = \mathbf{y} - 2(\mathbf{y} \cdot \hat{\mathbf{z}} - L_z)\hat{\mathbf{z}}. \quad (7.68)$$

The symmetrized fluctuating stress Eq. (7.64)-(7.65) is discretized at each grid point with independent Gaussian random variables whose statistics are

$$\langle P_{ij}(x_\alpha, x_\beta, x_\gamma) \rangle = 0 \quad (7.69)$$

$$\langle P_{ij}(x_\alpha, x_\beta, x_\gamma)P_{kl}(x_\alpha, x_\beta, x_\kappa) \rangle = \frac{2k_B T}{(\Delta x)^3} \Delta_{ijkl} \delta_{\gamma\kappa} + \frac{2k_B T}{(\Delta x)^3} \Gamma_{ijkl} \delta_{\gamma\kappa^{im}} \quad (7.70)$$

where the index $\kappa^{im} = \text{mod}(M - \kappa, M)$. We remind the reader that the indices $\alpha, \beta, \gamma, \kappa$ go from 0 to $M - 1$, where M is the number of discretization points in a given direction.

Single particle mobility

With the slip boundaries present, the mobility matrix for a single particle has the form

$$\mathbf{M} = \mu_\perp(z)\hat{\mathbf{z}}\hat{\mathbf{z}}^T + \mu_\parallel(z)(\mathbf{I} - \hat{\mathbf{z}}\hat{\mathbf{z}}^T) \quad (7.71)$$

where the mobility coefficients $\mu_{\parallel}(z)$ and $\mu_{\perp}(z)$ depend on the distance from the slip surfaces. We determine the coefficient $\mu_{\perp}(z)$ for FCM by applying a unit force $\mathbf{F} = \hat{\mathbf{z}}$ on an isolated sphere and measuring the resulting velocity $V_z(z)$ at 400 equi-spaced values of z between $z = a$ and $z = L_z - a$. We perform these simulation both with and without the particle stresslets to obtain $\mu_{\perp}^{FCM-S}(z)$ and $\mu_{\perp}^{FCM}(z)$, respectively. The values of $2k_B T \mu_{\perp}^{FCM-S}(z)$ and $2k_B T \mu_{\perp}^{FCM}(z)$ are provided in Figure 7.1. We see that both with and without the stresslets, the value of this mobility coefficient decreases as the particle approaches the slip surface. The addition of the stresslet results in the mobility coefficient depending more strongly on z and further reduces the mobility coefficient by approximately 30% near the boundaries. We have performed similar computations for $\mu_{\parallel}(z)$ by taking $\mathbf{F} = \hat{\mathbf{x}}$, but have not included this data for brevity. We also note that given the symmetries associated with a single slip surface, the exact Stokes flow for a rigid sphere near a slip surface is equivalent to an appropriate two-sphere problem. A comparison of FCM with these two-sphere problems has been addressed by [Lomholt and Maxey \(2003\)](#), showing that FCM provides accurate results for a wide range of separations.

To ensure that the fluctuation-dissipation theorem for the particles is satisfied when the statistics for the fluctuating stress are given by Eq. (7.64)-(7.65), we compute the component of the random particle velocity $\tilde{V}_{\perp}(z)$ normal to the slip surface. We then can check that its correlations satisfy

$$\langle \tilde{V}_{\perp}^2 \rangle(z) = \frac{2k_B T \mu_{\perp}(z)}{\Delta t}. \quad (7.72)$$

To efficiently compile a large number of samples to accurately determine $\langle \tilde{V}_{\perp}^2 \rangle(z)$, we divide the domain in the z -direction into 200 equispaced parallel planes. Over each plane, we distribute 50 particles that do not interact with one another. For the stresslet case, particular care is taken to ensure that any interactions are removed. For 10000 realizations of the fluctuating stress, we compute $\tilde{V}_{\perp}(z)$ for each of the particles. For each fixed value of z , we compute $\langle \tilde{V}_{\perp}^2 \rangle(z)$ by averaging over the realizations and the 50 particles at that particular value of z . Figure 7.1 shows the correlations of the particle normal velocity, $\Delta t \langle \tilde{V}_{\perp}^2 \rangle(z)$, and the normal mobility coefficient in the channel, $2k_B T \mu_{\perp}(z)$. We see that for both cases, with and without the stresslets, the fluctuation-dissipation relation for the particles, Eq. (7.72), is satisfied. Though not shown, we have also performed the same check for the parallel random velocities and a similar strong agreement was found.

Equilibrium distribution between two slip surfaces

To demonstrate their RFD approach, [Delong et al. \(2014\)](#) performed simulations of a single spherical particle between two no-slip surfaces at $z = 0$ and $z = L_z$ and subject to

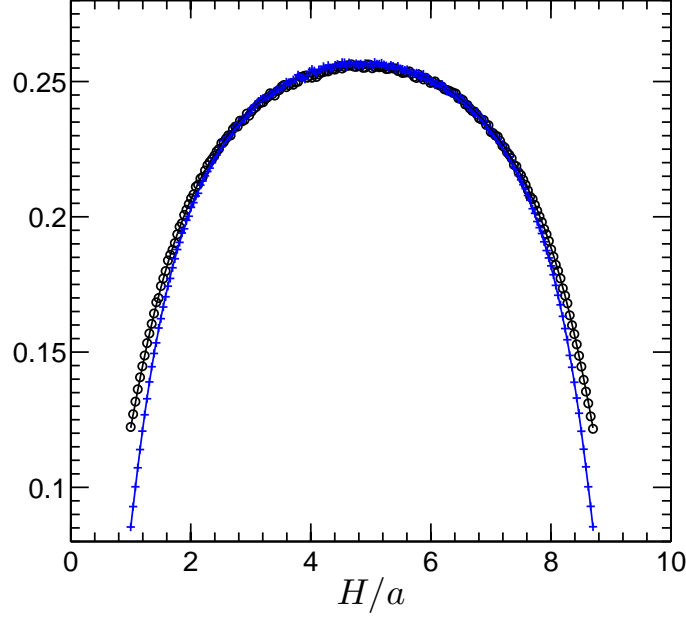


Figure 7.1: A comparison between the wall-normal mobility coefficient and the autocorrelation of the wall-normal particle velocity. — : $2k_B T \mu_{\perp}^{FCM}$, \circ : $\Delta t \left\langle \left(\tilde{V}_{\perp}^{FCM} \right)^2 \right\rangle$, — : $2k_B T \mu_{\perp}^{FCM-S}$, + : $\Delta t \left\langle \left(\tilde{V}_{\perp}^{FCM-S} \right)^2 \right\rangle$.

the potential

$$U(z) = \begin{cases} \frac{k}{2} (z - R_{ref})^2 & , z < R_{ref}, \\ \frac{k}{2} (z - (L_z - R_{ref}))^2 & , z > L_z - R_{ref}, \\ 0 & , \text{otherwise.} \end{cases} \quad (7.73)$$

When the particle comes within a distance R_{ref} from the wall, it experiences linear, repulsive force whose strength is governed by k . If the time integration scheme correctly accounts for the Brownian drift term, the equilibrium distribution of the particles will be given by the Boltzmann distribution,

$$P(z) = Z^{-1} \exp \left[-\frac{U(z)}{k_B T} \right] \quad (7.74)$$

where $Z = \int_0^{L_z} \exp \left[-\frac{U(z)}{k_B T} \right] dz$.

We consider a similar problem here, now simulating the dynamics of a spherical particle between two slip surfaces, but still subject to the potential $U(z)$. A sketch of this simulation is provided in Figure 7.2. Even though we have slip boundary conditions on the

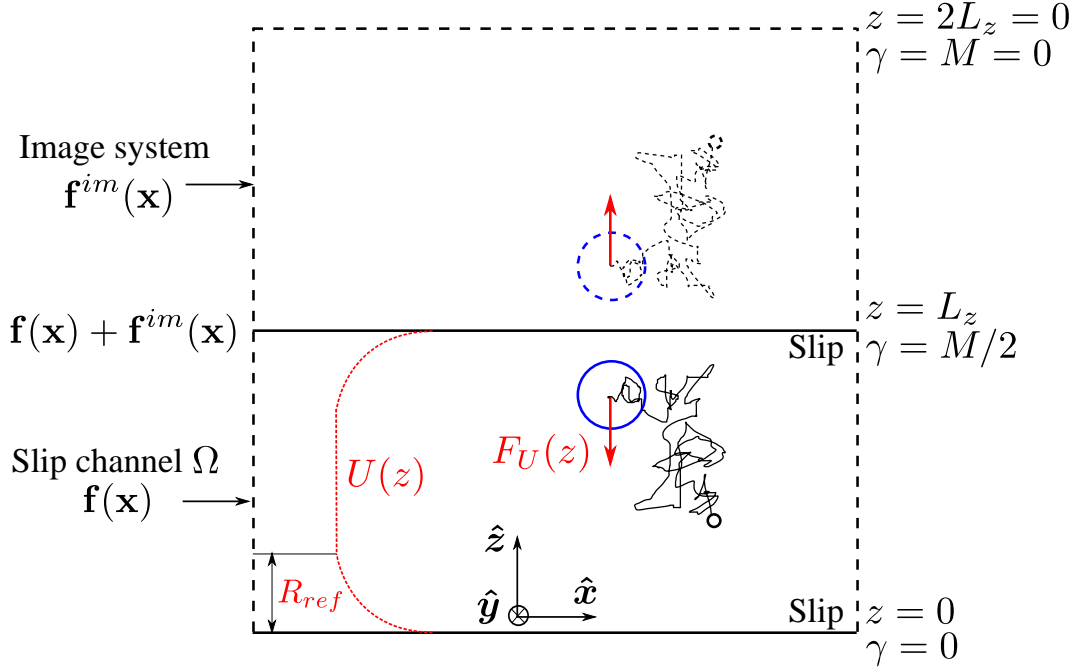


Figure 7.2: Sketch showing a particle (and its image) in the slip channel. The black dashed line represents the periodic boundaries conditions. The index γ runs over the z -coordinate of the grid. The potential $U(z)$ provides the interaction between the particle with the slip surfaces and is given by Eq. (7.73). The force on the particle is $F_U(z) = -\partial U/\partial z$.

walls, the distribution of particles should still be described by Eq. (7.74). We perform these simulations both with and without the stresslets and using both central RFD and the DC. We also integrate the equations using the Euler-Maruyama scheme, Eq. (7.33), which should instead yield the biased distribution (Delong et al. (2014)),

$$P_B(z) = Z_B^{-1} \exp \left[-\frac{U(z) + k_B T \ln(\mu_{\perp}(z))}{k_B T} \right] \quad (7.75)$$

In our simulations, we have set $L_z = 9.7a$, $L_x = L_y = 2L_z$, $R_{ref} = 1.4a$ and $k = 24k_B T/(\Delta x)^2$. For the RFD simulations we set $\delta = 10^{-6}\Delta x$. To obtain the equilibrium distribution, each simulations is performed with $N_p = 500$ non-interacting particles and run to time $t/t_{D_a} = 391.60$, where $t_{D_a} = \frac{a^2}{k_B T} \bar{\mu}_{\perp}$ is the average time required for the particle to diffuse one radius along the z -direction based on the averaged mobility coefficient

$$\bar{\mu}_{\perp} = \frac{1}{L_z - 2a} \int_a^{L_z - a} \mu_{\perp}(z) dz. \quad (7.76)$$

To determine $P(z)$ from the simulations, a histogram of the particle positions in the z -direction is compiled during the time window $t/t_{D_a} = 6.526 - 391.60$. The results from the simulations without the stresslets are shown in Figure 7.3a, while those with the stresslets

are given in Figure 7.3b. In both figures, we see that central RFD and the DC recover the correct Boltzmann distribution, Eq. (7.74). The Euler-Maruyama scheme, however, yields the biased distribution, Eq. (7.75), as the Brownian drift, $k_B T d\mu_\perp/dz$, is non-zero. We see also that compared to the stresslet-free case, when the stresslets are included the biased distribution exhibits higher peaks close to the boundaries. This is a direct result of the greater reduction in mobility near the boundaries when the stresslets are included, see Figure 7.1. One can then expect that using the correct integration scheme becomes even more important in simulations where the singular lubrication interactions with the boundaries are resolved.

Distribution dynamics

Along with characterizing the equilibrium distribution, we perform simulations to confirm that fluctuating FCM with the DC also yields the correct distribution dynamics. For non-interacting particles, the dynamics of the distribution is described by the Smoluchowski equation

$$\frac{\partial P}{\partial t} = -\frac{\partial}{\partial z} \left[\mu_\perp F_U P - k_B T \mu_\perp(z) \frac{\partial P}{\partial z} \right], \quad (7.77)$$

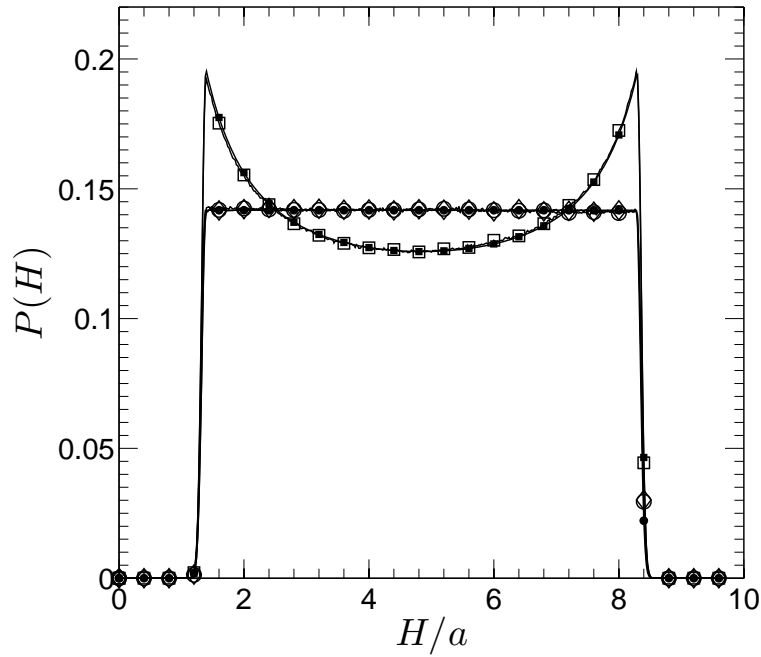
for the distribution $P(z, t)$ subject to no flux conditions

$$\left[\mu_\perp F_U P - k_B T \mu_\perp \frac{\partial P}{\partial z} \right] \Big|_{z=0, L_z} = 0 \quad (7.78)$$

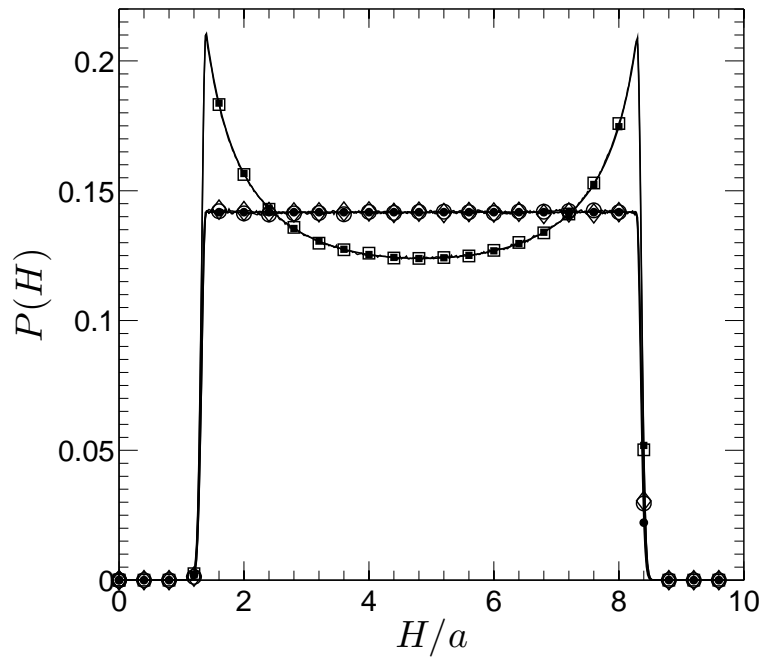
at the slip surfaces ($z = 0, z = L_z$). The advective flux term is proportional to the force $F_U = -\partial U/\partial z$ associated with the potential U . We solve Eq. (7.77) using a first-order finite volume solver where the advective fluxes are calculated using an upwinding scheme and the diffusive terms with a central scheme. We have validated the solver against analytical solutions of the heat and transport equations. The mobility coefficient $\mu_\perp(z)$ is determined by interpolating the values from our FCM simulations, see Figure 7.1, to the finite volume grid points.

We obtain the distribution dynamics from stresslet-corrected fluctuating FCM simulations by averaging the histogram time dynamics over 20 independent simulations each with 500 non-interacting particles. For these simulations, the initial particle positions are generated by distributing their positions uniformly in the center of the domain in the region $z \in [3L_z/8; 5L_z/8]$. We compare these results with our numerical solution of Eq. (7.77) using the distribution obtained from the fluctuating FCM simulations at $t = 0$ for the initial condition.

Figure 7.4 shows the dynamics of the distribution obtained from the fluctuating FCM simulations with the DC time integration, as well as the finite volume solution of Eq. (7.77). We see that the distributions given by both methods match as they evolve from the initial to the equilibrium state reached at time $t/t_{D_a} = 6.4$. This confirms further that the DC recovers the dynamics described by the Smoluchowski equation, Eq. (7.77), as desired.



(a)



(b)

Figure 7.3: The equilibrium distribution for a Brownian particle subject to the potential $U(z)$. The distribution from simulations is obtained by averaging 10 simulations of 500 non-interacting particles over the time interval $t/t_{D_a} = 6.526 - 391.60$. \ominus : DC, \diamond : Central RFD with $\delta = 10^{-6}\Delta x$, \bullet : Gibbs-Boltzmann distribution Eq. (7.74), \square : Euler-Maruyama Scheme, \blacksquare : Biased Gibbs-Boltzmann distribution Eq. (7.75). (a) Without stresslets, (b) With stresslet corrections.

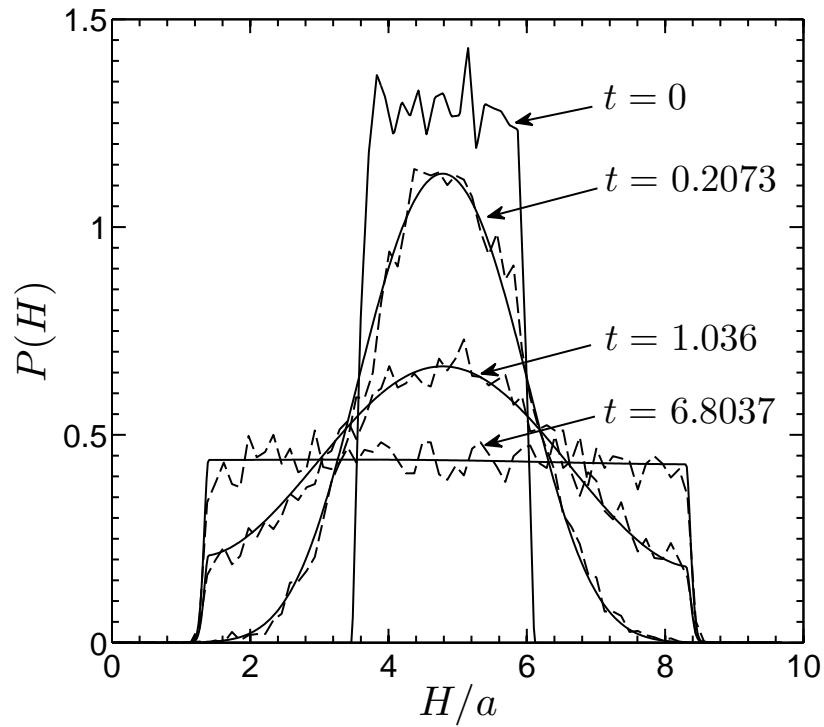


Figure 7.4: The evolution of the particle distribution during the time interval $t/t_{D_a} = 0 - 6.8037$. The results from the particle simulations are achieved by averaging over 20 simulations, each with 500 non-interacting particles. The stresslet corrections are included in these simulations. ---- : fluctuating FCM with the DC, — : solution to the Smoluchowski equation (7.77) - (7.78).

7.5.3 Colloidal gelation and percolation

An important application of the methodology presented in this paper is the large-scale simulation of interacting colloidal particles. Depending on the interactions between these particles, colloidal suspensions can take on both solid- and fluid-like properties (Segre et al. (2001); Anderson and Lekkerkerker (2002)). When the particles interact via an attractive potential, the suspension can transition from a fluid-like state to that of a solid through the process of gelation (Lu et al. (2008)). This transition depends not only on the potential, but also on the volume fraction occupied by the particles. Recent numerical studies have shown that the dynamics of this aggregation process will also depend on the hydrodynamic interactions between the particles (Yamamoto et al. (2008); Furukawa and Tanaka (2010); Whitmer and Luijten (2011); Cao et al. (2012)). In this section, we use fluctuating FCM with the DC to simulate of the aggregation and gelation of interacting particles, focusing particularly on the role of hydrodynamic interactions on the resulting structures. We compare our results with previous studies (Furukawa and Tanaka (2010); Cao et al. (2012); Delong et al. (2014)), demonstrating that fluctuating FCM with the DC provides an effective and computationally efficient approach for studying Brownian suspensions.

Collapsing icosahedron

A simple example that highlights the role of hydrodynamic interactions on colloidal aggregation is the collapse of a small cluster of Brownian spherical particles as originally studied by Furukawa and Tanaka (2010). Specifically, they considered $N_p = 13$ Brownian particles initially at the vertices of a regular icosahedron with edge length $8.08\Delta x$. The particles interact via a modified Asakura-Oosawa potential

$$U_{AO}(r) = \begin{cases} c(D_2^2 - D_1^2)r & , r < D \\ c(D_2^2 - 1/3r^2)r & , D_1 \leq r < D_2 \\ 0 & , r \geq D_2, \end{cases} \quad (7.79)$$

where r is the center-center distance between two particles, as well as a soft-core repulsive potential, $U_{SC} = \epsilon_{SC}(2a/r)^{24}$. The values of the parameters in these potentials are set to $D_1 = 2.245a$, $D_2 = 2.694a$, $c = 58.5/a^3$, and $\epsilon_{SC} = 10.0$. As the cluster evolved, they monitored the evolution of the radius of gyration

$$R_g(t) = \left[\frac{1}{N_p} \sum_{n=1}^{N_p} (\mathbf{Y}^n - \mathbf{Y}^c)^2 \right]^{1/2}, \quad (7.80)$$

where \mathbf{Y}^c is the position of the center of mass. Their results revealed that the hydrodynamic interactions slow the time of cluster collapse and lead to a final state in which the particles rearrange themselves within the cluster. Delong et al. (2014) used this test case to validate the treatment of hydrodynamic interactions in fluctuating IBM, showing that they matched Brownian Dynamics simulations with hydrodynamics given by the Rotne-Prager-Yamakawa tensor.

$\Delta U/k_B T$	c	ϵ_{SC}	$a/\Delta x$	η	$\Delta t/t_{Da}$	N_p	N_g
2.39	$58.5/a^3$	18.0	3.29	1	$2 \cdot 10^{-4}$	13	32^3

Table 7.1: Parameter values for the icosahedron collapse simulations.

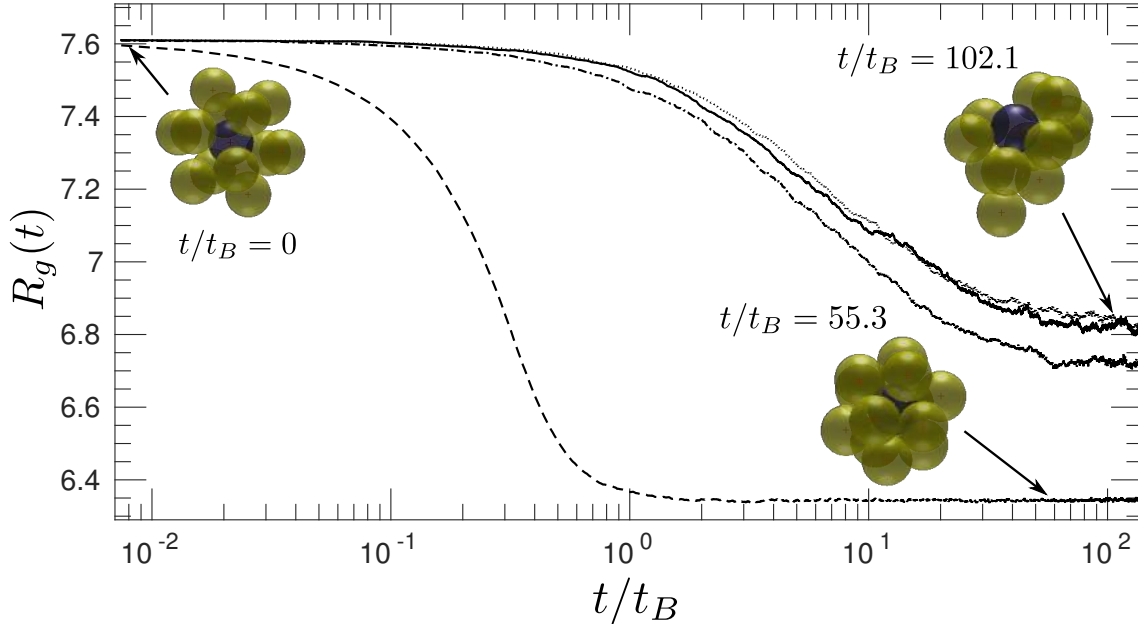


Figure 7.5: The radius of gyration $R_g(t)$ (in units of Δx) during the time interval $t/t_{Da} = 0 - 150$. The results are obtained by averaging over 150 independent simulations. ---- : no hydrodynamic interactions; -.-.- : FCM without stresslets, Euler-Maruyama scheme; : FCM-S, central RFD; — : FCM-S, DC.

We perform similar simulations of cluster collapse to both show that fluctuating FCM recovers previous results, but also to quantify the effects of the stresslet included in fluctuating FCM. The simulations are performed using periodic boundary conditions, applying directly the spatial discretization scheme described in Section 7.5.1. In our simulations, we set the magnitude of the repulsive potential to $\epsilon_{SC} = 18.0$, a slightly higher value than the one used by [Furukawa and Tanaka \(2010\)](#). The values of the other parameters used in our simulations are provided in Table 7.1. We also note that the inclusion of the particle stresslets necessitates a numerical scheme that accounts for Brownian drift such as the DC or RFD. If the stresslets were not included, the equations of motion could be integrated using the Euler-Maruyama scheme as the Brownian drift term is zero ([Keaveny \(2014\)](#)) in an unbounded or periodic domain.

Figure 7.5 shows the time evolution of the average radius of gyration given by fluctuating FCM with and without the particle stresslets. We also show data from simulations using the same interparticle potentials, but with hydrodynamic interactions ignored completely. For each case, the averages are obtained from 150 independent simulations. In addition, when the stresslets are present, we integrate the equations of motion using both

central RFD and the DC. As in [Furukawa and Tanaka \(2010\)](#) and [Delong et al. \(2014\)](#), we see from [Figure 7.5](#) that the hydrodynamic interactions impact both the evolution and final value of R_g by slowing down the collapse of the cluster. Here, we see also that the inclusion of the stresslets leads to a higher value of R_g during the collapse. The value of R_g with the particle stresslets given by central RFD and the DC are nearly identical.

We note that for each timestep, the central RFD scheme requires the stresslets to be solved for three times. One central RFD timestep therefore requires approximately 30 Stokes solves. While providing similar results as the central RFD approach, the DC requires just one iterative solve per time step (~ 10 Stokes solves). This is confirmed from our simulations which show that the average simulation time with the DC is more than three times less

$$\left\langle \frac{T_{sim}^{RFD}}{T_{sim}^{DC}} \right\rangle = 3.29 \pm 0.25$$

than that for central RFD. Again, we note that compared to a completely deterministic simulation, the additional cost per time-step of including Brownian motion for FCM with the DC is just the distribution of the random stresses on the grid, an $O(N_g)$ computation, and one additional Stokes solve, which for our FFT-based solver incurs an $O(N_g \log N_g)$ cost.

Aggregation and percolation in colloidal suspensions

As a final test and demonstration of the DC, we perform a series of fluctuating FCM simulations to examine colloidal gelation of a suspension of Brownian particles. We compare our results with those given by accelerated Stokesian Dynamics (ASD) in [Cao et al. \(2012\)](#). While we do not incorporate near-field lubrication hydrodynamics as is the case with ASD, we find the fluctuating FCM provides a very similar characterization of the gelation process, and with the DC we find the computations take a fraction of time of the ASD simulations.

As in [Cao et al. \(2012\)](#), we employ an interparticle potential that is a combination of a $(36 - 18)$ Lennard-Jones-like potential and a repulsive long-range Yukawa potential,

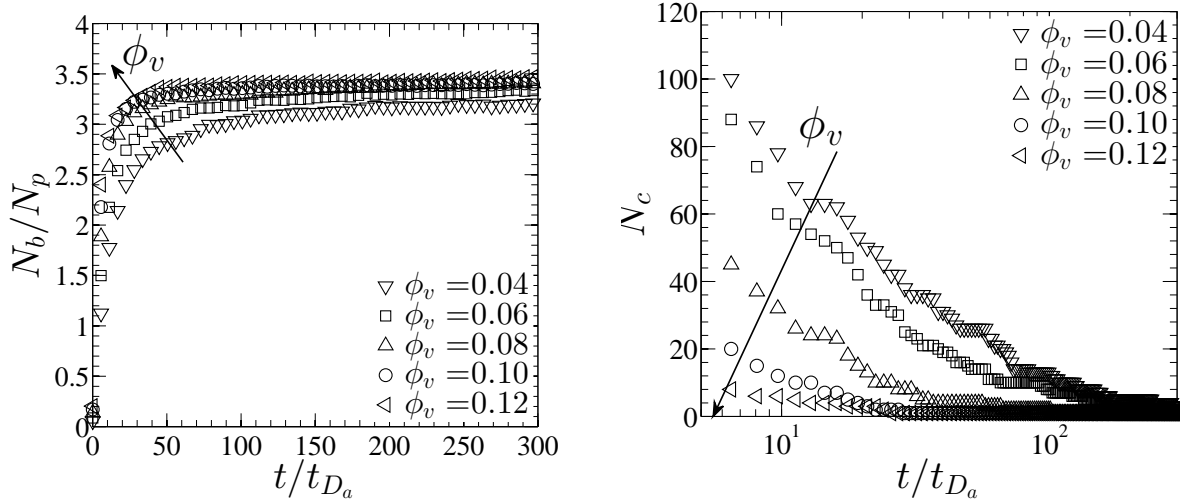
$$\frac{U(r)}{k_B T} = A \left[\left(\frac{2a}{r} \right)^{36} - \left(\frac{2a}{r} \right)^{18} \right] + B \frac{\exp[-\kappa(r - 2a)]}{r}. \quad (7.81)$$

Along with the other parameter values, the exact values of A , B , and κ used in our simulations are provided in [Table 7.2](#). These parameter values match exactly those used by [Cao et al. \(2012\)](#), including the very small time-step that must be taken due to the stiffness of the Lennard-Jones-like potential. To increase the volume fraction, ϕ_v , we increase linearly the number of particles, N_p while keeping the computational domain over which we solve the Stokes equations a fixed size such that $\phi_v = N_p 4\pi a^3 / (3L^3)$. This is different from [Cao et al. \(2012\)](#) where the number of particles was kept fixed as the volume fraction was varied.

As each simulation progresses, we monitor the number of bonds per particle, N_b/N_p . We use the criterion that a bond between two particles is formed when their center-to-center distance is less than or equal to $2.21a$ ([Cao et al. \(2012\)](#)). [Figure 7.6a](#) shows the

$A/k_B T$	$B/k_B T$	κ	$\Delta t/t_{D_a}$	η	a	ϕ_v	N_p	L
60	$20a$	$4/a$	10^{-4}	1	$3.29\Delta x$	0.04 – 0.12	558 – 1674	$128\Delta x$

Table 7.2: Simulation parameters for the colloidal gelation simulations



(a) Number of bonds per particle N_b/N_p as a function of t for different values of ϕ_v .

(b) Number of clusters in the domain N_c as a function of t for different values of ϕ_v .

Figure 7.6: Time evolution of the aggregation process for $\phi_v = 0.04 - 0.12$ and $\kappa = 4/a$.

time evolution of N_b/N_p for different values of ϕ_v . We observe for a fixed time, the number of bonds per particle increases as ϕ_v increases. We do see, however that as time increases, all simulations approach the same asymptotic value of $N_b/N_p \approx 3.47$. These observations consistent with the ASD results obtained by [Cao et al. \(2012\)](#).

The aggregation dynamics can also be quantified by the time evolution of the number, N_c , of particle clusters. We determine $N_c(t)$ by first compiling a list of bonded particle pairs at time t and then processing the list using the k -clique percolation algorithm implemented in Python by [Reid et al. \(2012\)](#). Figure 7.6b shows N_c as a function of time. We see that for each value of ϕ_v , the number of clusters decreases with time. We also find that for a fixed time, the number of clusters decreases as ϕ_v increases. The final structures we observe at $t/t_{D_a} = 300$ for different values of ϕ_v are shown in Table 7.3. For all values of ϕ_v except $\phi_v = 0.04$, we find that the particles aggregate to form a single structure that spans the entire domain. For $\phi_v = 0.04$, which is the most dilute case we considered, the final state consists of 2 clusters that are not long enough to connect the opposite sides of the domain. The tendency to form a single cluster was also noted by [Cao et al. \(2012\)](#) and [Furukawa and Tanaka \(2010\)](#). They also showed that for low volume fractions, hydrodynamic interactions between the particles are needed in order to capture the formation of a single percolated structure.

In addition to achieving very similar results as ASD, fluctuating FCM with the DC

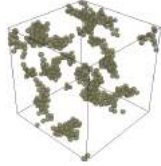
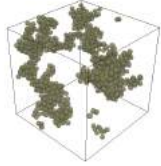
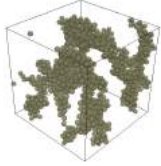
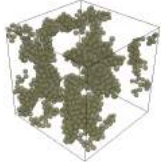
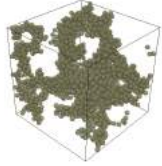
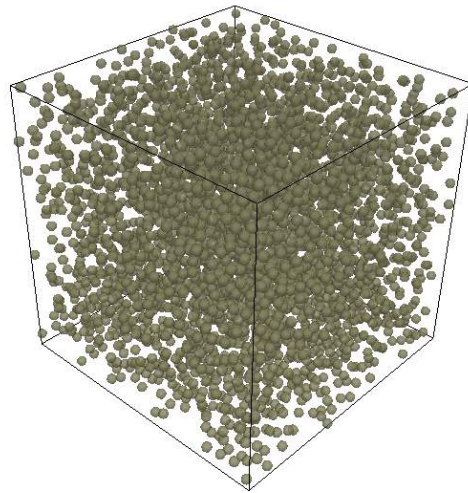
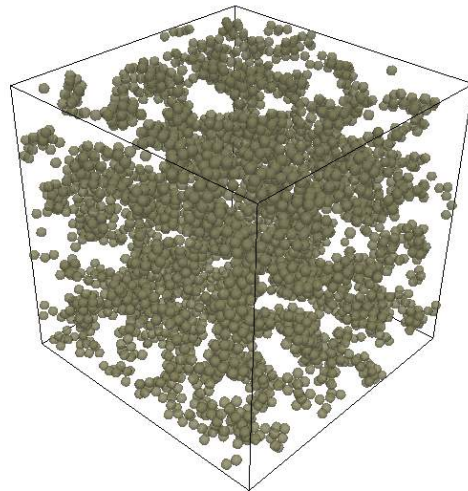
$\phi_v = 0.04$ ($N_p = 558$)	0.06 (837)	0.08 (1116)	0.10 (1395)	0.12 (1674)
NP	P	P	P	P
				
$N_c = 2$	1	1	1	1

Table 7.3: State of the suspension at $t/t_{D_a} = 300$ for different values of ϕ_v . The numbers in parentheses correspond to the number of particles in the domain N_p . The label “P” indicates that the particles aggregated to form a percolated network, while “NP” indicates that they have not. The snapshots show the suspensions at the final time and N_c is the number of clusters in the images (accounting for periodicity).

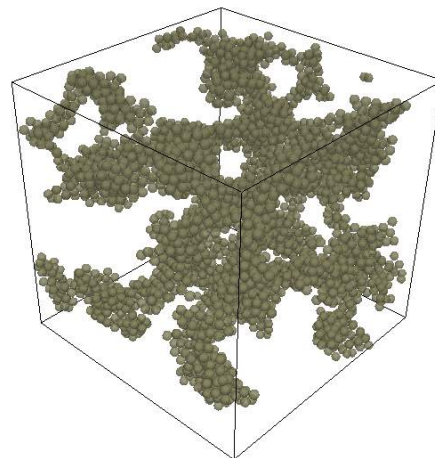
integration scheme provides these results at a relatively low computational cost. The average computational time needed for fluctuating FCM with the stresslets and the DC to reach $t/t_{D_a} = 100$ (10^6 timesteps) with $N_p = 1674$ was 2.5 days. The ASD simulations (Cao et al. (2012)) required approximately 10 days to reach $t/t_{D_a} = 100$ (10^6 timesteps) for half as many particles ($N_p = 874$). Our approach is 8 times faster when run on 64 Intel(r) Ivybridge 2.8 Ghz cores. To further test the scalability of fluctuating FCM with DC, we simulated a suspension of $N_p = 3766$ particles at a volume fraction of $\phi_v = 0.08$ using 64 Intel(r) Ivybridge 2.8 Ghz cores. Snapshots from the simulation at different time are provided in Figure 7.7. This simulation required 8 days to reach $t/t_{D_a} = 145$ (1.45×10^6 time steps). For this larger system size, we again find that the particles do eventually aggregate to form a single structure that percolates the entire domain.



(a) $t/t_{D_a} = 0$.



(b) $t/t_{D_a} = 8$.



(c) $t/t_{D_a} = 145$.

Figure 7.7: Snapshots of the aggregation process for $\phi_v = 0.08$ and $N_p = 3766$.

7.6 Conclusions

In this study, we presented a mid-point time integration scheme we refer to as the drifter-corrector (DC) to efficiently integrate the overdamped equations of motion for hydrodynamically interacting particles when their Brownian motion is computed using fluctuating hydrodynamics. Methods based on fluctuating hydrodynamics such as the stochastic and fluctuating IBMs and the fluctuating FCM have been shown to drastically reduce the cost of including Brownian motion in simulation by simultaneously computing the deterministic and random particle velocities at each timestep. Like Fixman’s method and RFD-based schemes, our DC scheme allows for the effects of the Brownian drift term to be included without ever having to compute it directly. The DC, however, was designed especially for the case where imposed constraints on the rate-of-strain are used to provide a more accurate approximation to the particle hydrodynamic interactions, as is the case with fluctuating FCM. Imposing these constraints incurs an additional cost for existing schemes. Using these schemes with fluctuating FCM, we showed that this constraint would at the very least double the cost per timestep, which in practice meant an additional 10 Stokes solves per timestep. We show that by using the DC with fluctuating FCM, this additional cost can be reduced to a single Stokes solve per time step. Though we have developed the DC for and tested the scheme with fluctuating FCM, FCM’s similarity with other methods, such as the stochastic and fluctuating IBMs, suggests that the DC could be an effective scheme to integrate particle positions for these methods as well. Using the DC with fluctuating FCM, we have provided an extensive validation of the scheme, showing that it reproduces the correct equilibrium particle distribution, as well as provides the distribution dynamics in accordance with the Smoluchowski equation. We have also demonstrated the effectiveness of fluctuating FCM with the DC for colloidal suspension simulations, examining the collapse of a small cluster of particles, as well as the gelation process of a suspension. In doing so, we were able to both quantify the effect of including higher-order corrections to the hydrodynamic interactions, as well as demonstrate the ability to accurately simulate colloidal suspensions at large-scale. Indeed, in Chapter 11 we apply this approach with active particle models (Delmotte et al. (2015) and Chapter 10) to understand recent experimental results (Leptos et al. (2009); Kurtuldu et al. (2011)) on the dynamics of passive Brownian tracers in active particle suspensions.

The methods described in this work may also be modified and extended to simulate particles with more complicated shapes (Cichocki et al. (2015)). While one approach is to construct rigid (Vázquez-Quesada et al. (2014); Delong et al. (2015)), or flexible (Majmudar et al. (2012)) particles from assemblies of spherical particles, another approach is to modify the shape of the kernel in the projection and volume averaging operators to reflect the shape of the particle itself. This has been done with FCM for ellipsoidal particles (Liu et al. (2009)) and, as the underlying framework of the method remains unchanged, fluctuating FCM with the redefined operators should yield particle velocities that satisfy the fluctuation-dissipation theorem. A current challenge is to adapt the DC to these particle shapes as the Brownian drift term will also depend on the orientation of the particle. It would be of interest to compare fluctuating FCM results with the

experimental measurements of [Han et al. \(2006\)](#) and the recent simulations of [De Corato et al. \(2015\)](#). We are currently pursuing this line of research to provide a similar set of efficient and accurate simulation techniques to understand the dynamics of suspensions of ellipsoidal Brownian particles.

Chapter 8

Conclusions: combining fluctuating FCM with active FCM.

The tool developed in Chapter 6 effectively combines our extension of the force-coupling method for active particles to a highly scalable fluid solver and an efficient parallelization of pairwise short-range interactions. Our code scales linearly with the particle number, even for high volume fractions.

We showed in the validations (Section 6.3) that our method provides an accurate description of hydrodynamic interactions which compares very well with the more costly boundary element method.

The time-integration scheme developed in Chapter 7, called Drifter-Corrector, accounts for the drift terms arising in the overdamped limit of Langevin equations for particle motion with only one additional Stokes solve per time-step compared to deterministic simulations. The validations with analytical and numerical results from the literature prove the robustness of our approach. The efficiency of the method allowed the simulation of colloidal gelation and aggregation processes at large scales.

Both tools are implemented in the same code so that combining the active part with the fluctuating FCM does not require much efforts. Swimmers' orientations are integrated with the Euler-Maruyama scheme starting at the midstep of the Drifter-Corrector. They are then projected onto the unit sphere at every time step. Appendix E provides more details and shows how this time integration recovers the correct Langevin equations for the rotational motion of spherical particles.

In the literature, objects' orientations are sometimes represented with unit quaternions. The interest of working with unit quaternions instead of unit vectors to track orientation is twofold:

1. time-integration schemes for quaternions are based on rotation operations, whereas schemes for vectors are based on Taylor expansions. Rotations inherently maintain the norm of the quaternion while additions arising in Taylor expansions result in the accumulation of numerical errors (Zhao and van Wachem (2013)).

2. when considering non axisymmetric bodies, two orthogonal unit vectors attached to each body must be tracked¹. Using a unit quaternion with four components instead is less costly.

These points are extensively discussed in Appendix [F](#).

¹Their cross product correspond to the third unit vector constituting the body frame.

Lire
la seconde partie
de la thèse